INFORMATION TO USERS

This manuscript has been reproduced from the microfilm master. UMI films the text directly from the original or copy submitted. Thus, some thesis and dissertation copies are in typewriter face, while others may be from any type of computer printer.

The quality of this reproduction is dependent upon the quality of the copy submitted. Broken or indistinct print, colored or poor quality illustrations and photographs, print bleedthrough, substandard margins, and improper alignment can adversely affect reproduction.

In the unlikely event that the author did not send UMI a complete manuscript and there are missing pages, these will be noted. Also, if unauthorized copyright material had to be removed, a note will indicate the deletion.

Oversize materials (e.g., maps, drawings, charts) are reproduced by sectioning the original, beginning at the upper left-hand corner and continuing from left to right in equal sections with small overlaps.

ProQuest Information and Learning
300 North Zeeb Road, Ann Arbor, MI 48106-1346 USA
800-521-0600

SUBSTRATE BIAS ASSISTED
RF THERMAL PLASMA DIAMOND DEPOSITION

Jörg Oberste Berghaus

Plasma Technology Research Center (CRTP)
Department of Chemical Engineering
McGill University

Dr. Jean-Luc Meunier, Supervisor
Dr. François Gitzhofer, Co-Supervisor

A Thesis Submitted to the Faculty of Graduate Studies
and Research in Partial Fulfillment of the Requirements
for the Degree of Doctor of Philosophy

McGill University
Montreal, Canada

à Stéphanie

Abstract

Polycrystalline diamond films are produced by chemical vapor deposition (CVD) in a r.f.-induction thermal plasma system. A dc bias voltage between –400 V and +500 V is applied to the deposition substrate. This is made possible by maintaining the reactor environment at ground potential and introducing a high-impedance, high-power filter network, eliminating the r.f. voltage drop across the plasma-probe junction. The Ar, H_2, CH_4 plasma (8.45 % H_2, 0.21 % CH_4) impinges on a molybdenum substrate probe (5 mm in diameter) in stagnation point flow. The resulting diamond films are analyzed by Scanning Electron Microscopy (SEM) and Raman Spectroscopy. The initial nucleation density is enhanced at negative bias voltage. However, this comes at the expense of degradation in crystalline quality. Positive voltage improves the quality and augments the film growth rate. A threefold increase in linear growth rate is attained at +500 V as compared to the unbiased case. The growing diamond film is used as an electrical and thermal probe. Electron emission currents from the developing diamond structures are exploited to monitor the film evolution during deposition. Diamond nucleation and growth stages are identified, and the bias voltage is varied in-situ to adjust to the changing growth requirements. A numerical simulation and optical emission spectroscopic measurements are used to characterize the plasma free stream as well as the boundary layer region between the plasma and the substrate. Current-voltage characteristics of the substrate are interpreted, and electrical probe theory is applied. It is shown that at negative bias the plasma–substrate interface is described by an expanding collision-dominated sheath imbedded inside the chemically reacting thermal boundary layer. Contrary to dc arcjet CVD, there is no secondary discharge created in the r.f. system at positive bias voltage. Also, the role of ion bombardment at negative bias is shown to be of little importance. It is inferred that the predominant mechanism leading here to changes in diamond formation under bias conditions is the promotion and suppression of electron emission from the growing diamond structures.

Résumé

Les revêtements de diamant polycristallin sont produits dans un plasma thermique inductif par déposition chimique en phase gazeuse (CVD). Une tension continue entre –400V et +500V est appliquée afin de polariser le substrat. Ceci est rendu possible en maintenant l'enceinte du réacteur à la masse et par l'installation d'un filtre à haute-puissance/haute-impédance qui élimine la chute de tension haute fréquence entre le plasma et la sonde. La surface de la sonde/substrat de molybdène (5 mm diam.) est orientée normale à l'axe d'écoulement du plasma $Ar/H_2/CH_4$ (8.45 % H_2, 0.21 % CH_4). Les couches de diamant ainsi obtenues sont analysées par microscopie électronique (SEM) et par spectroscopie Raman. La densité de nucléation initiale est augmentée par une polarisation négative au détriment cependant de la qualité cristalline qui décroît à ces conditions. Une polarisation positive par contre améliore la qualité des cristaux de diamant et augmente les taux de croissance de la couche. La vitesse de croissance du dépôt est augmentée d'un facteur trois (3) à +500V en comparaison avec le cas non polarisé. Pendant la croissance, la couche de diamant est utilisée comme une sonde pour les mesures électriques et thermiques. L'émission électronique du film de diamant permet de suivre en temps réel l'évolution de la couche. Les stages de nucléation initiale et de croissance sont identifiés, et la polarisation est adaptée in-situ afin de satisfaire aux besoins changeants de la déposition. Le jet du plasma et la couche limite au-dessus du substrat sont caractérisés par les prédictions d'une simulation numérique et par des mesures de spectroscopie d'émission. Les caractéristiques électriques courant-tension, collectées par le substrat, sont interprétées et les théories de sonde électrostatiques sont appliquées. Il est établi qu'à une polarisation négative la zone de charge d'espace au-dessus de la surface est en expansion et est dominée par des collisions. Cette zone de charge d'espace est comprise à l'intérieur de la couche limite thermique. Contrairement aux dépositions dans les jets plasma d.c., aucune décharge secondaire n'est créée dans le système h.f. inductif à une polarisation positive. De plus, il est montré que le bombardement ionique a un effet négligeable même à forte polarisation négative. Le mécanisme principal, responsable des changements observés au niveau de la croissance du diamant sous des conditions de polarisation variées, est attribué aux variations de l'émission électronique induite à la surface de diamant.

Acknowledgements

For their contribution to this research project I would like to thank the following individuals and groups:

Foremost, my supervisor Professor Jean-Luc Meunier for his guidance, patience and support without which the completion of this work would not have been possible.

Professor François Gitzhofer for his continued interest and helpful suggestions.

Leo Nikkinen for his invaluable help in high-frequency problems and for many enlightening discussions.

Professor Richard J. Munz for his trust in giving me unique opportunities.

Charles Dolan, Lu Cusmich, Alain Gagnon, Walter Greenland, Frank Caporuscio, Helen Campbell and the Chemical Engineering Staff for their technical support.

Past and present CRTP research group members: Dr. Tony Adonna, Dr. Sylvain Coulombe, Dr. Antonio-Carlos da Cruz, Dr. Patrice Nadeau, Mrs. Karen Sum, Dr. Julie Filion, Mr. Hong Son Seon, Mr. David Harbec.

The summer students Daniel Feigenbaum Cleiman and Jaime Yip.

Dr. Samir Ilias (Université de Montréal, Dept. de Phys.) and Dr. Stefanie Warner (Dept. of Chem., McGill) for their assistance in the Raman analysis.

Le Fond pour les Chercheurs et l'Aide à la Recherche du Ministère de L'Éducation du Québec (FCAR) and the Department of Chemical Engineering, McGill University for funding this project.

My father, my mother and Ellen for their unconditional endorsement.

Dr. Stéphanie Gélinas for her unparalleled inspiration and support throughout my work.

Table of Contents

EXPERIMENTAL

CHAPTER 3

RESULTS

CHAPTER 4

CHAPTER 5

CHAPTER 6

CHAPTER 7

CHAPTER 8

DISCUSSION

CHAPTER 9

CONCLUSION

CHAPTER 10

REFERENCES

List of Figures

INTRODUCTION

1. General Introduction

Over the past years there has been an increasing number of research efforts directed towards producing diamond films under thermodynamically metastable conditions. The interest in diamond is due to its excellent physical and chemical properties. Diamond is the hardest known material and combines optical transparency from ultraviolet to infrared, low friction coefficient and very good thermal conducting and electrical insulating properties. It is also chemically inert. For all these reasons the technical challenge of diamond synthesis in the form of films is very attractive in view of potential industrial applications.

Crystalline diamond can be grown by an astonishing wide variety of plasma assisted chemical vapor deposition processes (CVD). The activation methods range from low-pressure hot-filament, microwave, and capacitively and inductively coupled radio-frequency discharges to highly energetic atmospheric pressure combustion flames and direct-current and r.f. thermal plasma jets. To produce diamond coatings on industrially relevant substrates there are, however, still several intriguing problems related to growth rate, diamond quality, film uniformity and initial diamond nucleation.

Thermal plasma CVD, using either d.c. arcjets or r.f.-induction flames, has received increasing attention due to the high diamond growth rate achievable. Film growth rate in the order of 30 μm/hr to several hundred μm/hr have been reported and can be attributed to the high density of growth precursors available at the elevated pressure (Matsumoto et al. 1992, Lu et al. 1992). Among these technologies, r.f. inductively coupled plasmas can be generated over larger and more uniform gas volumes. This homogeneity of the induction plasma flame is reflected in the formed deposit, making it more prone for creating uniform films. The r.f. thermal plasma technology hence shows some advantage in view of attaining large and uniform surface coverage at high film growth rates.

The diamond formation in thermal plasma CVD depends critically on the non-equilibrium gas phase chemistry in the boundary layer region between the plasma and the substrate surface, in which active growth species are both rapidly created and destroyed.

Manipulation of process parameters directly affecting the boundary layer chemistry allows for enhancement both in deposition rate and in diamond film quality (Girshick et al. 1993, Baldwin et al. 1994, Oberste Berghaus et al. 1997). However, these parameters such as composition, jet momentum, gas temperature etc. are strongly coupled, and it is difficult to change one operational condition without simultaneously shifting all the others. An independent process parameter that can be adjusted to control the diamond growth during deposition is often desired. Substrate biasing could, in principle, provide such a control.

Using d.c. arcjet technology, it has been found that the non-equilibrium in the boundary layer and consequently the diamond growth characteristics can be enhanced by applying an electrical voltage between the substrate and the plasma. Positive substrate bias voltages in d.c. arc deposition result in an astounding increase in film growth rates and diamond quality (Matsumoto et al. 1990/1992, Ito et al. 1995, Baldwin et al. 1995).

The technique of substrate biasing is widely used in low-pressure diamond CVD, in particular in microwave (MPECVD) and hot-filament plasma systems (HFCVD). To realize the full potential of CVD diamond coatings on foreign substrates, great progress has been made in obtaining high-density oriented diamond nucleation by applying a negative d.c. voltage during the initial diamond nucleation stage (Yugo et al. 1991/1995, Ma et al. 1995, Stoner et al. 1993, Jiang et al. 1994). An extended negative voltage often leads to degradation in film quality (Lee et al. 1990). By acknowledging the inherent difference between the initial nucleation and the subsequent film growth, the bias voltage can be varied in-situ to adjust to the changing growth requirements. For this purpose, monitoring and identifying the different stages of the diamond film formation are vital (Kulish et al. 1996, Beckmann et al. 1994, Milne et al. 1995).

To our knowledge, less work has been done on substrate biasing in induction thermal plasma diamond CVD. This may be due to the technical difficulties arising from the strong radio-frequency signal, as well as the lack of a reference electrode, inherent to these systems. However, combining this promising technology of substrate biasing with the advantages of the rf-induction thermal plasma system is the consequent next

technological advancement in diamond CVD and constitutes the main topic in the present research work.

1.1 Overall Objectives

The primary objectives of this thesis are to demonstrate the implementation of d.c. substrate biasing in an r.f. thermal plasma diamond deposition system and to investigate the effect of the bias voltage on the diamond nucleation and growth behaviour. The goal is to show the application of the substrate bias voltage as an additional and independent process operating parameter.

The secondary objective is to monitor the diamond evolution by using the growing film as an electrical and thermal probe. In conjunction with appropriate theory, these probe measurements are to yield information about plasma-substrate interactions under bias conditions. The underlying motivation is to infer the predominant physical mechanisms in bias assisted diamond formation in the r.f.-induction thermal plasma CVD process.

1.2 Organization of the Thesis

In order to achieve these objectives, the thesis is organized in ten chapters.

After this Introduction (*CHAPTER 1*), the Background section (*CHAPTER 2*) introduces the process and the pertinent operating parameters by reviewing the relevant literature.

The Experimental section in *CHAPTER 3* describes the apparatus, procedures and measurement methods. Emphasis is posed on the design aspects, which allow the implementation of d.c. substrate biasing in the r.f. plasma environment. *CHAPTER 3* includes a description of the optical emission spectroscopic diagnostics that are used in *CHAPTER 4* and *5*.

The Results are presented in *CHAPTER 4* through *CHAPTER 8*. In *CHAPTER 4*, the plasma free stream is characterized by using the spectroscopic measurements. Combining these measurements with a thermodynamic analysis yields information about the equilibrium state of the discharge.

In *CHAPTER 5*, the dimensions of the thermal boundary layer are estimated by formulating a numerical simulation of the flow and temperature fields. The results are compared to spectroscopic measurements taken in the boundary layer above the substrate surface.

The effect of substrate bias voltage on diamond nucleation and growth is experimentally investigated in *CHAPTER 6*. The bias voltage is then used as an independently adjustable process parameter at otherwise invariant plasma operating conditions.

The in-situ measurements obtained by using the growing diamond film as an electrical and thermal probe are presented and explained in *CHAPTER 7*.

The effect of surface temperature on the diamond growth behaviour is examined in *CHAPTER 8*.

The Discussion (*CHAPTER 9*) addresses the applicability of electrical probe theory to the present situation, and a basic theoretical description of our process is developed. The experimental findings are compared with ongoing research efforts in various CVD systems and the governing mechanisms in bias assisted diamond CVD in our r.f. plasma system are inferred.

The final chapter (*CHAPTER 10*) summarizes the conclusions of this work and the original contributions to knowledge.

BACKGROUND

2. Background

2.1 Chemical Vapor Deposited Diamond

The first successful efforts to grow diamond from the vapor phase in the 1950's by Deyagin in the former Soviet Union and later confirmation in 1958 by W.G. Eversole in the United States demonstrated that diamond could be grown by chemical vapor deposition from hydrocarbon gases under metastable conditions. Worldwide interest in CVD diamond was stimulated by publications associated with the National Institute of Inorganic Materials (NIRIM) Japan in the late 1970's.

Similar to natural diamond, synthetic diamond is formed from tetrahedral bonded sp^3-hybridized carbon atoms. The crystal structure can be portrayed through the (100) plane, the (110) plane or the (111) plane. The morphology of CVD diamond crystallites is dominated by cubic (100) and octahedral (111) surfaces and occasionally (111) twin planes. Cubo-octahedra exhibiting both (100) and (111) surfaces are also very common. The resulting crystal shapes can intergrow as polycrystalline layers with morphologies ranging from well-defined facets to poorly defined rounded shapes or highly irregular forms.

The interest in diamond is due to its excellent physical and chemical properties. Diamond is the hardest known material and combines optical transparency from ultraviolet to infrared, high electron and hole mobility, low friction coefficients and very good thermal conducting and electrical insulating properties. It is also chemically inert. Some properties are listed in Table 2.1.1.

Table 2.1.1: Typical Properties of Diamond
(Data from NRC Report (1990), Spear et al. (1989), Ravi (1994))

Property	*Typical Value*
Indentation Hardness	10000 kg / mm^2
Friction Coefficient in Air	< 0.1
Dielectric Constant at 300 K	5.7
Electric Breakdown Strength	$2 \cdot 10^7$ V/cm
Thermal Conductivity at 293 K	Type Ia 6-10 W/cm K Type II a 20-21 W/cm K
Linear Thermal Expansion Coefficient at 293 K	$0.8 \cdot 10^{-6}$ K^{-1}
Compressibility	$1.7 \cdot 10^{-7}$ cm^2/kg

(Type Ia: 2000 ppm nitrogen, most natural diamond; Type IIa: <5 ppm nitrogen, high quality natural and synthetic diamond)

Application of diamond films as abrasive or as cutting tools arises from its extreme hardness and high thermal conductivity. Diamond films may find application as wear-resistant coatings on wire-drawing dies or as coatings for drills and bearing surfaces. Those films may also serve as impact-protection coatings for erosion and small-particle impact. The high thermal conductivity, low expansion coefficient and strength of diamond provide high thermal shock resistance. This combination of properties can be advantageous in windows for high power lasers. The favorable optical properties of diamond encourage its use in optical elements and diamond coated optics. The high thermal conductivity has led to the use of diamond as a heat sink in electronic applications, i.e. microchip packaging. Diamond can also be used as a wide band-gap semiconductor, having a high breakdown voltage and very high saturation velocity. These applications and many others will likely be expanded by the availability of uniform, continuous and highly crystalline diamond films.

2.1.1 Chemistry of CVD Diamond Growth

In the late 1970's the addition of atomic hydrogen to the reactants in diamond CVD increased the growth rate by orders of magnitude, eliminated the need for diamond substrates and made the process technologically significant. Atomic hydrogen serves a number of critical roles in the CVD process.

Diamond can grow when only sp^3-hybridized single bonds of the carbon are allowed to form. Atomic hydrogen provides carbon-hydrogen bonds on the cleaved diamond surface, where otherwise energetically unfavorable dangling single bonds would recombine to sp^2 double bonds. Diamond growth occurs when the surface hydrogen are replaced by carbon from the vapor phase. The gas-phase hydrogen combines with the surface hydrogen to from hydrogen gas, leaving a vacant site. Because in most CVD processes the ratio of hydrogen to carbon is very large, the vacant site is likely replaced by another hydrogen from the vapor phase. However, every now and then, a carbon or hydrocarbon radical will collide with the vacant site and attach to the diamond crystal, thereby generating diamond growth (Anthony 1990). This proposed mechanism is schematically illustrated in Figure 2.1.1.

Atomic hydrogen is also important in the etching of both diamond and graphite. Since the removal of graphite is orders of magnitude higher than for diamond, the presence of atomic hydrogen enhances the net diamond formation in the films (Spear et al. 1989).

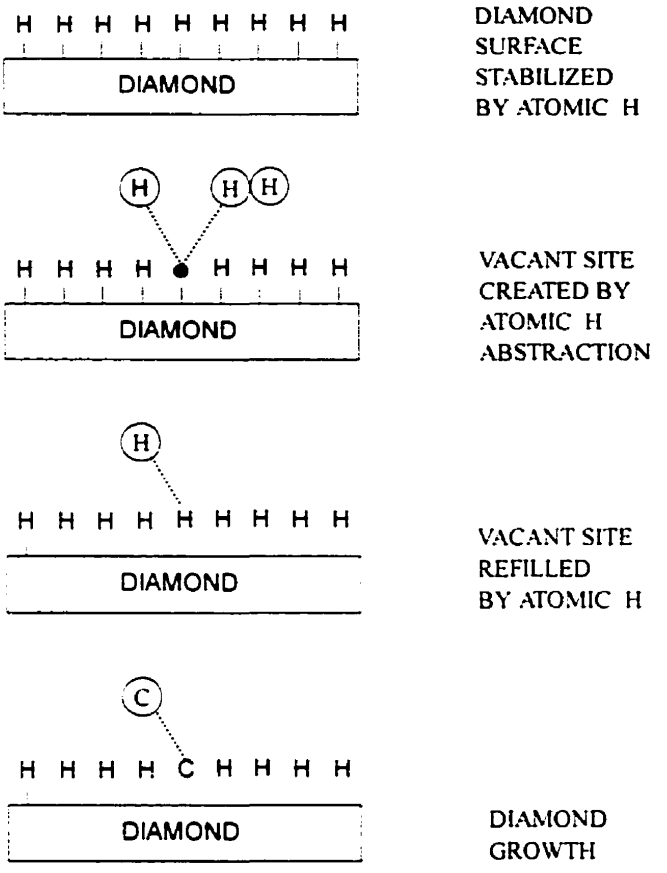

Figure 2.1.1 : Suggested Diamond Growth Mechanism.
(Modified from Anthony 1990)

Crystalline diamond can be grown by an astonishing wide variety of energetically assisted chemical vapor deposition processes. The traditional distinction between non-thermal activation and atmospheric pressure thermal plasma methods can be made. The non-thermal processes include microwave plasma enhanced CVD (MPECVD) (e.g. Sattel et al. 1996, Kulish et al. 1996, Stoner et al. 1993), hot-filament CVD (HFCVD) (e.g. Chen et al. 1995/1996, Chao et al. 1994, Lee et al. 1990), and low-pressure capacitively or inductively coupled radio-frequency systems (e.g. Bárdos et al. 1994, and Teii 1999). In the atmospheric pressure range, combustion flames (Matsui et al. 1990), direct-current arc jets (e.g. Owano et al. 1991, Lu et al. 1991/1992, Matsumoto et al. 1991/1992) and rf induction thermal plasma jets (e.g. Baldwin et al. 1994, Girshick et al. 1993, Oberste

Berghaus 1996, Matsumoto et al. 1987) are used. The diamond film quality achieved in non-thermal deposition systems is generally superior. In conjunction with substrate biasing, very high initial nucleation rates and even textured film deposition and epitaxial crystal orientation with respect to the substrate can be attained (e.g. Wolter et al. 1993, Lee et al. 1995, Schreck et al. 1996). However, this comes at the cost of a low film growth rate. For example, the typical deposition rates in MPECVD are in the range of 0.1 to 5 μm/hr. On the other hand, the high-pressure techniques are much more conducive for potential scale up, and show significantly higher growth rates. Deposition rates far exceeding 100 μm/hr can be realized.

2.2 CVD Diamond Synthesis from Thermal Plasma

Synthesis of polycrystalline diamond films by Chemical Vapor Deposition in thermal plasma jets has amply been demonstrated. Significant contributions in this research area have been made by the National Institute for Research in Inorganic Materials (NIRIM) in Japan, the Department of Mechanical Engineering at the University of Minnesota by providing comprehensive parametric results, and by the High Temperature Gas-Dynamic Laboratories at Stanford University by investigating the gas and surface chemistry in the boundary layer, to name some of the most important research groups.

The thermal plasma is conventionally generated by either dc-arcs or by rf-inductively coupled discharges. Dc-plasmas are inherently easy to operate and can generate very high linear growth rates. But the steep radial temperature and velocity gradients in the torch can cause non-uniform and irregular deposits (Matsumoto et al. 1992). In fact, radial non-uniformity of the diamond deposit is a common problem on large substrates, which are conventionally oriented normal to the oncoming plasma flow. A likely explanation lies in the radial gradients of temperature and concentration in the plasma flame itself, which are reflected in the formed deposit (Cappelli et al. 1990, Zuang et al. 1992, Hernberg et al. 1991). To overcome this limitation, Lu et al. (1991) introduced a triple dc-torch arrangement, whereby three plasma jets coalesce to form a large converging plasma volume. In an attempt to enlarge the dc-plasma flame tail to obtain wider deposition and uniform film thickness, Matsumoto et al. (1990) applied a positive bias voltage to the substrate, and thereby partially transferring the arc to the surface. An increase in diamond growth rate was observed, but the desired improvement in uniformity could not be induced.

Rf induction thermal plasmas, on the other hand, excite a large volume of reactant gases from the onset (Lu et al. 1992, Baldwin et al. 1994). The relatively large and uniform flame core, which exits the torch at a lower velocity, makes these plasmas more prone to create uniform deposits. Previous work, in which a small probe-like substrate tests the growth conditions in different radial locations in the rf plasma, revealed that uniform growth over large substrates is only likely within the central homogeneous core

of the flame (Oberste Berghaus et al. 1997). This uniform core, where temperature and concentration gradients are minimal, is characteristic to rf thermal plasmas. Possible film contamination that arises out of electrode erosion in dc torches can also be eliminated. The rf thermal plasma technology hence shows some advantages in view of attaining large surface coverage of diamond coatings at high growth rates.

2.3 Relevant Deposition Parameters

Although the methods of plasma generation for CVD diamond formation are intrinsically different, the critical deposition parameters are generally similar for dc-plasma and rf-induction plasma deposition.

2.3.1 Substrate Temperature

The surface temperature is one of the most significant process parameters in CVD diamond deposition. For diamond films with high levels of crystal perfection grown in thermal plasmas, the temperature is usually in the range of 900°C to 1200°C. Studies on the effect of substrate temperature have been conducted by Hernberg et al. (1991), Owano et al. (1991) and Lu et al. (1992). Lu used a modified dc torch system and observed that at low temperatures (T_s < 1000°C) triangular shaped (111) faces dominate the crystallite morphology, while at higher temperatures (T_s > 1200°C) square shaped (100) faces are predominant. Girshick et al. (1993) confirmed this trend in an rf system. Baldwin et al. (1994) obtained the highest diamond growth rate in a induction plasma at a surface temperature of 1100°C.

With an rf deposition system similar to the one used in this study an optimal surface temperature range between 910°C and 1010°C was previously established and diamond deposits with large crystal faces were obtained (Oberste Berghaus 1996). Square shaped faces were predominant. Reduction in temperature to approximately 850°C resulted in the growth of microcrystals only, creating ball shaped cauliflower structures. At a high temperature of about 1100°C only randomly distributed islands of small diamond nuclei were formed. Further increase in surface temperature promoted

increasing graphite formation. The discrepancy in the optimal temperature ranges can be attributed to differences in plasma composition and/or heat flux (Oberste Berghaus et al. 1997).

Maintaining a constant temperature across the entire substrate area can be very difficult in particular in the conventional stagnation point flow geometry using a flat substrate positioned normal to the plasma flow. The extend to which radial surface temperature variations contribute to the formation of nonuniform deposits was investigated by Zhuang et al. (1992), who showed that a uniform surface temperature is an essential but not sufficient condition for uniform diamond coverage.

Because the impinging thermal plasma jet heats the substrate, temperature control is generally achieved by altering the thermal conduction or thermal contact resistance between the substrate and a water-cooled base (Oberste Berghaus et al. 1997, Lu et al. 1992, Bieberich and Girshick 1996). The measurement of the surface temperature in the highly luminous plasma environment during deposition is, however, not a trivial task (Bieberich and Girshick 1996).

2.3.2 Process Pressure

Typical reported diamond film growth rate are ~ 1 μm/hr for low-pressure processes (P < 10 Torr (0.013 atm.) and ~100 μm/hr for high pressure (P ~ 1 atm) techniques. Since the diamond formation depends on the supersaturation of hydrocarbon species above the substrate, Yu et al. (1989) and Owano et al. (1991) attribute this difference to the greater density of growth species available at elevated pressures. Hernberg et al. (1991) studied the pressure dependence of the film growth rate by varying the process pressure between 0.2 atm and 0.6 atm in an rf-induction plasma system. Pressure reduction increased the growth rate and changed the morphology from a collection of non-uniformly distributed crystallites to a very homogeneous film with practically no granular structure at all. Kohzaki et al. (1993) deposited very uniform diamond films over a substrate 100 mm in diameter by reducing the process pressure in an rf-induction system to 150 Torr (0.2 atm). Lu et al. (1992) also investigated the effect of pressure on the diamond deposition

in a thermal plasma reactor. The highest deposition rate was obtained at 270 Torr (0.355 atm). This peak is attributed to the thermodynamic balance between generation and recombination of atomic hydrogen and carbon-containing active species above the substrate. This pressure of 270 Torr has successfully been adopted in previous work in the rf deposition system (Oberste Berghaus et al. 1997) and is used in the present study.

2.3.3 Process Gases

A large number of hydrocarbon gases have been used to deposit diamond. Methane has been the gas of choice. The methane to hydrogen feed ratio has a pronounced effect on the crystallite morphology. Girshick et al. (1993) found for an rf-induction system that cases with 1% CH_4 in H_2 produced well-faceted crystallites, whereas a 5% ratio yields round "cauliflower"-type structures. Owano et al. (1991) confirmed the observation and created higher quality diamond at lower methane to hydrogen ratios. Similar results for rf systems are reported by Park et al. (1995). Lu et al. (1992) state that an increase in methane concentration results in smaller grain size due to the increased number of secondary nucleation on the existing diamond crystal facets. When the methane concentration exceeds a certain value, a large portion of the film starts to loose its crystallinity dramatically and changes to cauliflower balls. Using dc plasmas high-quality films can be produced at a methane concentration of 5%. Lu et al. (1992) explain the difference in the ideal methane concentration between rf and dc systems in terms of the different capabilities in converting the incoming methane into active species. It is, however, more likely that the higher heat flux to the substrate, which can be generated by dc torches, is responsible for the shift in optimal methane concentration, since both rf and dc plasmas are usually sufficiently hot to completely dissociate the process gases. The effect of methane concentration is found to be coupled with heat flux and substrate temperature conditions (Owano et al. 1991). Baldwin et al. (1994) optimized an rf-induction plasma deposition system in terms of the operating conditions, and report the highest diamond growth rates obtained at a gas feed ration of 2.5% CH_4 in H_2. In previous work an $Ar/H_2/CH_4$ gas mixture of 8.65% H_2 and 0.25% CH_4 was successfully

used to deposit high quality diamond films at a high growth rate (Oberste Berghaus et al. 1997).

In low-pressure CVD systems (MPECVD and HFCVD) the effect of an increased nucleation at a higher methane concentration has repeatedly been used in combination with other pre-treatment methods to enhance the initial diamond nucleation density on non-diamond substrates (Yugo et al. 1995, Sattel et al. 1996, Stoner et al. 1993).

2.4 Substrate Material and Pretreatment

Most of the experimental work on diamond deposition presently available is for silicon and molybdenum substrates. Research efforts aimed at expanding the range of materials and improving diamond/substrate interface properties are dominated by studies in low-pressure CVD. It has proven difficult to directly coat substrates like steels, nickel alloys, cemented carbides and most alloys containing transition metals with well-adhering, high quality diamond films (Deueler et al. 1996). High residual stresses developed in the diamond due to the mismatch in the thermal expansion coefficients of the film and its substrate are considered to be the principal cause for poor film adherence (Weiser et al. 1995, Lu et al. 1992). Another reason is the dissolution and diffusion of carbon into the substrate material, which in the case of stainless-steel, W, WC-Co, Fe and Ni based alloys promotes the formation of a graphitic soot at the diamond substrate interface. This layer is often made responsible for easy film delaminating (Deueler et al. 1996, Karner et al. 1996, Weiser et al. 1995, Monteiro et al. 1996). An additional factor is the diamond nucleation density. Low nucleation densities promote large grain sizes and, correspondingly, small contact area between the film and the substrate, resulting in poor adhesion (Zhu et al. 1995).

To circumvent these problems a thin interface layer is sometimes prepared, which can form strong chemical bonds with both the diamond and the substrate material, and which has an intermediate thermal expansion coefficient (Zhu et al. 1995, Bahr et al. 1996). Buffer layers of TiN (Weiser et al. 1995) and AlN (Godbole et al. 1995), which also serve as effective carbon diffusion barriers, have been used for this purpose.

An additional way to improve adhesion is to implement a pre-treatment that is aimed at enhancing nucleation density (Deueler et al. 1996). High nucleation densities also lead to an early coalescence of the diamond particles to produce a continuous and smooth coating at an early stage of the growth (Chao et al. 1994). The most common method for promoting nucleation is to scratch or seed the substrate with diamond powder. The increase in nucleation is attributable to either carbonaceous residues left from the polishing, supplying the nucleation sites, or to the damaging of the surface resulting in high-energy sites on which nucleation is most likely initiated. An alternate method to increase the nucleation density is to apply a negative substrate bias voltage at a high methane concentration prior to normal deposition (e.g. Sattel et al. 1996, Yugo et al. 1991). The advantage of bias enhanced nucleation (BEN) is that it does not damage the surface of the substrate, such as the conventional scratching methods. Another important characteristic of the biased nucleation is the strong texture and to some extend crystal orientation of the nuclei (Chao et al. 1994). In exceptional cases, bias pre-treatment is reported to result in (100) diamond planes almost perfectly aligned with the substrate Si(100) or β-SiC(100) (Stöckel et al. 1996). Bias enhanced nucleation has extensively been used in low-pressure CVD systems. But also in dc thermal plasmas an increase in nucleation density under negative substrate bias has been implied in the literature (Matsumoto et al. 1990). The exact mechanism leading to the enhanced nucleation density is, however, still not well understood and is subject to debate. Several workers (Sattel et al. 1996, Reinke et al. 1996) infer that ion bombardment changes the surface structure of the substrate which promotes nucleation. Others suggest (Chen and Lin 1996, Stoner et al. 1993) that electron emission from the diamond coating changes the plasma composition above the substrate. Independent of the mechanism, an increased nucleation density can be beneficial in terms of a reduced film roughness and an improved film adhesion due to an increase in contact area between the layers.

2.5 Growth Rate and Quality in Thermal Plasma CVD

The interface region between the thermal plasma and the substrate plays a fundamental role in the diamond formation. When the hot plasma impinges on the cooled substrate a thin gas phase boundary layer develops near the surface. Hydrocarbon and atomic hydrogen growth precursors generated in the bulk of the plasma must pass through the thermal boundary layer by diffusion or convection without recombining or otherwise reacting if they are to contribute to the growth. In addition, important chemical species are both rapidly created and destroyed in the reacting boundary layer. Since the reactive species have a finite recombination time as they pass through the temperature gradient, the thickness of the thermal boundary layer determines the degree of super-saturation of these species above the growing film. This is different from low-pressure techniques in which only production and diffusion of the chemical species control the deposition. Figure 2.5.1 shows a photograph of the substrate immersed in stagnation-point flow in the impinging rf plasma jet, as used in the present study. The thermal boundary layer above the molybdenum substrate surface can be visually identified.

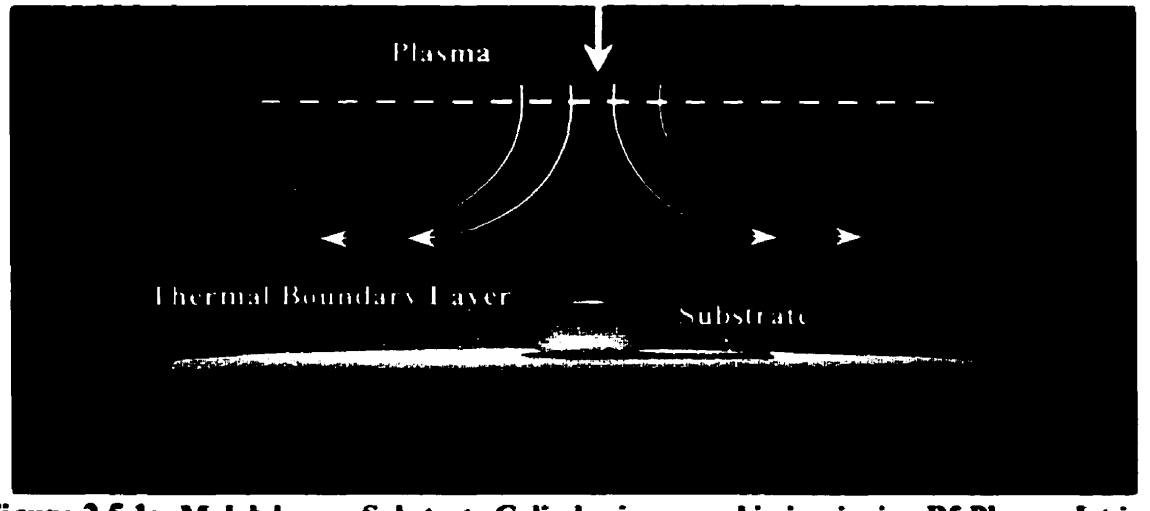

Figure 2.5.1: Molybdenum Substrate Cylinder immersed in impinging Rf-Plasma Jet in Stagnation–Point flow.

Harris et al. (1989) provided the first computation analysis of the non-equilibrium diamond growth environment. A one-dimensional kinetic analysis was used to model the gas phase chemistry that occurs during the diamond growth process. Goodwin and Gavillet (1990) and Goodwin (1989/1991) extended the model to acetylene combustion flames, dc-arcs and rf-torches to include transport phenomena by using the one-dimensional geometry of the stagnation point flow. The model by Goodwin has been readily adopted and extended by many researchers investigating the boundary layer above the growing film in thermal plasma systems (e.g. Zhang et al. 1993, Meeks et al. 1993, Yu et al. 1994, Kolman et al. 1996).

An enhanced diamond growth is generally observed when the boundary layer is made thinner by some change in operating conditions or substrate geometry (Owano et al. 1995). Girshick et al. (1993) observed a significant improvement of the diamond quality after increasing the plasma forming carrier gas flow rate in an rf-induction system. Baldwin et al. (1994) report a drastic increase in the deposition rate after reducing the throat diameter of the rf-torch exit nozzle, thereby increasing the plasma velocity. These findings support the idea that as the jet momentum is increased the boundary layer thickness (BLT) is reduced resulting in a decrease of the time available for reactive species that are created in the free stream and the boundary layer to recombine as they approach the substrate. This, in turn, promotes a higher super-saturation on the growing film, which increases the growth rate and/or diamond quality. In previous work (Oberste Berghaus et al. 1997) a decrease in boundary layer thickness from 4.5 mm to 3 mm was invoked by an increase in plasma power, which enhanced the lateral growth of individual diamond crystallites such that a smoother deposit with larger crystal faces was created in a shorter deposition time.

Practical implementation of the above mechanism to improve the diamond coating is, however, quite difficult since the thermal boundary layer is not an independent or easily adjustable process parameter but is always coupled with the plasma composition or momentum or the substrate geometry.

Recently a method has been proposed to increase the deposition rate and film quality by actively driving the boundary layer chemistry to a greater degree of non-

equilibrium via applying an electrical voltage between the substrate and an dc jet thermal plasma. Matsumoto et al. (1990/1992) induced a positive bias potential to the deposition surface in a atmospheric dc arcjet and found a twofold increase in diamond growth rate as compared to the unbiased case. Even a sevenfold increase in deposition rate in a dc jet under positive substrate bias is reported (Baldwin et al. 1995; Kruger et al. 1997). Ito et al. (1995) showed a significant improvement in the purity of the diamond phase after implementing a positive substrate bias in a dc plasma deposition system. Baldwin et al. attribute these findings to an acceleration of free electrons by the imposed electric field. The energetic electrons promote the supersaturation of radical species in the boundary layer via bond-braking collisions. In particular these electrons shift the balance of important reactions, such as hydrogen dissociation, to produce an elevated concentration of atomic hydrogen in the boundary layer. The presence of a secondary discharge in close proximity to the substrate is observed in all these cases, which indicates that the plasma chemistry in the boundary layer is indeed affected. However, under bias conditions the plasma characteristics are altered in a way that is representative for the creation of a transferred arc between the torch electrodes and the substrate surface, quite different than the bias enhanced mechanisms in low-pressure CVD.

Less or no work has been done on biasing in rf-induction thermal plasma diamond deposition systems.

EXPERIMENTAL

3. Experimental Apparatus and Measurements

3.1 Overview

The main components of the experimental apparatus are the radio frequency power supply with the induction plasma torch, the reactor chamber, including the substrate holder, gas cooler and vacuum pump, and the substrate biasing power supply. The installation also includes instrumentation for spectroscopic, calorimetric and gas flow measurements, along with pyrometric and electrical substrate measurement circuitry. Figure 3.1.1 shows a schematic overview of the experimental facility.

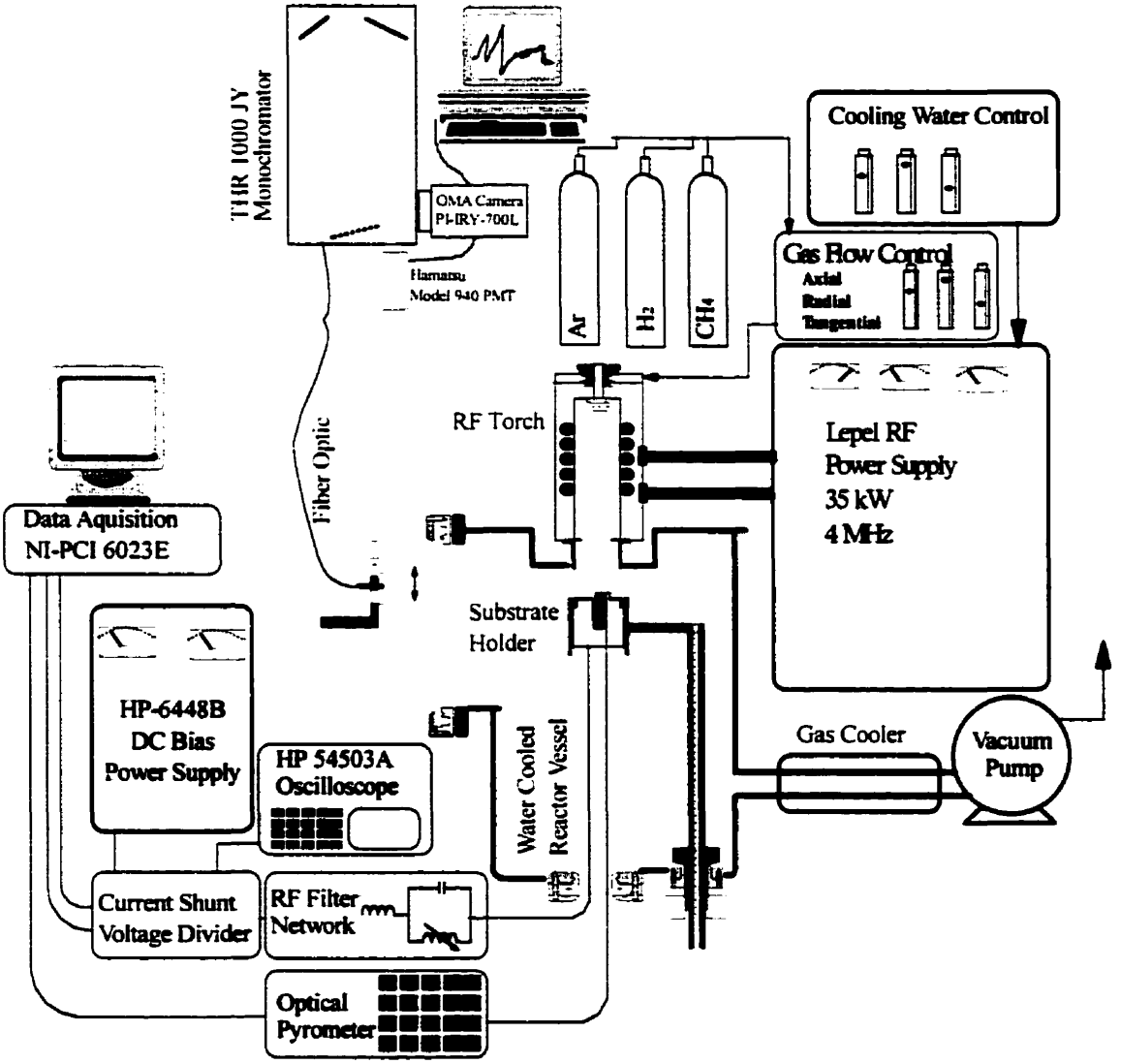

Figure 3.1.1 : Overview of Experimental Apparatus.

3. 2 Plasma Generation

The plasma is created by a standard 35 kW TAFA Model 56 rf induction plasma torch connected to a Lepel TAFA Model 32-30 MC power supply, operating at a nominal frequency of 4 MHz. The torch consists of a 3 mm thick quartz tube with an inner diameter of 3.81 cm, surrounded by a five turn copper coil. The tube and the coil are immersed in cooling water and encased in a Teflon plastic body with brass end plates. The torch has a diameter of 10.16 cm (4 in.) and a height of 24 cm (9.5 in.). The plate power of the power supply is adjusted to 31.7 kW at operation by setting the plate current to 4.4 A and the plate voltage to 7.2 kV. The Ar-H_2-CH_4 plasma gas is premixed at a pressure of 40 psi before being introduced into the torch. Precision rotameters with the tube designation 610, 603, and 602 by Matheson are used to dose the argon, hydrogen and methane flow rates at 57.56 slpm, 5.31 slpm and 0.133 slpm, respectively. The plasma gas is delivered to the top of the torch through a manifold allowing radial, tangential and axial flow injection. The tangential injection mode stabilizes the discharge, and the radial injection prevents direct contact between the plasma and the quartz tube thereby reducing tube damage. During operation the gases are injected radially, tangentially (swirl) and axially at an approximate ratio of 3:2:0.5, as controlled by additional rotameters of the gas delivery system. The gas exits the torch through a copper nozzle in the form of a tail flame.

The cooling water flow rates to the power supply and the torch are maintained at 68.5 l/min and 19.5 l/min, respectively. All cooling water circuits are individually instrumented with flowmeters and thermometers to obtain calorimetric energy balances. From these balances it is determined that 6.45 kW of the total power input of 31.7 kW exits the torch with the plasma flame and is dissipated by the reactor, heat exchanger and substrate holder cooling water. Precision mercury thermometers (±0.1°C) are installed inside the ducts to monitor the cooling water temperature rise. These thermometers are less subject to misinterpretation than thermocouples under the influence of rf interference.

3. 3 Reactor and Auxiliaries

For the present study the plasma is arranged to burn vertically in a double-walled water-cooled reactor chamber, which contains the substrate probe system (Figure 3.3.1). The cylindrical reactor is constructed from stainless steel, with an inner diameter of 25.4 cm (10.0 in.) and a height of 36.8 cm (14.5 in.). A rectangular door, supporting an optical-quality quartz window, facilitates substrate replacement and cleaning. To enhance optical access to the plasma tail flame for spectroscopic measurements the torch is positioned 2 cm off-center the reactor vessel towards the window. In addition, the torch is sunk into the top flange by 3.8 cm, and the water cooled window frame is raised to prevent the flange from blocking the view onto the nozzle exit plane.

To implement substrate biasing and to perform electrical measurements, it is found necessary to maintain all parts of the reactor equipment at a common reference potential. A common potential cannot be provided if the reactor were left floating. The base plate of the rf power supply is chosen as the common point. Its potential is referred to as ground, even though it is not necessarily at earth ground. Installing low–impedance copper ribbons to the top reactor flange, the grounded power lead, and the aluminum table minimizes any rf voltage drop through the equipment. The copper strips are six inches wide and are kept shorter than 3.75 m (one-twentieth of a wavelength at 4 MHz). All connections are either soldered or fastened with many screws across the entire width of the ribbon.

The grounded vessel shields the laboratory environment from the high-frequency electric field emitted by the plasma. In an attempt to completely enclose the noise source a grounded brass cage surrounds the torch and the power lead. In this arrangement, the grounded power lead, the brass shield, and the reactor vessel then provide return paths for the radio-frequency current.

For the rf-exited plasma there is an rf potential difference (hundreds of volts) between the plasma and the grounded environment. To prevent random arcing, caused by the flow of rf current, objects in the vicinity of the plasma must either float with the plasma potential or, if grounded, must be insulated from the plasma. To maintain a

floating object intimate electrical contact with the plasma must be ensured, and the stray capacitance of this object to ground must be minimized. This is only possible for a small object. In this experimental set-up the torch end plate and exit nozzle are left floating. The inner surface of the copper nozzle is highly polished to reduce any electrical resistance. Its stray capacitance to the grounded reactor flange is reduced by providing a Teflon spacer of at least one centimeter thickness.

The grounded reactor flange is insulated from the plasma flame by a hot-pressed boron-nitride plate, 6.5 mm in thickness and 17.8 cm in diameter, held in place by a steel ring around the nozzle. Since the plasma flame is deflected by the substrate holder to the reactor walls, an aluminum-oxide cast insulation is applied to the inside wall of the vessel. The insulating materials can withstand the harsh plasma environment. These measures are necessary to eliminate arcing problems and allow stable plasma operation.

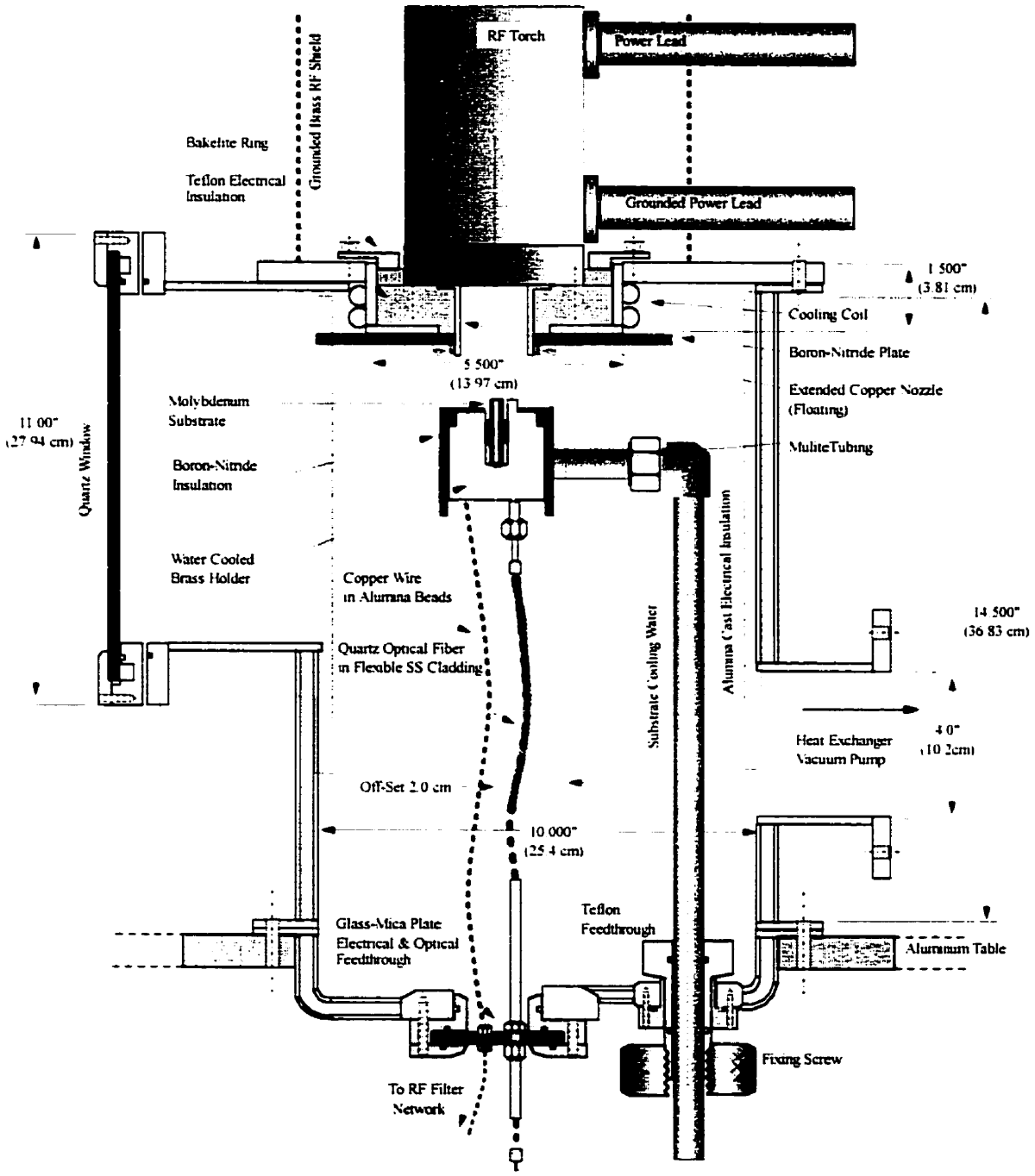

Figure 3.3.1 : Schematic of Reactor Vessel Design.

The process gases are evacuated from the main reactor unit through a water cooled shell and tube heat exchanger. 75 cm in length. The shell consists of 4" (10.16 cm) diameter stainless steel vacuum tubing, and the cooling water flows sequentially through twelve staggered 0.5" nominal copper pipes inside the shell. To force the gas flow between the tubes and to provide structural stability of the arrangement, five equally spaced copper baffles are installed normal to the tube axis. To minimize thermal stresses, the tubes are attached only at the end flange of the heat exchanger. Figure 3.3.2 shows a schematic of the heat exchanger.

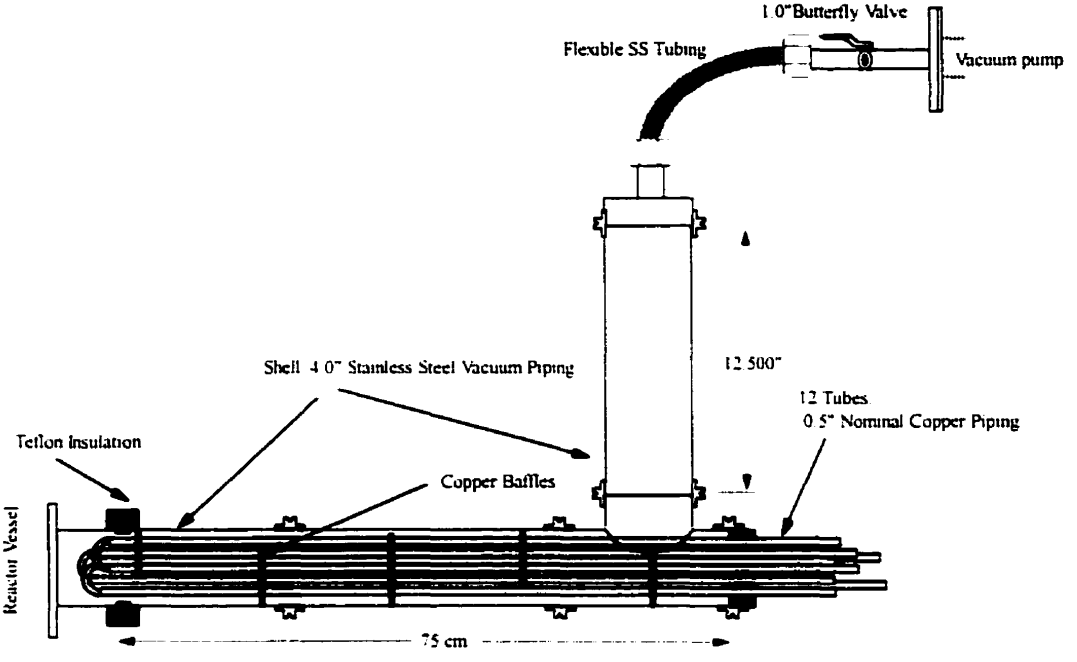

Figure 3.3.2 : Schematic of Heat Exchanger.

The ambient pressure inside the reactor is maintained at 0.3553 atm (270 Torr) during deposition by a mechanical Ruvac E116-S25 double-staged root blower/centrifugal vacuum pump from Leybold Inc., by which the reactant gases are evacuated and discharged into a fume hood. The pressure is measured through a port in the lower part of the reactor vessel by a mercury filled U-tube. The precision of this measurement is ±1 Torr. Pressure control is attained by manual adjustment of the pressure drop through a

nominal 1" butterfly valve just in front of the pump. Flexible stainless-steel tubing between the heat exchanger and the pump serves as a vibration dampener.

The photograph in Figure 3.3.3 shows a side-view of the apparatus.

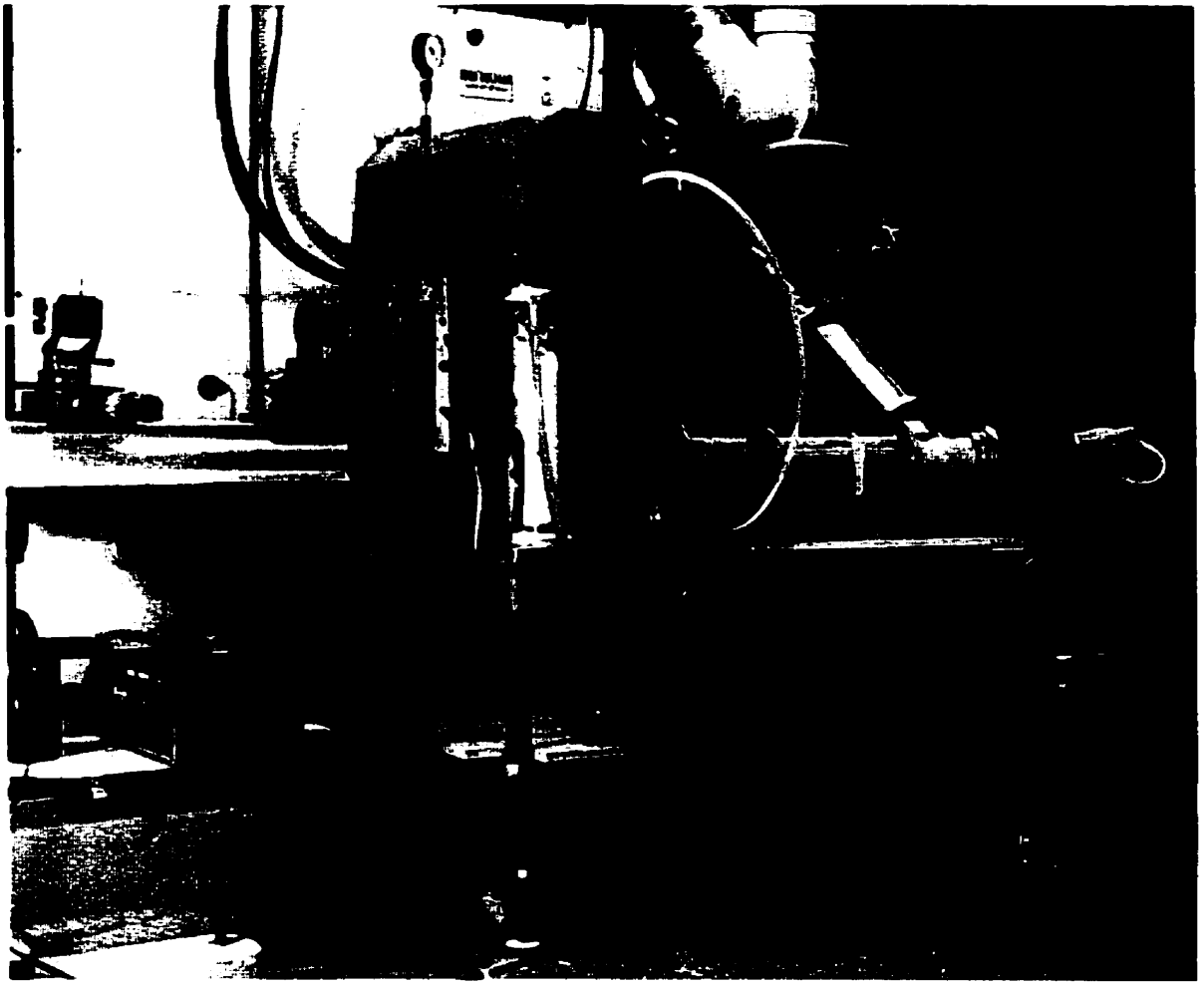

Figure 3.3.3 : Side-View of Experimental Set-Up.

3.4 Substrate Holder Design

The plasma gas leaving the torch head impinges on the substrate positioned normal to the oncoming flow. The molybdenum substrate probe is held by a water-cooled brass cylinder, which is supported by an 11 cm off-axis cantilever system supplying the cooling water. The pipe structure is introduced through the bottom flange of the reactor vessel by a Teflon feed-through. This design facilitates axial and radial positioning of the probe with respect to the plasma flame. The top of the substrate holder is placed 18 mm below the torch nozzle exit plane in all experiments. The brass cylinder is constructed of concentric tubes, fashioning conduits that channel the water throughout the holder. A high water flow rate of 5.5 l/min is maintained to prevent film boiling. Figure 3.4.1 shows a schematic of the substrate holder.

The molybdenum probe, 5 mm in diameter, is fit into a compressible copper sleeve, 14 mm in length, and sunk into a central hole in the brass (6.35 mm in diameter and 20 mm deep). A tightened set-screw secures the arrangement and ensures intimate thermal contact between the molybdenum cylinder and the brass holder through the copper sleeve. Varying the length or position of the sleeve, thereby adjusting the amount of material through which conductive heat dissipation can occur, controls the substrate surface temperature. Alternatively, the substrate length can be changed but the temperature measurement position relative to the substrate top surface is then altered.

The design incorporates a 45°-beveled quartz light pipe, which samples the thermal radiation of the substrate on its side. It terminates inside a 4 mm high brass protrusion of the holder, which shields off direct plasma radiation. This protrusion is oriented not to interfere with spectroscopic measurements close to the substrate surface. A small molybdenum ring around the substrate, having a hole aligned with the light guide, blocks reflected plasma radiation. A 600 μm quartz optical fiber transfers the signal to a pyrometer. The fiber termination, connecting to the light guide, is modified to withstand the high ambient temperature. Further information is given in a subsequent discussion on temperature pyrometry.

The substrate holder is designed to float with the rf plasma potential. It is electrically insulated from the reactor unit by alumina and PVC water ducts. To confine direct electrical contact with the plasma to the substrate surface area, a hot-pressed boron-nitride insulator covers the substrate assembly. The top plane of the brass holder facing the plasma, along with the thin (1mm) boron-nitride dielectric layer, constitute a shunt capacitance, which reduces rf currents from the plasma to the probe. To maintain electrical insulation throughout an experiment, it is found necessary to provide a small spacing between the thin BN plate and the brass, since a conducting carbonaceous coating forms. The electrical considerations are further addressed in section 3.7.

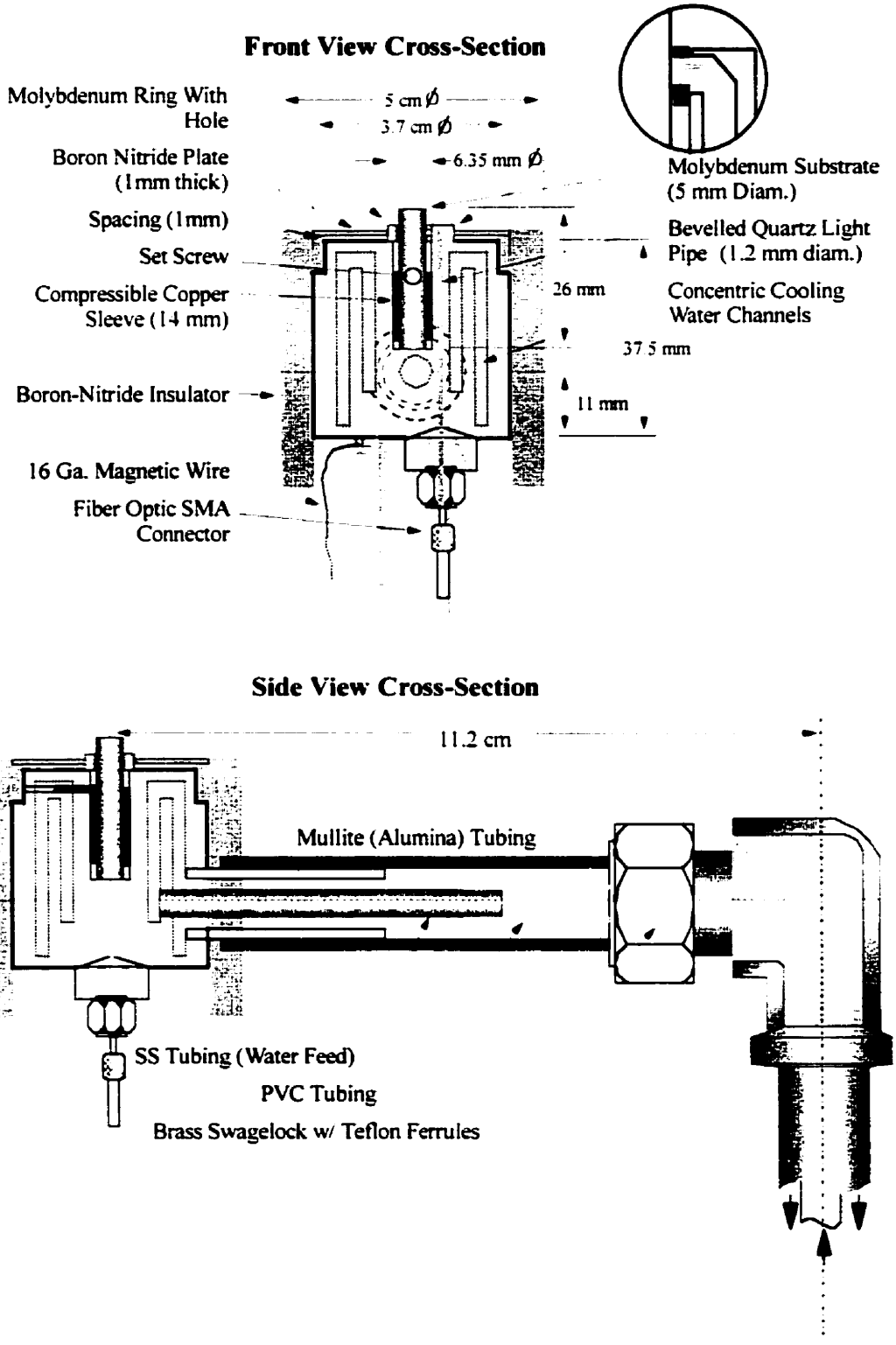

Figure 3.4.1 : Schematic of Substrate Holder.

3.5 Substrate Temperature Pyrometry

Substrate temperature is known to be an important parameter in chemical vapor deposition of diamond. In this study it is imperative to control and measure the surface temperature of the substrate during deposition. For the temperature measurement, the principle of radiation pyrometry is applied. Pyrometry is a practical application of Plank's law, which relates the radiation emitted by an object to its temperature. Using Wien's approximation, the intensity at wavelength λ is related to the temperature T of an object with emissivity ε by

$$I = \frac{2\pi hc^2\varepsilon}{\lambda^5 \exp\left(\frac{hc}{\lambda kT}\right)} \tag{3.5.1}$$

.where h is Plank's constant, c is the speed of light, k is the Boltzmannn constant.

In the plasma environment of a CVD deposition reactor, the use of conventional pyrometric methods is limited by several factors. The emissivity of the surface changes drastically as the polished molybdenum gets coated with diamond. To avoid this difficulty, two-color pyrometry can be used, which relates the intensity ratio at two wavelengths to the temperature, assuming equal emissivity. Bieberich et al. (1996) illustrates, however, that deviation from gray-body behavior, as in the case of molybdenum, can introduce large errors. A strong interference is also caused by the plasma radiation, which may reach the detector directly or may reflect off the substrate. A common technique is to measure the substrate radiation after shutting off the plasma and extrapolating the temperature during the experiment from the resulting cooling curve (Oberste Berghaus 1996). However, this method does not allow in-situ monitoring and requires highly reproducible start up conditions.

Bieberich et al. (1996) describes a radiation measurement from the backside of the surface. This approach is adapted to our geometry. The radiation of the molybdenum substrate is collected on its side, some 5 mm below the top surface, by a beveled fused quartz light pipe, 1.2 mm in diameter, as described earlier. At this location, changes in surface emissivity due to carbon deposition are negligible. The light path is entirely

contained, thereby shielded from direct and reflected plasma radiation. The signal is conveyed through a fiber to a single-color Accufiber Model 100C Measurement System. The photodiode detector operates at a wavelength of 950 nm. An emissivity $\varepsilon = 0.33$ of the molybdenum surface is taken from the literature (Touloukian 1970), as measured for 600 Grid polished molybdenum at a wavelength of 0.98 μm and a temperature of 1600 K. At the measurement location the molybdenum cylinder is polished to match these surface conditions. Transmission losses through the optical path as well as the light collection solid angle are calibrated against a sapphire lightpipe sensor with known attenuation, using various light sources. From these measurements an attenuation factor of 0.8 at 950 nm is determined and used in all experiments. Even though the actual deposition surface temperature must be deducted from this indirect measurement, the problems of changing surface conditions and plasma radiation are avoided. More importantly, the measurement is very robust and allows in-situ monitoring of the substrate temperature during deposition. The Accufiber System allows a 4-20 mA analog output, which is recorded by a data acquisition system described later.

3.6 Heat Flux Measurement

The molybdenum substrate is heated by conduction and convection from the impinging plasma jet, and cooled by conduction to the water-cooled substrate holder. The substrate temperature is measured by the pyrometric technique developed and described earlier. The temperature can be controlled by varying the axial position of the copper sleeve, thereby adjusting the effective length of the molybdenum cylinder through which the heat is conducted to the water cooled base. Neglecting radiative cooling and assuming that most of the heat flux comes through the normal oriented deposition surface, the temperature can be expressed in terms of the heat flux through the cylinder by Fourier's law in the following form:

$$\frac{\Delta T}{\Delta x} = \frac{Q}{Ak} \qquad (3.6.1)$$

, where ΔT is the difference in temperature between two points along the cylinder separated by a distance Δx, A is the area of the normal surface ($A = 1.963 \cdot 10^{-5} m^2$) and Q

is the heat flux in W. The thermal conductivity k is assumed constant at 105 W/m·K at a molybdenum temperature of 1200 K (Perry's Handbook 1984). At standard plasma operating conditions, the temperature is varied by sliding the 14 mm copper sleeve to different axial positions along the substrate. Figure 3.6.1 shows the measured temperature as a function of relative sleeve position. The heat flux to the substrate is evaluated from the slope of the line fitted by the least-square method. The heat flux to the substrate is approximately 45.5 W.

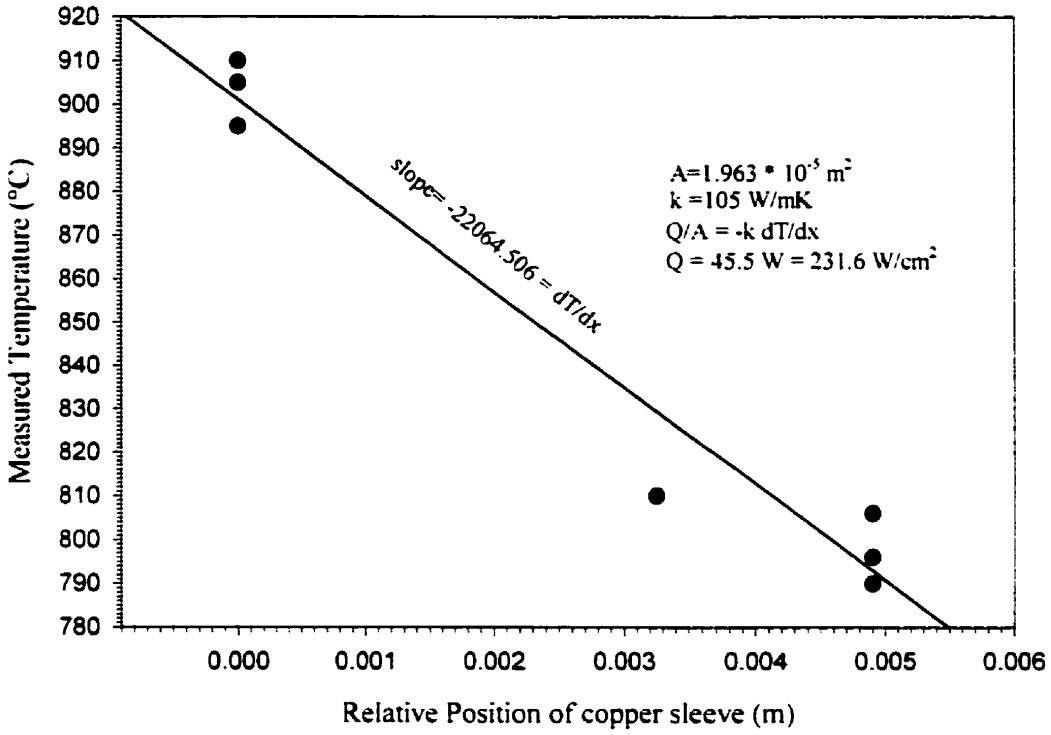

Figure 3.6.1 : Heat Flux Measurement at Standard Plasma Conditions.

3.7 RF Problems and Bias Circuit Design

The strong radio-frequency signal generated by an induction thermal plasma system generally imposes severe constraints on the process control and on the kind of attainable experimental measurements. The problem arises not only from the high residual rf voltage of the plasma flame itself but also from the strong emitted electric and magnetic rf fields, which interfere with any electrical equipment in the vicinity of the plasma generator (EMI). In fact, it is often necessary to place even unconnected electronic equipment many meters away from the system. In the following, a circuit is presented which allows the application of a dc potential difference between the substrate probe and plasma in which the probe is immersed. The main concern is that the rf voltage drop across the plasma-probe junction is small, if not eliminated, such that little or no rf current flows into the dc biasing power supply, possibly causing loss of regulation and damage. Furthermore, conducted and radiation pick-up induced rf current must be alleviated to such a degree that the dc current and voltage in this circuit can be accurately measured and electronically recorded.

When a probe is immersed in an rf plasma an rf voltage will develop across the plasma probe junction if the probe voltage differs from the plasma voltage. Historically, this problem arises in Langmuir probe diagnostic studies in low-pressure capacitive-coupled glow discharges, where the rf current and its rectification in the plasma-probe boundary (sheath) causes distortion in the characteristics. A possible technique is to carefully sample the plasma voltage and then actively applying the same voltage on the probe. Typically, the sampled signal is phase and amplitude adjusted before being reapplied. Mismatch between the probe and plasma potential waveforms is still likely due to differences in harmonic content. Another drawback of this active compensation method is the very complex experimental arrangement required (Braithwaite et al. 1987, Mizumura et al. 1992, Špatenka et al. 1992). An alternate approach, developed by Gagné and Cantin (1972), reduces the rf currents though the sheath by letting the probe float with the plasma such that the time varying plasma potential effectively drives the probe potential. The electrical connection to ground, required to apply a dc bias, then contains a

decoupling device of high impedance with respect to the rf component (Paranjpe et al. 1990. Dilecce et al. 1991). This passive scheme is adapted to our high-power induction plasma situation. Figure 3.7.1 illustrates the idealized condition, in which the probe voltage matches the plasma voltage in waveform, frequency, amplitude and phase, and an offset is superimposed, representing the dc bias voltage difference.

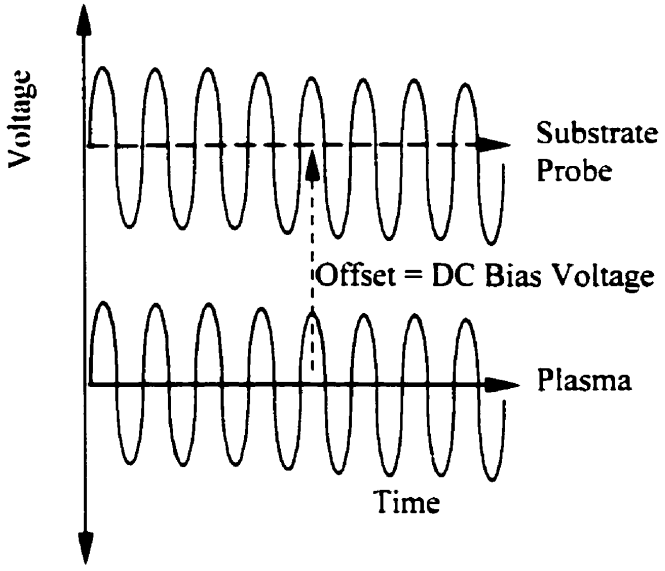

Figure 3.7.1 : Schematic of Time-Variant Probe Voltage.

Figure 3.7.2 gives the ac equivalent circuit, where the plasma voltage is symbolized by an ac and dc power source, and resistive/capacitive components represent the sheath impedance. Direct current continuity from the biasing power supply to the probe is maintained through a passive filter, consisting of a tunable L-C circuit trap in series with additional chokes.

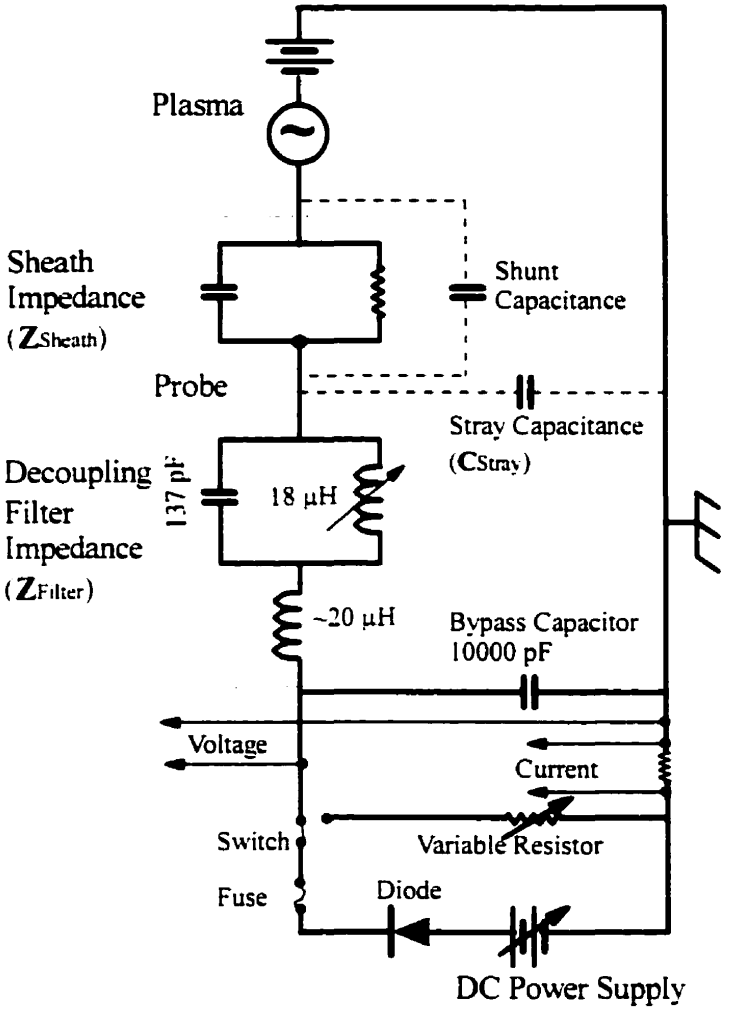

Figure 3.7.2 : AC equivalent bias circuit diagram.

To eliminate rf currents through the circuit, the sheath impedance must be small such that there is little voltage drop across the plasma-probe junction, and the filter impedance must be very large to decouple the probe from the grounded environment at

the rf frequency. In addition, a small stray capacitance to ground is desired. Ideally, a decoupling filter with small circuit elements very close to the substrate is preferred, since both the filter components and the connecting wire contribute to the stray capacitance. This criterion is compromised in our design, since physically large circuit elements are required to sustain the large rf voltage drop of over 1000 V in our system. This also takes the circuit outside the reactor vessel, requiring a long connecting wire. However, a small diameter wire (16 gage) is chosen to minimize its capacitance to ground. The wire is fed to the substrate through an insulating glass-mica plate. In an attempt to reduce the sheath impedance while limiting the dc contact with the plasma to the probe surface area, the area of the substrate holder, which is covered by a thin dielectric, is intentionally kept large to provide a shunt capacitance. This capacitance amounts to approximately 40 pF with a dielectric constant of K = 4.0 for boron-nitride.

The major decoupling is provided by an L-C parallel circuit, resonance tuned to the main rf frequency according to $$f_{reson} = \frac{1}{2\pi\sqrt{LC}}. \qquad (3.7.1)$$

Ceramic disk capacitors (5 kV peak-voltage rating), available from Dralonic Inc., add to a capacitance of 137 pF. Small capacitor values allow lower phase-shifted current in the parallel circuit. The loss factor in the coil, which governs the overall impedance of the trap, is thereby kept low. At 4 MHz resonance and ±1000 V peak voltage the inductance is L = 11.5 μH, and the current in the trap is I_{rms} = 2.35 Amp (root-mean-square). Resonance is attained by a tunable air-core inductor with a maximum inductance of 18 μH. This 27-turn coil, 15 cm long and 7 cm in diameter, has a current rating of 5 A and is commercially available from Cardwell Condenser Inc.. Its inductance is varied by the number of active turns. The linear characteristics of an air core inductor, as opposed to a magnetic core device, facilitate tuning. An air core is also preferred because it does not saturate at the high current load and is far less susceptible to magnetic fields. A 34-turn air-core choke (11 cm long and 6 cm in diameter), in series with the trap, provides additional decoupling. Although its 20 μH inductance is small, the design ensures very low internal capacitance, which most often governs the impedance of chokes at MHz frequencies. To reduce the rf signal even further, a 3 cm diameter ferrite torrid is placed

after the choke. A ceramic disk capacitor (10000 pF, 5 kV) acts as an rf bypass. The assembly is installed just below the rector vessel and mounted on a low impedance copper plate, grounded to the rf power supply base. The filter components are individually shielded by aluminum casings to prevent cross-talk. The bias voltage is generated by a Hewlett Packard DC Power Supply SCR-1P Series Model 6448B, with a 600 V and 1.5 A rating, which can be operated in current and voltage control. A fuse protects against current overload, and a diode prevents reverse current loading. To make measurements in the quadrant of opposing sign (i.e. positive current and negative voltage) with a one-polar power supply, a variable resistor (1400 Ω) can be connected. The single point ground of the circuit is located at the copper plate. A coaxial cable connects the power supply. The outer conductor of this cable carries the return current. Besides providing EMI shielding, this arrangement reduces the area of the magnetic field receptor loop created by the circuit.

Rf voltages are measured with a Hewlett Packard 54503A (500 MHz) digital oscilloscope in conjunction with a Hewlett Packard 82335A HP-IB interface to an IBM-compatible PC. Using a Tektronix P6015 1000:1 High-Voltage Probe, rf voltages are measured on the floating torch exit nozzle during operation. The resulting signal, which is taken to represent the plasma voltage, features a sine wave of 2100 V (peak-to-peak) at 4.063 MHz with little harmonic content. Using this 1000:1 attenuation probe, the substrate voltage is measured on the connecting wire outside the reactor. A smaller HP 10430A 10:1 attenuation probe is employed to measure the circuit rf voltage after the filter, leaving the bypass capacitor unconnected. The voltages before and after the tuned filter are compared in Figure 3.7.3. The substrate peak voltage of $V_{pp} \approx 2000$ V illustrates that the substrate effectively follows the time-varying plasma potential. The well-defined waveform with little harmonic content justifies the use of a notch-filter decoupling device. The filter is evaluated in terms of the insertion loss, defined by I.L. = 20 $\log_{10} V_1/V_2$. The high insulation of I.L. = -60 dB indicates effective decoupling of the probe from the grounded environment. The signal after the filter that reaches the power supply is essentially dc. Its rf component is even further reduced when the bypass capacitor is connected.

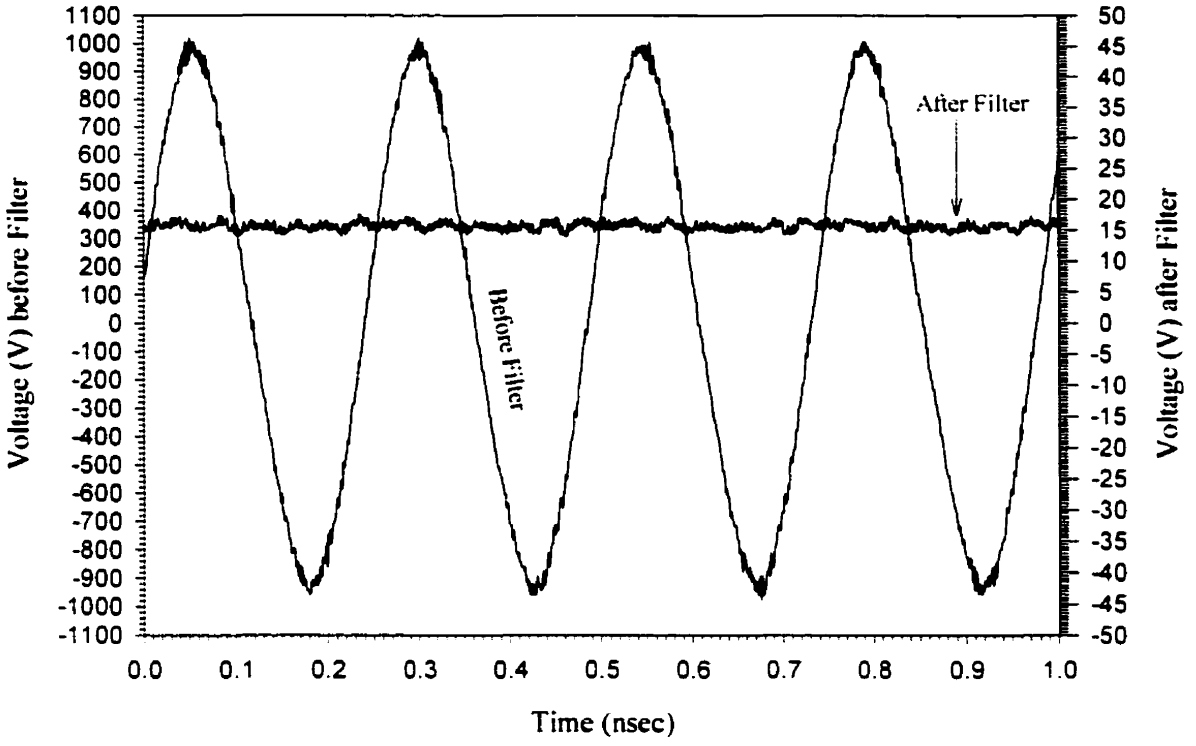

Figure 3.7.3 : Voltage measured on substrate connection before (1000:1) and after (10:1) tuned filter. Frequency = 4.063 MHz.

In practice the filter is not tuned during plasma operation but on an electronically reproduced signal. To continuously monitor the residual rf noise, the oscilloscope is ac coupled to the bias circuit during experimentation.

3.8 Current-Voltage Measurement and Data Acquisition

The dc voltage is measured through a 60:1 voltage divider with a total resistance of 101.7 kΩ, producing a 10 V signal at full range (600V). The voltage drop through a 1 Amp shunt resistor, creating a 0 to 50 mV signal, measures the dc current in the circuit. The low voltage drop ensures low power dissipation. Since the current shunt in the bias circuit is positioned on the grounded side of the dc power supply, the sign of the current must be corrected. The current is defined as positive when it flows from the substrate into the plasma. Analog panel meters display the readings. The devices are enclosed in a grounded aluminum casing. A National Instruments PCI-6023E Data Acquisition System mounted on an IBM-compatible PC records the measurements. Particular consideration is given to prevent rf currents to reach the electronic equipment. The signals are transferred to the computer by shielded-twisted pair cables. The twisted-pair protects against common mode magnetic pick-up, and the shield guards against capacitive pick-up. Corcom 1VB3 EMI filters are installed on each end to reduce conducted common-mode rf noise. The computer ground differs in potential from the bias circuit ground (rf power supply base). To avoid any ground loops, the cable shield is grounded only on the computer side. The difference in reference potential makes a differential input configuration necessary, and the current and voltage connections are treated as floating signal sources. In this configuration the PGIA (Programmable Gain Instrumentation Amplifier) also rejects some common-mode noise, provided that the input signals are within ±11V of the computer ground. Additional measures to remove rf pickup by the leads include bypass capacitors and ferrite beads employed in such a way that the signal paths are balanced. Besides bias voltage and current, the system also records the measured substrate temperature. The 4-20 mA analog output of the pyrometer is translated into a 0-10V signal and transferred to the data card. The data are logged to file at 10 Hz or 5 Hz sampling rates.

The rf mitigation techniques used in this experimental setup with respect to grounding, shielding, layout, component and material selection are discussed by Ott (1988), Taylor (1971), Kodali (1996) and Fish (1994).

3.9 Substrate Material and Preparation

The substrate is a 5 mm diameter molybdenum rod, with a purity of 99.97%, available from Alfa Aesar. The average grain size is 3.2 μm, as measured by optical microscopy in Figure 3.9.1. For this measurement the final polish is made with 0.3 μm Al_2O_3 paste. The surface is etched for 20 seconds with Murakami's reagent (15 g $K_3Fe(CN)_6$, 2 g NaOH in 100 ml water, from Metals Handbook, 8th Editon, 1998) to expose the grain boundaries.

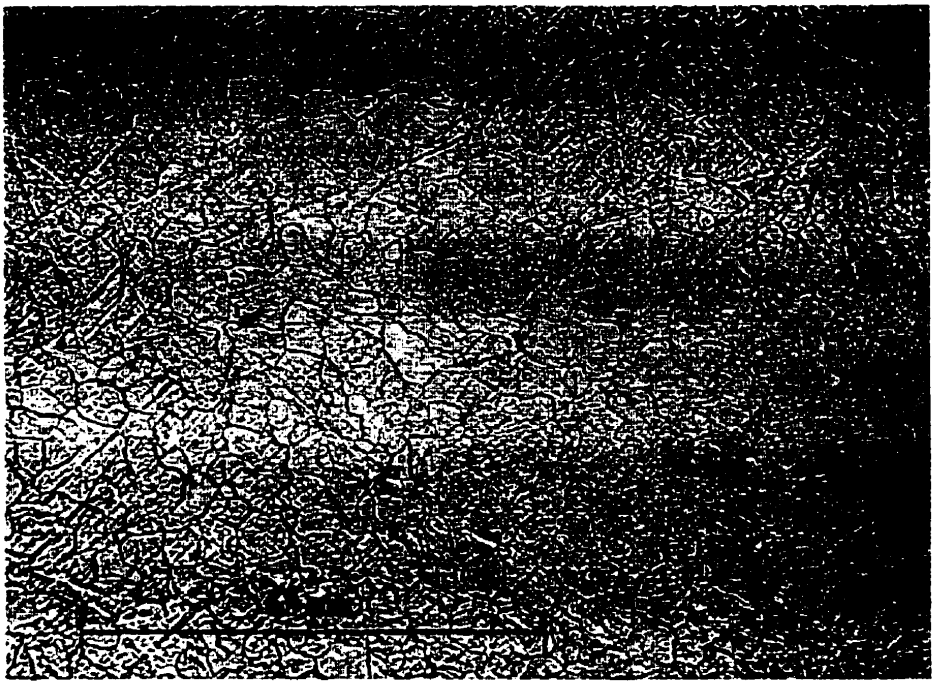

Figure 3.9.1 : 200 X magnification of polished and etched molybdenum substrate surface for grain boundary resolution.

The Molybdenum substrate after being cut to length is polished on its deposition surface with 260 Grid and 600 Grid wet silica paper and then with 6 micron polycrystalline diamond suspension (on Vicker paper). To ensure reproducible surface emissivity for the pyrometric measurement, a 600 Grid final polish is applied on the sides of the molybdenum cylinder. Possible residues are washed off in an ultrasonic methanol bath in which the substrate is submersed for 20 minutes. Any oxides that may have formed are removed by exposing the substrate to an argon-hydrogen plasma for at least 30 seconds before deposition.

3.10 Experimental Procedure

The prepared substrate is mounted in the substrate holder and positioned in the center of the plasma flame, such that the substrate surface is 1.5 cm below the torch exit plane. The start-up procedure is routine and accomplished in the following manner. The rectifier voltage is activated and allowed to go through a 20 minute warm up cycle. The cooling water temperature is noted. The reactor is evacuated and then purged with argon at a flow rate of approximately 25 slpm for one minute. The plate power is then applied with the plate current not exceeding one ampere in order to lessen erosion effects inside the torch. The ratio of tangential to axial argon injection during start up is 2 to 1. At a pressure of approximately 10 to 15 Torr (~0.015 atm.) a corona discharge is formed at this point. Adjusting the butterfly valve increases the ambient pressure. Increasing the power then allows the argon plasma to form. Adding argon through the radial and tangential injection ports and readjusting the pressure to 270 Torr (0.355 atm.) then establishes the final argon gas flow rate. Addition of hydrogen requires a higher sustaining power and drastically increases the impedance of the plasma. The hydrogen is consequently added incrementally, while the power is gradually increased and the grid current tuning continuously adjusted. Increasing the power on the pure argon plasma results in a fire-ball too large to be contained in the torch, damaging the equipment. The higher hydrogen plasma impedance forces the current through the power supply grid, causing current overload if the grid impedance is not increased simultaneously. With the full argon and hydrogen flow the final plate current of 4.4 A is then attained. The argon hydrogen plasma is maintained for the period required to start the data acquisition system, which is left unconnected until the plasma has reached stable operation. Possible arcs during startup and the associated current spikes are thereby prevented from damaging the electronics. Finally, the methane is mixed into the process gases and the grid is adjusted to a plate voltage of 7.2 kV. If pertinent, the biasing power supply is now turned on to apply the desired bias voltage. The plate current and voltage along with the cooling water flow rates and temperature rises are recorded. The deposition time is taken form the moment of opening the methane valve. The plasma is shut down by simply interrupting

the plate current. The hydrogen and methane valves are then closed, and the reactor is purged with argon before the vessel is opened and the deposited sample removed for further analysis.

3.11 Post Deposition Analysis

The produced deposits are visually inspected under an optical microscope with a magnification of 40. The microstructure, film thickness, grain/crystal size, coverage and nucleation density are discerned by micrographs of the deposit obtained in a JOEL JSM-840 Scanning Electron Microscope (SEM) in conjunction with a LECO 2005 Image Analysis System. Micro Raman Spectroscopy is performed on some samples to characterize the quality of the deposit. With Raman Spectroscopy, diamond, which has a phonon density of states very different from other carbon phases, can be detected without any ambiguity (Bonnot 1990). A green argon laser at 541nm is the excitation source in a Renishaw 3000 Ramascope, with a spatial resolution of 1 micron.

3.12 Optical Emission Spectroscopy

Optical Emission Spectroscopy (OES) measures the intensity of radiation emitted by the plasma as a function of wavelength. Plasma parameters such as temperature and species densities can be deduced from the spectroscopic observation if the plasma is assumed to be in the state of Local Thermal Equilibrium (LTE). Under this assumption, the energy transfer processes within the discharge are dominated by collisions and energy states of the gas species are normal distributed. Spectroscopic observations can be interpreted in terms of the Boltzmann equation for the energy distribution to yield plasma temperatures. In $Ar/H_2/CH_4$ thermal plasmas conventionally used for diamond deposition, a deviation from LTE is commonly reported. An increased electron density above the Saha equilibrium value at the gas temperature is usually seen and can be attributed to the finite electron-ion recombination rate within the plasma (Baldwin et al. 1994). Lower excitation states of the heavy species are little affected and can be assumed to obey LTE (Kruger et al. 1997). The rotational temperature can be taken as the kinetic gas temperature because of the low energies involved in the rotational processes. Rotational equilibrium of the gas molecules is likely, and measurements of relative intensity of rotational lines will in principle reflect the overall gas temperature (Mermet et al. 1978). Excited level populations are generally used to approximate the electron temperature. In the jet recombining plasma, the relaxation time of an exited level population is much shorter than the time of ionization-recombination relaxation. Consequently, excited level populations and their corresponding temperature can still be used to yield the plasma electron temperature, or at least its relative spatial changes (Bousrih et al. 1995).

The temperature determination from the spectroscopic measurements is based on the Boltzmann plot method, using relative line intensities. The intensity of a spectral line for the transition between an upper and lower energy level can be formulated as

$$I = \left(\frac{h\nu}{4\pi}\right) \cdot A n_K \qquad (3.12.1)$$

where A is the transition probability (sec^{-1}), $\nu = c/\lambda$ is the wave number of the line, and n_K is the number density of the species at the upper level. At equilibrium, the Boltzmann distribution equation allows to relate the population of the exited species to the total number density n of the ionization state:

$$n_K = \frac{n}{Q(T)}\left[g_K \exp\left(\frac{-E_K}{kT}\right)\right] \qquad (3.12.2)$$

where g_K denotes the statistical weight of level K, E_K the energy and $Q(T)$ is the partition function. The partition function is a summation of the Boltzmann factors for all bounded energy levels of the species. The resulting equation can be expressed as:

$$\ln\left(\frac{I\lambda}{gA}\right) = -E\frac{hc}{kT} + C \text{ .with C being a constant.} \qquad (3.12.3)$$

The temperature can be derived by plotting ln (I / S) versus E, with the line strength $S = gA / \lambda$, obtaining T from the slope.

The gas temperature is inferred from the rotational temperature, which is determined from the Swan band spectrum of the C_2 molecule in the wavelength range of 5129.2 Å to 5165.2 Å. The electron temperature is deduced from the excitation temperature, measured from the hydrogen Balmer Series lines. The electron density is determined form the Stark broadening effect on the H_β line at 4861 Å. This last diagnostic does not depend of the LTE assumption, and the electron density can be evaluated independent of the equilibrium state of the discharge.

The light emitted by the plasma is imaged through a quartz window by a double achromat lens with an aperture of f/4 and f = 20 cm with a one-to-one magnification. Light is collected by a fused silica single optical fiber set in horizontal position, yielding a 200-μm spatial resolution in the plasma perpendicular to the optical axis. The lens is placed 40 cm from the center of the torch exit nozzle parallel to the window and the

image plane 40 cm from the lens. The optical fiber can be precisely positioned along the vertical z-direction in the image plane to monitor the axial variation of emissivity in the tail flame and the boundary layer above the substrate; as well as along the horizontal y-direction to collect the line-of-sight radiation at different distances from the axis of the plasma cone (Figure 3.12.1). The emission signal is selected by a THR-1000 monochromator (ISA division Jobin Yvon) with 1-m focal length and a grating of 1800 grooves/mm. Variable slit width are used for the emission measurements. A Hamamatsu model R928 photomultiplier tube (PMT) is mounted at the exit slit monitoring the emission intensity. Alternatively, a Princeton Instruments 1024-pixel charge-coupled device (CCD) diode-array model IRY-700L is used to record the spectral image. With the monochromator dispersion of 4.8 Å/mm and a pixel size of 25 μm, the CCD resolution is 0.12 Å/pixel. The intensity readings are transferred to a laboratory computer and recorded for processing.

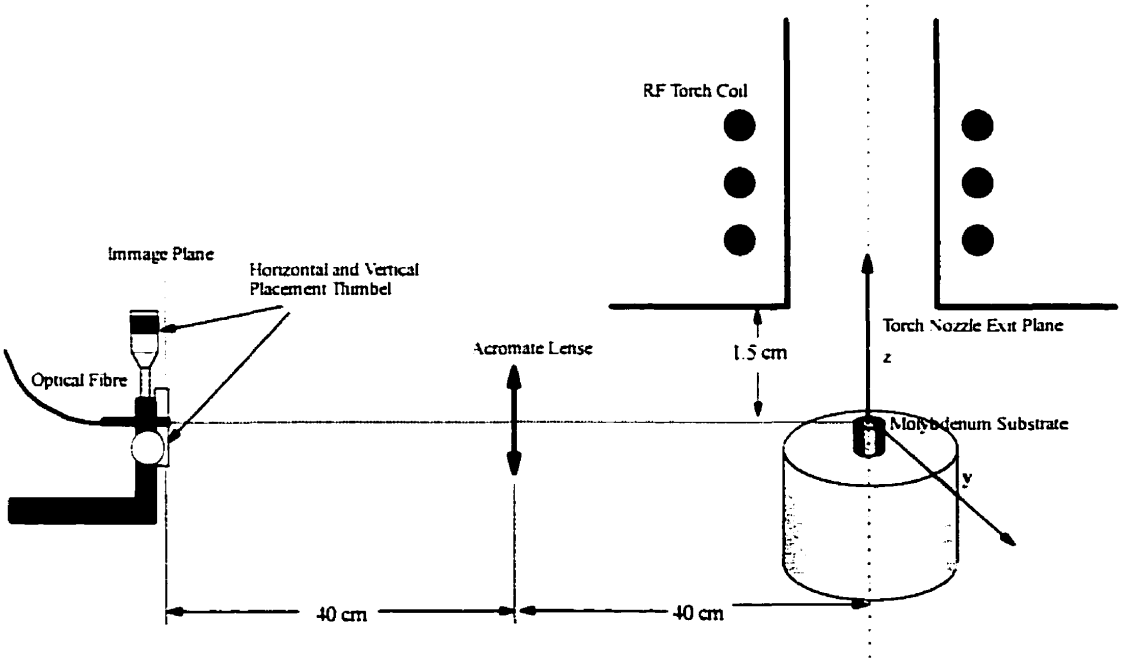

Figure 3.12.1 : Schematic of Optical Set-Up.

3.12.1 Rotational Temperature Measurement

The spectrum of the distinct C_2 Swan band emission is observed in the $Ar/H_2/CH_4$ plasma. The spectrum originates from vibrational and rotational excitation of the molecule. The spectra are recorded using the CCD diode array centered at 5140 Å. A much finer resolution can be obtained with the PMT in conjunction with a small slit, with the drawback that the acquisition takes an appreciable amount of time. Due to plasma fluctuations and drift which can significantly distort the spectrum a CCD measurement for which the intensity at all wavelengths is recorded simultaneously is preferred. The exposure time is 10 milliseconds in this measurement.

The rotational temperature is calculated by using the peak intensities of the rotational lines K''= 47 to K''= 35 in the P-branch of the v(0-0) $A^3\Pi_g$-$X^3\Pi_u$ Swan system. The lines and their corresponding wave numbers are identified using the results of Adler and Mermet (1973) and Bleekrode and Niewpoort (1965). The values for the line strength and the rotational energy are calculated by formulae by Adler and Mermet (1973) and Gaydon and Wolfhard (1950), based on "Spectra of Diatomic Molecules" by G. Herzberg.

$$\ln\left(\frac{I}{S}\right) = D + \nu^4 - E_r \frac{hc}{kT_r} \qquad (3.12.4)$$

where the coefficient D contains the rotational partition function, the statistical weight and the universal constants. S is the line strength of the emission incorporating the transition probability (Mermet et al. 1978). E_r is the rotational energy of the upper level of the line.

The line strength is given by: $$S = \left|(K'+1)^2 - 1\right| / (K'+1) \qquad (3.12.5)$$

and the rotational energy : $$E_r = B'K'(K'+1) \qquad (3.12.6)$$

where, I = Intensity of the line; D = constant;

K' = rotational quantum number of the upper rotational state = $K'' + 1$ for the P branch.

B' = rotational constant for the upper vibrational state (1.7443 cm^{-1})

ν = wavenumber of line (considered a constant)

A typical spectrum from the plasma emission acquired in line-of-sight is shown in Figure 3.12.2. The quantum number designation is indicated.

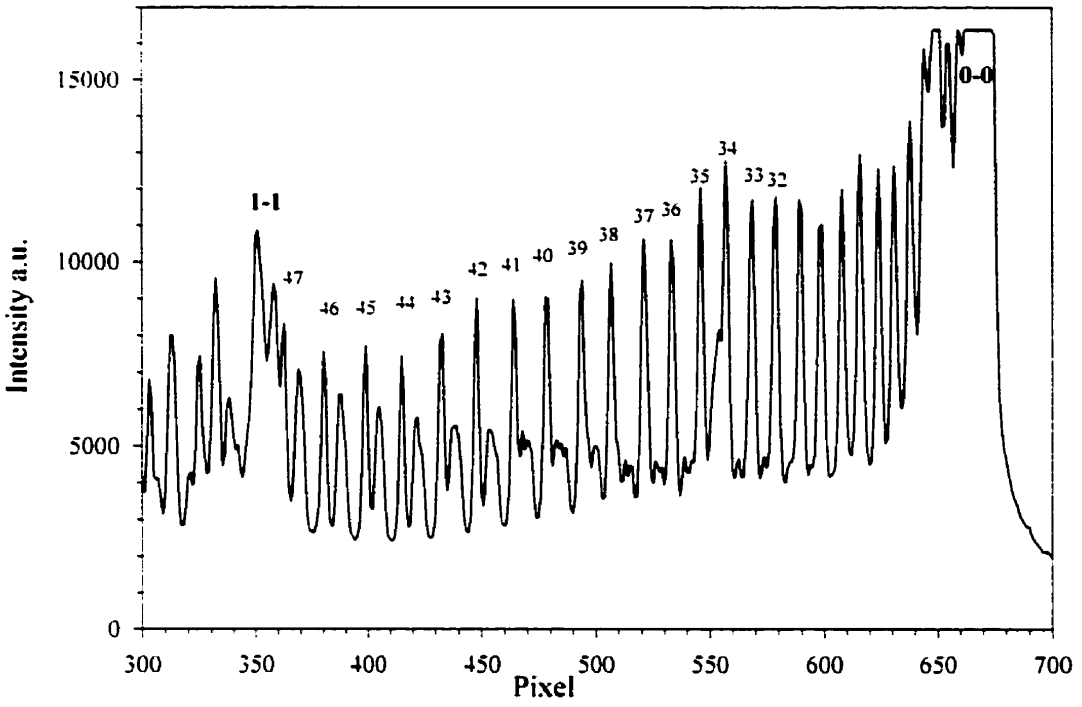

C_2 Swan Band resolved with CCD Array, 10 msec. integration time;
0.12 Å/pixel. K"=47 at 5150.645 Å and K"=36 at 5129.682 Å.
Line-of-sight measurement: 6 mm above substrate surface.

Figure 3.12.2 : Line-of-sight Swan band emission acquired with CCD diode array.

3.12.2 Excitation Temperature Measurement

The excitation temperature is derived from the emission of the first four members of the hydrogen Balmer transitions (H_α, H_β, H_γ, H_δ). The excitation of atomic hydrogen is used because the transition probabilities are accurately known. The relationship between line intensity at level j and excitation temperature is given by

$$\ln\left(\frac{I_j \lambda_j}{g_j A_j}\right) = -E_{j\,ext}\frac{hc}{kT_{ext}} + C \qquad (3.12.7)$$

A graph of $\ln(I_j\lambda_j/g_jA_j)$ versus E_{jext} yields a straight line at equilibrium with the slope of hc/kT_{ext}, from which the temperature is obtained. Table 3.12.2 summarizes the values for the relevant transitions, taken from Mermet (1978).

Table 3.12.2: Summary of the electronic transition, wavelength, statistical weight, and excitation energy of the H atom Balmer series.

Transition	Wavelength λ (nm)	Statistical Weight g_j	Transition Probability A (sec^{-1})	Excitation Energy E_{ext} (m^{-1})
H_α 3n-2n	656.3	18	$0.4410 \cdot 10^8$	9,749,200
H_β 4n-2n	486.1	32	$0.08419 \cdot 10^8$	10,282,400
H_γ 5n-2n	434.0	50	$0.02530 \cdot 10^8$	10,529,200
H_δ 6n-2n	410.2	72	$0.009732 \cdot 10^8$	10,663,200

The emission intensities are measured with the CCD diode array with an exposure time of 10 milliseconds. To mitigate plasma fluctuation effects, two consecutive frames are recorded. Since the emission wavelengths are far apart, the diode array, covering a spectral width of 123 Å, cannot capture the lines simultaneously, and the monochromator grating has to be moved for each transition to the respective central wavelength. The slit width is adjusted to full intensity range of the detector. The emission intensities of the lines are very different. It is not found possible to obtain a sufficient H_δ signal without overexposing the diode array at H_α, while maintaining the same light sampling

conditions. Consequently, the intensities of only three consecutive lines are recorded for a given experimental measurement (e.g. H_α-H_β-H_γ or H_β-H_γ-H_δ). Figure 3.12.3 shows examples of measured spectra with the light collection adjusted to the intensity of the strongest emitting line. The strong broadening of the lines requires integration of the peak area (with the continuum radiation subtracted) to obtain intensity values.

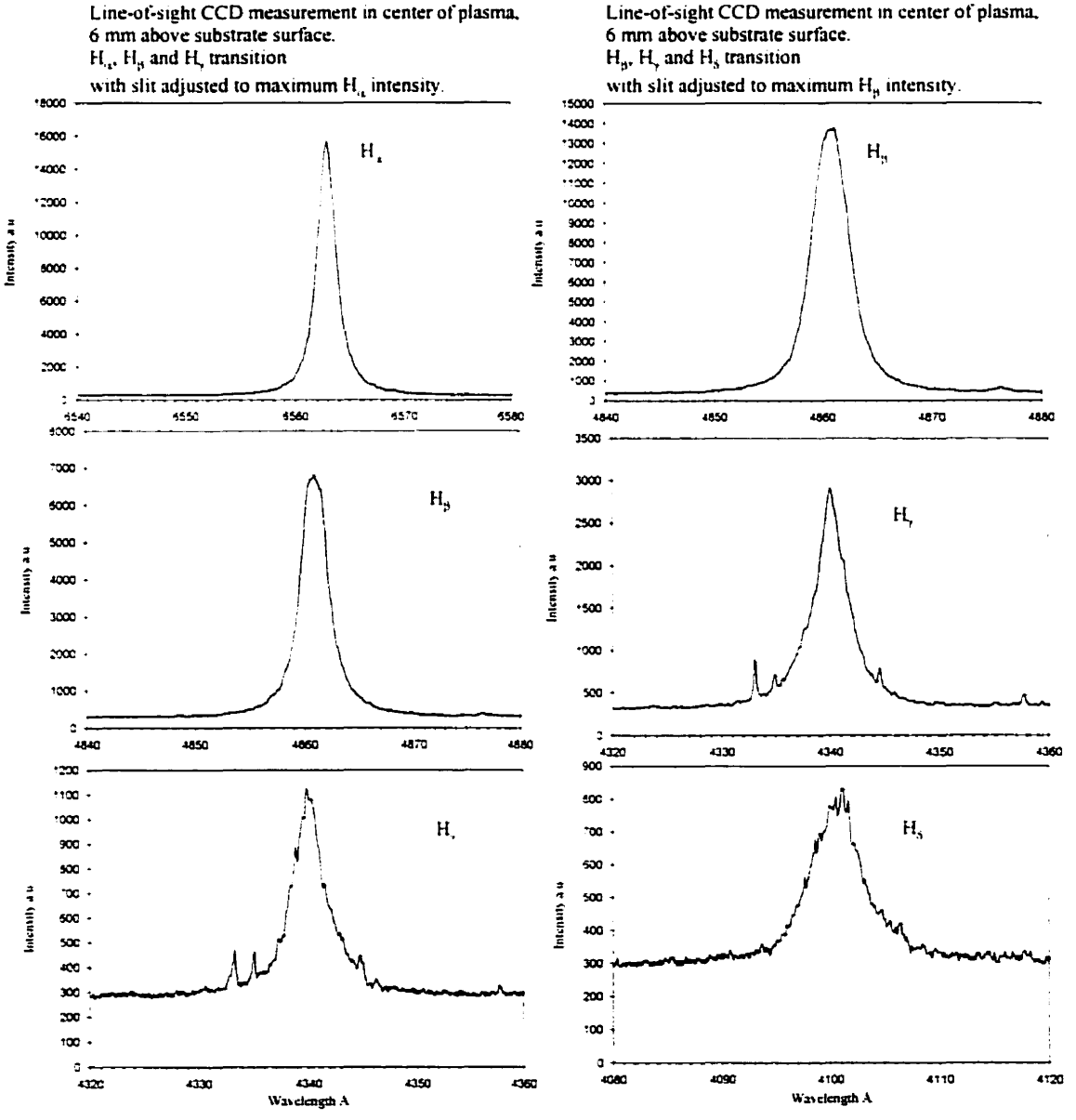

Figure 3.12.3 : Line-of-sight H Balmer emission.

3.12.3 Electron Density Measurement

The atomic hydrogen emission shows Stark broadening of individual lines. Stark broadening is caused by the interaction of the charged particles, electrons and ions, with the discrete energy levels of the atomic transitions. The broadening strongly depends on the electron density in the plasma and is only marginally influenced by the electron temperature. Measurements of the full width at half maximum (FWHM) of the broadened H_β line at 4861 Å obtained from high resolution scans are used to calculate the electron density. The H_β line is selected because it is strongly emitting, free of spectral interference, and because extensive broadening data are available for the complete line profile encompassing a broad range of electron number density values and temperatures. Also, a greater accuracy is generally associated with Stark calculation for the H_β line than for other atomic hydrogen lines (Kalniky, Fassel, Kinseley 1977). Since a high resolution is required, the photomultiplier tube is used to collect the radiation with the following acquisition parameters:

Measurement Range: 4855Å to 4884 Å
Voltage on PMT: 1000 V
Slit Width: 0.015 mm
Resolution: 0.06 Å per point
Integration Time: 1.5 sec. per point

Figure 3.12.4 depicts a measured line profile. The observed line splitting is characteristic for the linear Stark effect (Visser 1976).

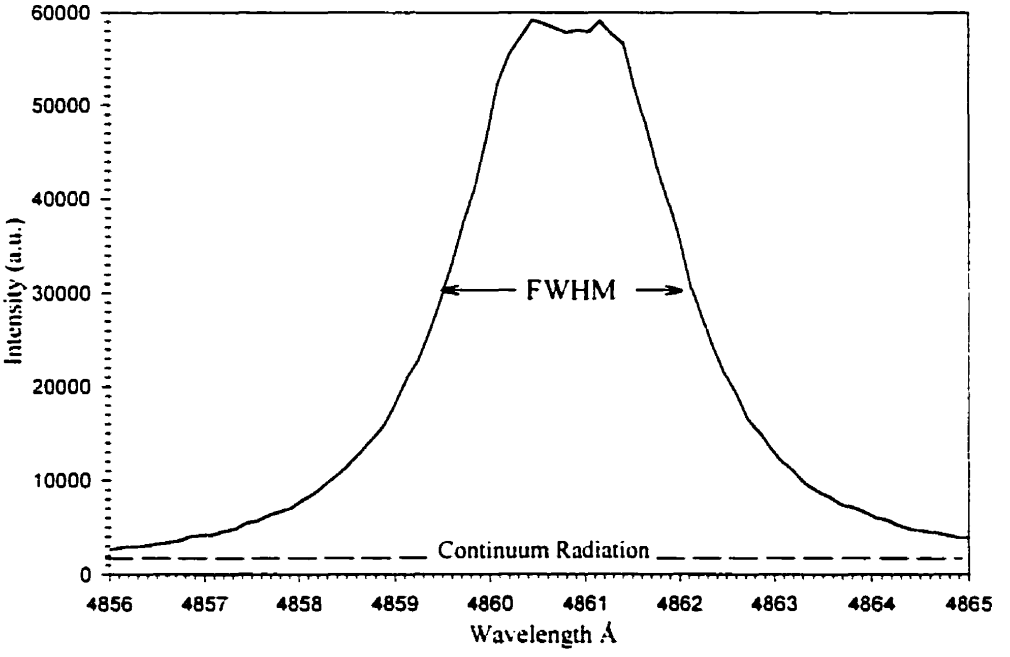

H_β line with PMT: slit width = 0.015 mm. Range: 4856 Å to 4885 Å.
PMT V = 1000 V. Integration time: 1.5 sec/pt. measurement every 0.06 Å
Center of plasma. 6 mm above substrate surface

Figure 3.12.4: Line-of-sight H_β emission

The electron density is calculated according to the unified theory presented by Griem et al. (1968) using the formula proposed by Jian et al. (1992). and verified by Wiese (1978):

$$n_e = \left[C_o + C_1(\ln\ \Delta\lambda) + C_2(\ln\ \Delta\lambda)^2 + C_3(\ln\ \Delta\lambda)^3\right]\Delta\lambda^{3/2} \cdot 10^{13} \qquad (3.12.8)$$

where n_e is the electron density in cm^{-3}, the coefficients C_0=36.84, C_1= -1.430, C_2= -1.33, C_3=0.0089. and $\Delta\lambda$ is the FWHM of the H_β line in Å, after subtracting the continuum emission.

RESULTS

4. Plasma Characterization

4.1 Electron Temperature

The electron temperature profile of the plasma flame is deduced from excitation temperature measurement of the atomic hydrogen Balmer series emission. Horizontal emission measurements of the plasma flame are performed in 0.5 mm intervals, at an axial location 6 mm above the substrate surface. This horizontal position is well above the boundary layer and reflects the free stream plasma characteristics before reaching the region that is influenced by the presence of the substrate. After integration of the peak area and correction for the continuum emission, a spline is fit to the data. Using the function values, the line-of-sight emission is converted to radial radiance using the mathematical Abel conversion. The excitation temperatures are deduced from the relative line intensities, using the Boltzmann plot method. Figure 4.1.1 shows measured intensities and a fitted spline function in the example of the H_β transition.

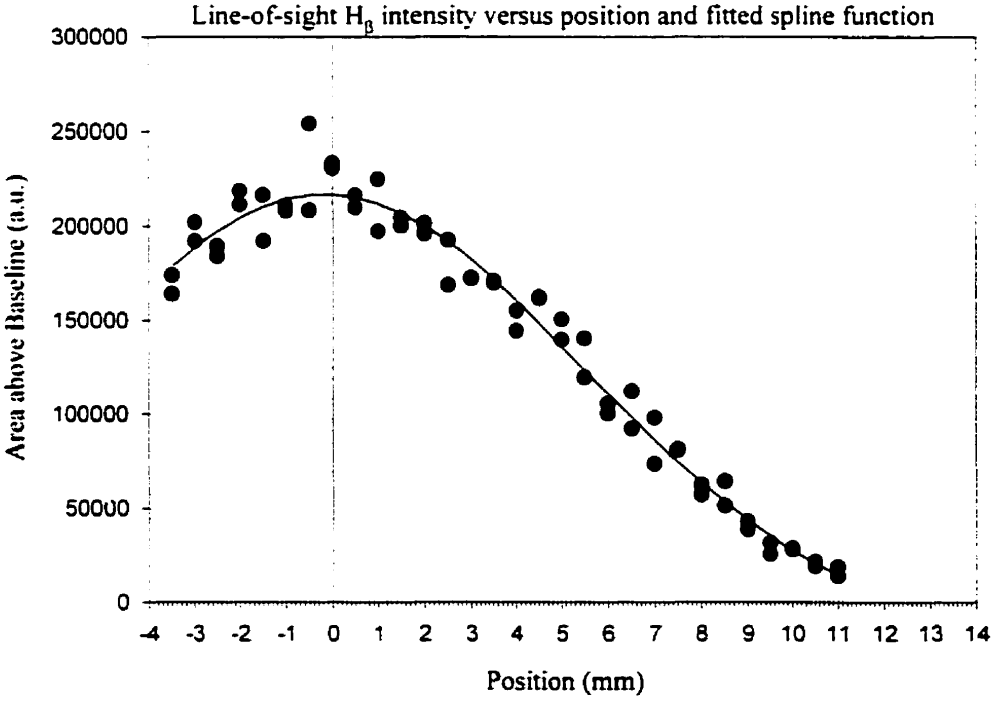

Figure 4.1.1 : Example of line-of-sight H Balmer emission and fitted Spline Function.

Due to the large discrepancy in intensity, only three Balmer transitions are recorded for a given measurement. Figure 4.1.2 shows Boltzmann plots of the inverted radiances at a radial plasma position of 3 mm for the H_α-H_β-H_γ and for the H_β-H_γ-H_δ set.

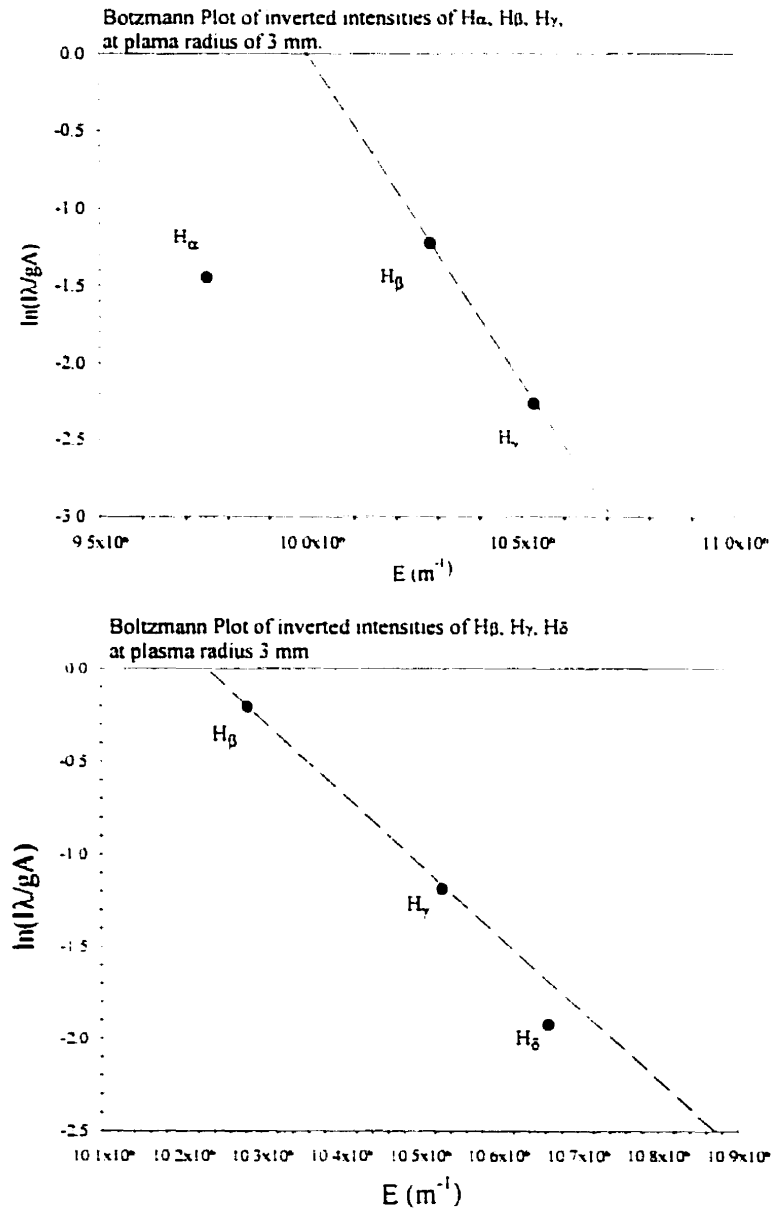

Figure 4.1.2 : Examples of Boltzmann Plots of H Balmer series.

The deviation from linearity of the first three Balmer lines can be attributed to high self-absorption of the H_α emission. With the high emission intensity at this

wavelength the plasma is not optically thin. The H_α line is consequently ignored in the temperature determination. The plot of H_β, H_γ, H_δ is almost linear, indicating that the emission is close to equilibrium. Nonetheless, a slight curvature is seen. This may be caused by interference of three argon I lines at 433.4, 433.5 and 434.5 nm with the H_γ line (Visser, Hamm, Zeeman 1976). Another possibility is that the higher excitation level (H_δ) is underpopulated, as expected in a slowly recombining or even ionizing plasma (Blades 1978). A higher measurement uncertainty is associated with the H_δ line because its intensity is not much larger than the continuum background. The electron temperature is consequently deduced from the H_β to H_γ intensity ratio only, and the resulting radial profile is shown in Figure 4.1.3.

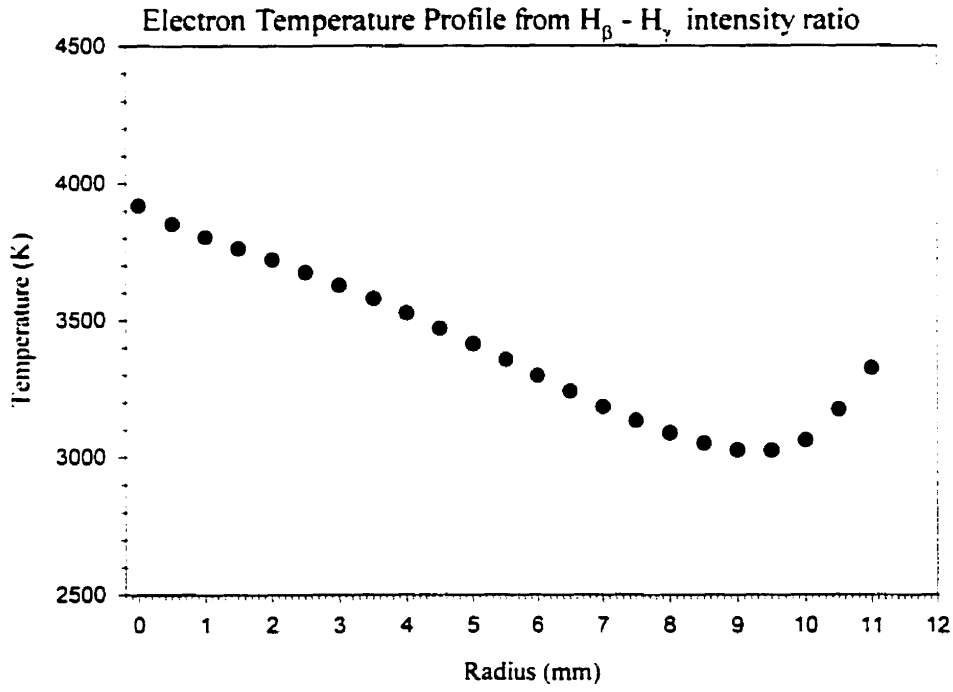

Figure 4.1.3 : Radial Electron Temperature Profile from Hβ, Hγ emission line ratio.

An electron temperature of ~3900 K is measured in the center of the plasma flame at an axial position of 6 mm above the substrate surface. The measured temperature increase in the outer plasma region is an artifact of the measurement method and can be attributed to non-equilibrium effects of the cooling and recombining plasma wing.

4.2 Electron Density

The electron density in the plasma free stream is measured from the linear Stark broadening of the H_β Balmer series member, as described earlier.

Figure 4.2.1 shows the measured electron density profile of the plasma 6 mm above the substrate surface.

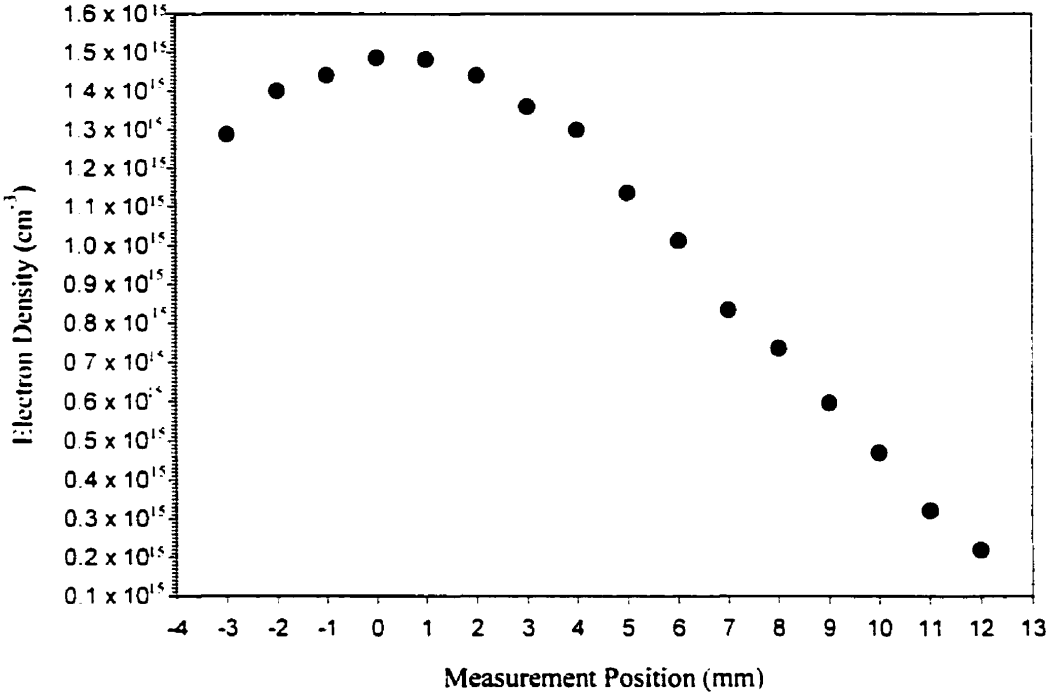

Figure 4.2.1 : Electron Density Profile from Stark broadening of Hβ line, from line-of-sight integrated emission data.
Measurement Position: 6 mm above substrate surface
Slit Width: 0.015mm, PMT Voltage = 1000 V,
Integration Time = 1.5 sec/pt
Measurement resolution: 0.06 Å, Non-inverted spectrum.

An electron density of $1.5 \cdot 10^{15}$ cm^{-3} is found for the center of the plasma flame. Abel's inversion on the emission data is also performed by resolving each line spectrum into 32 intensity data to extract local density values. The inverted profile does not differ significantly form the one in Figure 4.2.1. However, the inverted data indicate a slightly higher electron density in the plasma center of $1.8 \cdot 10^{15}$ cm^{-3}.

4.3 Rotational Gas Temperature

The line-of-sight rotational temperature is measured at eight horizontal positions in the plasma tail flame at an axial position six millimeters above the substrate surface. A horizontal intensity distribution of a representative line emission is shown in Figure 4.3.1.

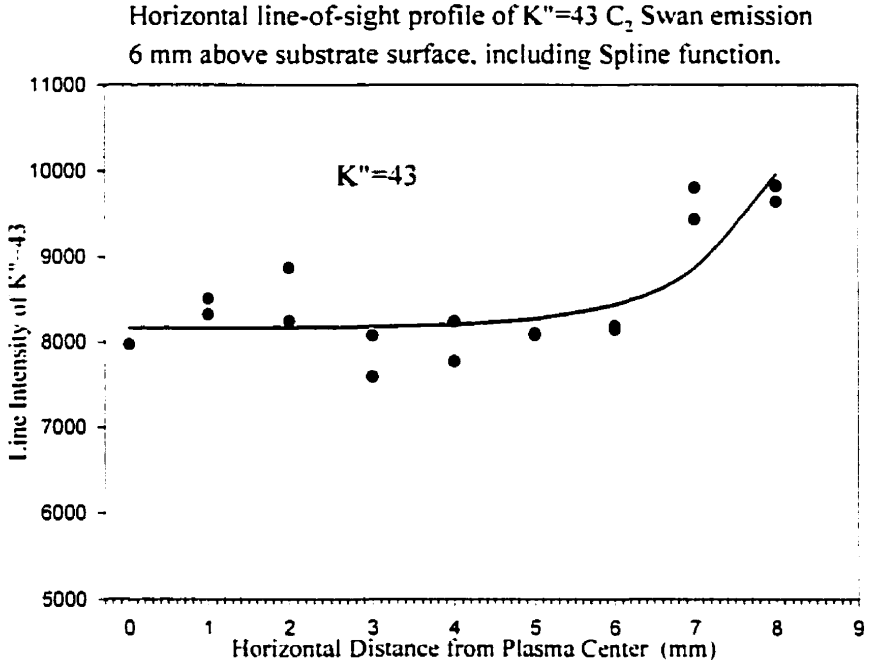

Figure 4.3.1 : Intensity versus y-position for the P-branch K"= 43 C_2 Swan emission.

The emission spectrum is highly sensitive to the plasma fluctuations, causing an appreciable scatter in the acquired data. A possible remedy includes smoothing the spatial data with a spline function and using the function values in the Boltzmann plot. Another possibility is to average all central radiation values from 0 mm to 6 mm, since the radiation varies little within this range with respect to the scatter. In addition, photographs of the plasma flame show a relatively uniform emission within a six millimeter radius, and then a strong increase in blue-green C_2 emission in the plasma wing (see, for instance, Figure 5.1.1). Using the former, information about the spatial extend of the plasma core can be obtained. The off-center intensity peak makes a conversion of line-of-sight emission into radial radiance values by Abel's inversion very difficult and is not attempted here.

Figure 4.3.2 shows the rotational line-of-sight temperature profile deduced from Boltzmann plots of the spline function values of these spectra.

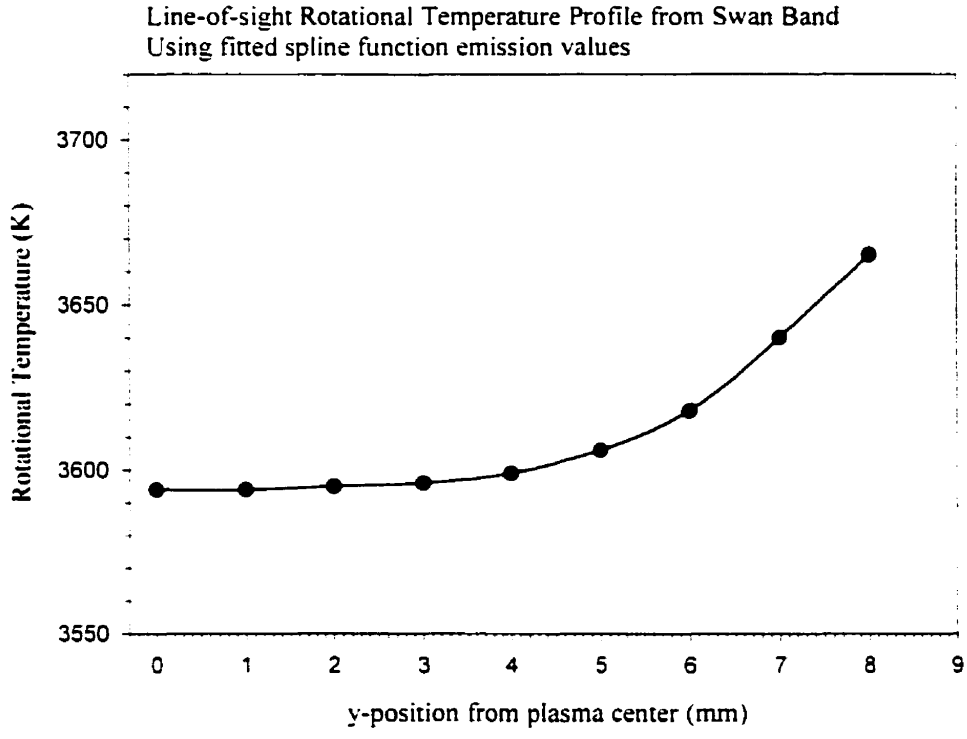

Figure 4.3.2 : Line-of-Sight Rotational Temperature Profile form C_2 Swan Emission.

Within a radius of approximately 6 mm, the temperature is uniform at ~3600 K but then shows an increase in the wing of the plasma flame. This increase can be attributed to a cooling and recombining plasma in the outer flame regions, disturbing the equilibrium distribution of the C_2 emission. Excited state C_2 is generally produced with a non-thermal distribution over its vibronic states and the shape of the emission bands will only reflect the gas phase temperature if C_2 equilibrates by collisions before emission. This effect can cause an indication of a temperature higher than the actual gas temperature (Davis and Martineau 1992). A similar behavior is observed by Adler and Mermet (1973) on a methane/argon plasma. They concluded that the temperatures measured in the center are close to the overall plasma temperature. While the line-of-sight measurements in the wing are contaminated by these non-equilibrium effects, the

central measurements integrate a much smaller volume of the recombining plasma and are dominated by the radiation in the core. It is thereby plausible to accept the measured temperatures in the center as the overall gas temperature of the flame.

Alternatively, averaging the central emission values from y = 0 to 6 mm, yields a gas temperature of 3700 K as depicted in the corresponding Boltzmann plot in Figure 4.3.3:

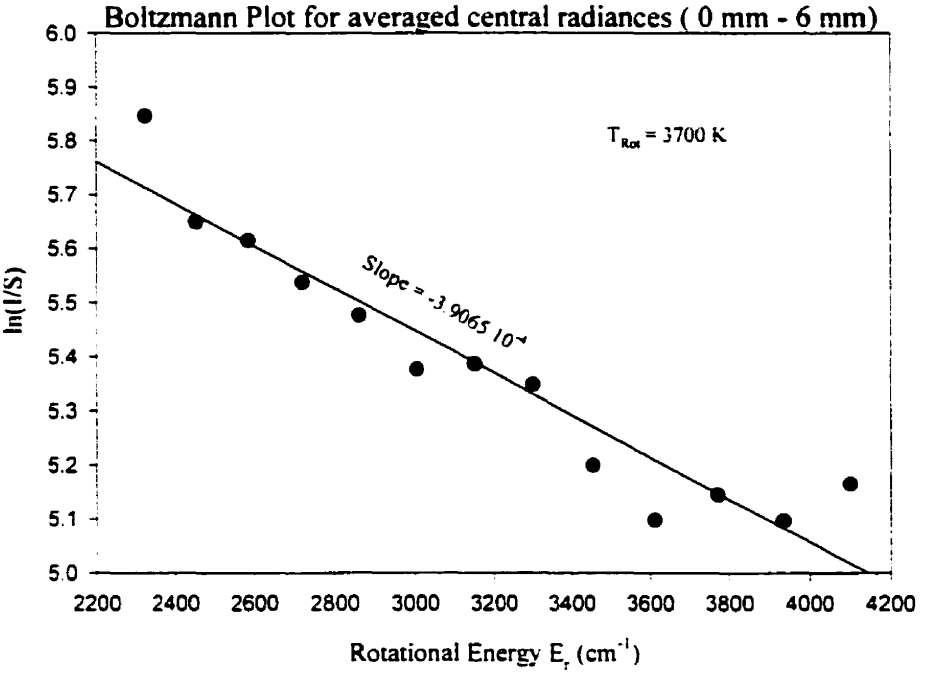

Figure 4.3.3 : Boltzmann Plot for averaged central line-of-sight C_2 Swan Radiance Values.

Both methods that are used to overcome the experimental scatter must be considered approximate. Since the measurement of 3700 K from the averaged intensity values is obtained using less data manipulation, it is here accepted as the average plasma gas temperature.

4.4 Equilibrium State of the Plasma

An equilibrium analysis for our experimental gas composition is performed by using a computer program Facility for the Analysis of Chemical Thermodynamics developed by Thermfact Ltd., Quebec, FACT for short (Figure 4.4.1). For the purpose of illustration the number density of the charged species is shown.

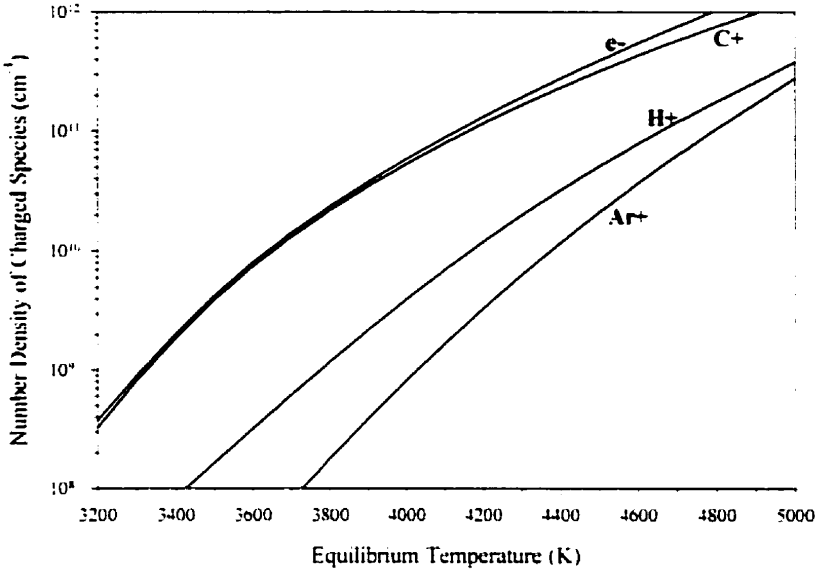

Figure 4.4.1 : FACT Equilibrium Diagram for Experimental Gas Mixture.

2.3926 moles argon, 0.22178 moles hydrogen,
and 0.005529 moles methane at 0.355 atm.

With an ionization potential of 11.26 eV, singly ionized carbon is the predominant ionic species in our plasma. The ionization potentials of hydrogen and argon are 13.6 eV and 15.75 eV, respectively (CRC Handbook, 70th edition 1990). At the measured gas temperature of 3700 K the calculated Saha equilibrium electron density of approximately $1.5 \cdot 10^{10}$ cm^{-3} is substantially lower than the measured value of around $1.5 \cdot 10^{15}$ cm^{-3}. In addition, the electron temperature of approximately 4000 K is elevated above the gas temperature. For $Ar/H_2/CH_4$ thermal plasmas in diamond deposition systems, an elevated electron temperature with respect to the gas temperature is often reported and can be attributed to a finite relaxation time of ionization-recombination processes (Baldwin et al. 1994; and Bousrih et al. 1995).

To indicate the trend expected when non-equilibrium effects are considered, the electron temperature is varied with respect to the heavy species temperatures in a two-temperature partial-equilibrium calculation of a pure carbon plasma in Figure 4.4.2. The compositions are computed according to the NASA method (Boulos et al. 1994), using a code developed by Coulombe et al. (1997). The result of this approximation shows qualitatively that a small increase in electron temperature with respect to the overall gas temperature can, indeed, induce the increase in electron density.

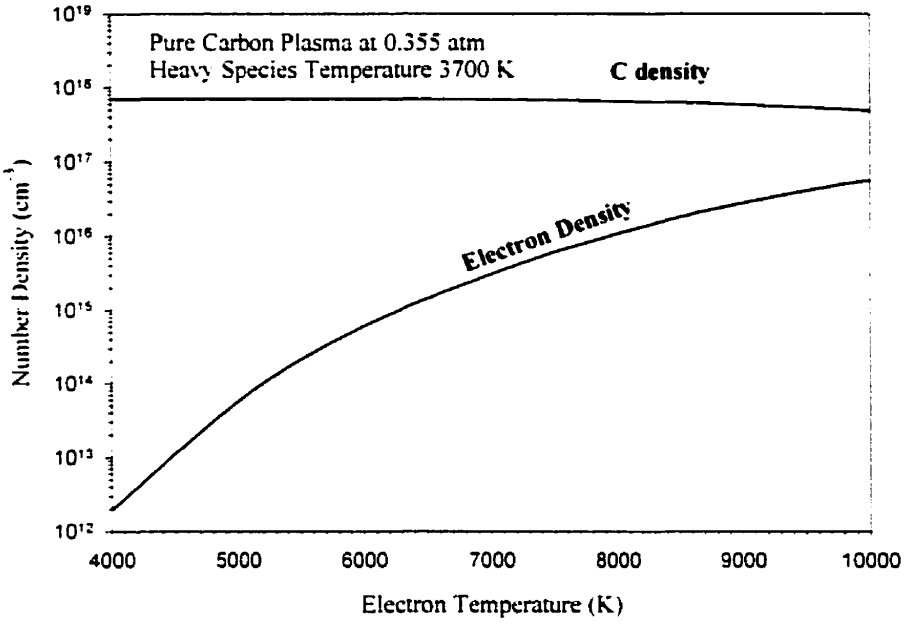

Figure 4.4.2 : Two-Temperature Equilibrium Calculation.
Pure Carbon Plasma at 0.355 atm.

4.5 Average Plasma Gas Velocity

The free stream average velocity of the plasma is estimated from mass and energy balances around the torch by using the colorimetric measurements for the plasma energy. Previous heat balance work with induction systems has shown that the energy leaving the torch can be accurately determined by subtracting all cooling water losses from the dc input to the power unit (Thorpe and Scammon 1969). Power losses to various sections of the reactor system are recorded. The plasma energy is then obtained by subtracting the heat losses in the oscillator tube and load coil from the plate power. Assuming that the process gases leave the system with negligible enthalpy, a second calorimetric measurement is obtained by adding the energy dissipated by the substrate holder, the heat exchanger, and the reactor vessel. Averaging the two independent measurement over a number of experimental runs yields a plasma flame enthalpy of 6.45 kW at a total dc power input of 31.7 kW.

The average gas velocity is approximated as the volumetric gas flow rate divided by the area of the torch exit nozzle. To obtain the flow rate, the average enthalpy, temperature, and density of the plasma gas are interpolated from published data while making the following simplifications: The gas enthalpy is the sensible heat, and radiation is not considered. The plasma gas obeys the ideal gas law, and the specific volume can be corrected for the ambient reactor pressure.

Since thermodynamic and transport properties of the experimental $Ar/H_2/CH_4$ mixture are not readily available, the methane is neglected and the properties are interpolated from published data of a 8.45 % H_2 in an Ar/H_2 mixture only (Boulos, Fauchais, Pfender 1994). The error introduced can be considered negligible, since the methane content is only 0.21 % (Oberste Berghaus 1996). Using these simplifications, the mass and energy balances yield an average plasma temperature of 5120 K, which compares reasonably well with the measured gas temperature. With a nozzle diameter of 19 mm, the average gas velocity at the nozzle exit plane is computed as 65.3 m/sec.

5. Boundary Layer Region

The interface region between the plasma and the substrate plays a fundamental role in the diamond formation. When the hot plasma impinges on the cooled substrate a thin gas phase boundary layer develops near the surface, in which important gas species are both rapidly created and destroyed. Hydrocarbon growth precursors generated in the bulk of the plasma or in the boundary layer must diffuse through the thermal boundary layer without recombining or otherwise reacting if they are to contribute to the diamond growth. Since these reactive species have a finite recombination time as they pass through the temperature gradient, the thickness of the thermal boundary layer determines the degree of supersaturation on the surface. A complete description of this non-equilibrium interface region is a complex matter, and requires a solution of the flow and temperature fields in a three-dimensional geometry, coupled with the gas phase reactions and electrical sheath equations. The objective here is to estimate the thickness of this region, while a complete model is beyond the scope of this work. The boundary layer comprises overlapping regions that include temperature, velocity and species concentration gradients. Since thermal and chemical boundary layers are generally of comparable thickness, the thermal boundary layer is traditionally considered to describe the diamond growth environment (Clements and Smy 1973) (Goodwin and Gavillet 1990 and Goodwin 1991). An electrical sheath region, where electrical neutrality is not preserved and space charge is dominant, must also be considered when the substrate is used as an electrode. However, it is often assumed that the charged particle dynamics has a negligible influence on the flow and temperature field (Cappelli 1993). Consequently, a common approach is to decouple the boundary layer from the sheath and study each region individually.

In this study the thickness of the thermal boundary layer above the substrate is estimated, and possible interactions between space-charge effects and boundary layer conditions, induced by substrate biasing, are explored.

5.1 Thermal Boundary Layer Estimation by Numerical Simulation

A simulation is used to estimate the flow and temperature fields in the vicinity of the substrate surface at the plasma operating conditions. The commercial software CFD 2000 version 3.0, available from Adaptive Research, is utilized. This software is designed to numerically solve conservation equations for mass, momentum, and energy. The code uses a finite-volume representation of the equations, where the domain is decomposed into control volumes. The governing equations are applied to these volumes and numerically integrated over the entire domain.

This work focuses on a vertical axisymmetric flow reactor with the deposition surface perpendicular to the oncoming plasma stream. The diameter of the probe-like substrate is 5 mm, and it protrudes 4 mm from the base of the substrate holder. The substrate and inlet are aligned on the same vertical axis. The substrate surface is 1.5 cm below the torch exit nozzle.

Figure 5.1.1 shows a photograph of the substrate immersed in the oncoming plasma jet, as used in the present study. The gradients in emission intensity above the substrate surface can be visually identified and reflect the thermal and chemical boundary layers.

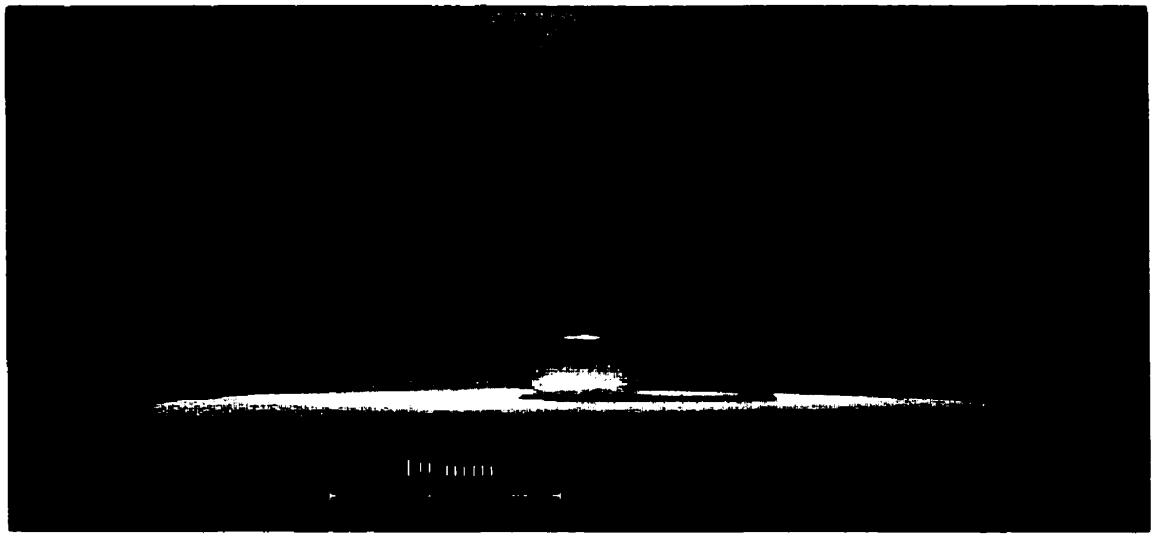

Figure 5.1.1: Photograph of Substrate immersed in Plasma Jet.

To approximate the boundary layer dimensions, a number of simplifying assumptions are made. Since the film growth rates are substantially lower that gas velocities in a CVD system, the problem is described by steady state. Dilute reactants are assumed. The carbon from the methane participates in nearly all gas phase reactions but its concentration is very small. The assumption of dilute reactants leads to a significant reduction of the scale of the numerical problem by removing the dependence of the flow and temperature on the species balance and its reaction terms. The transport and thermodynamic properties are evaluated for 8.45 % hydrogen in argon gas mixture. The small amount of carbon present is not expected to affect the gas properties. The thermal conductivity, density, specific heat and viscosity are interpolated from published experimental data (Boulos et al. 1994). Transport properties are a function of temperature and can be evaluated from statistical mechanics or from experimental data. However, these evaluations are valid only if thermodynamic equilibrium can be assumed. Since the conditions in the boundary layer region are expected to deviate strongly from equilibrium, the species concentration and their properties are modeled to be "frozen" at their free stream value. Table 5.1.1 summarizes the values of the gas properties used.

Gas Property	*Value*
Gas Temperature at Inlet	4000 K
Inlet Gas Velocity	65.3 m / sec
Pressure	0.3553 atm
Mole Fraction of H_2 in Ar/H_2	8.45 %
Density	0.1042 kg / m^3
Viscosity	$1.465 \cdot 10^{-4}$ kg / m sec
Specific Heat	1010.5 J / kg K
Thermal Conductivity	0.5573 W / m K

Table 5.1.1 : Gas Properties used in Numerical Simulation with CFD 2000.

5.1.1 Computational Domain and Boundary Conditions

A two-dimensional cylindrical coordinate system is chosen, since the geometry of the problem is axisymetric, and an azimuthally velocity component does not arise. To reduce computational time, a 3° angle of the cylindrical arrangement is evaluated only. Figure 5.1.2 shows a schematic of the computational domain, including the mesh of the discrete finite-volume elements.

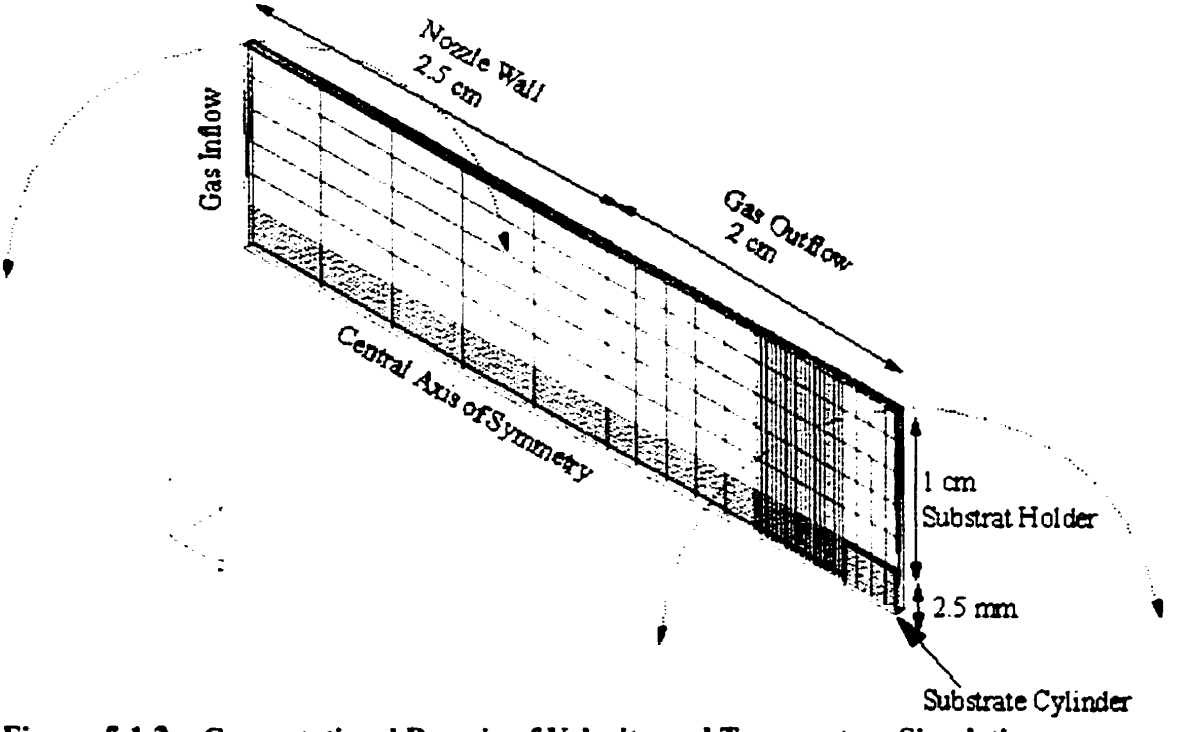

Figure 5.1.2 : Computational Domain of Velocity and Temperature Simulation in CFD 2000.

The following boundary conditions are specified:

The heat and mass flux on the nozzle wall and substrate holder are zero (thermal insulation), and there are no radial and axial velocity components on the walls (No-slip). No radial fluxes or radial gradients are present on the axis of symmetry. A constant axial velocity component of 65.3 m/sec is specified at the gas inflow. The velocity at the gas outflow is computed at the reactor pressure. The temperature of the substrate surface is fixed at 1000°C, and the no-slip boundary conditions apply.

5.1.2 Velocity and Temperature Profiles

The gas velocity components as a function of distance to the substrate surface are shown in Figure 5.1.3. The radial position of 0.4 mm off-axis is chosen for this illustration, since a radial velocity component can be shown.

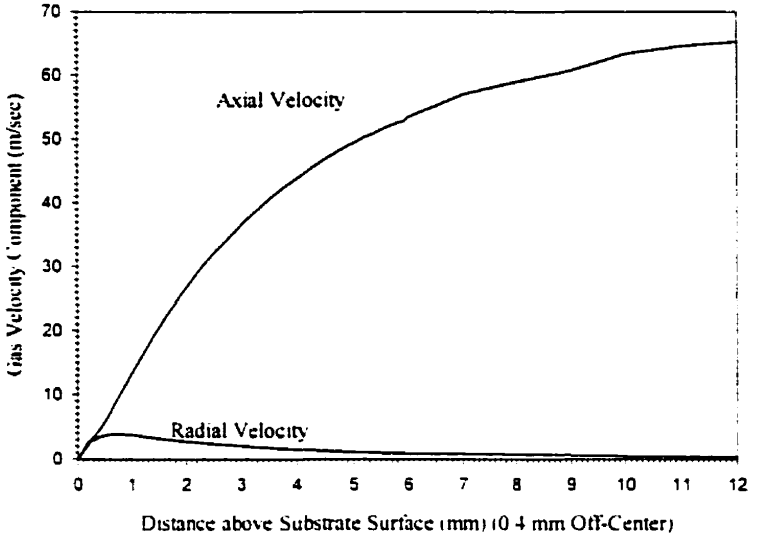

Figure 5.1.3 : Velocity Components above Substrate Surface.

Figure 5.1.4 gives a one-dimensional cut along the stagnation line of the gas temperature as a function of distance to the substrate surface. The thermal boundary layer thickness is the distance between the substrate and the location where the temperature reaches 95 % of the free stream value. A thickness of approximately 1.6 mm is obtained.

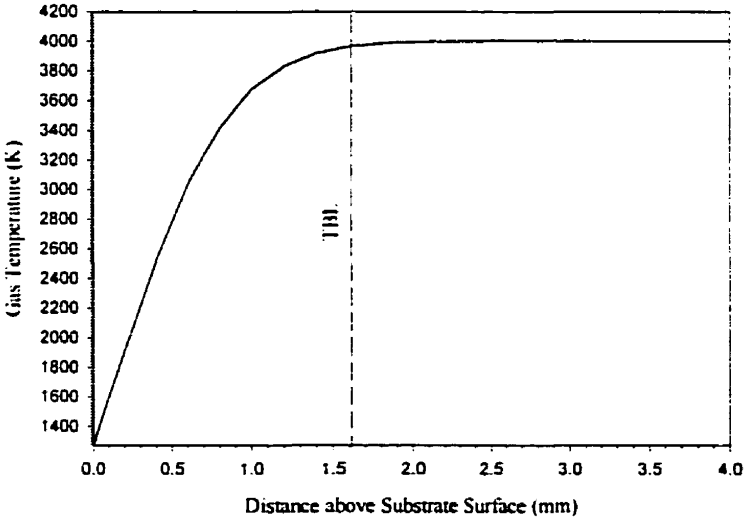

Figure 5.1.4 : Simulated Thermal Boundary Layer Thickness.

5.2 Spectroscopic Measurements in Boundary Layer Region

Optical emission spectroscopy (OES) measurements are made on the line-of-sight emission intensities of the hydrogen Balmer lines in the gas phase above the substrate surface. Line-of-sight measurements above a large and flat substrate are limited in spatial resolution, and the optical cone of observation is truncated in close proximity to the surface. The probe type geometry of the substrate used in this study allows measurements very close to the surface and is forcing the plasma parameters to change only at one confined and small area location in the flame such that variations in radiation observed above the substrate are local changes in emissivity originating from the boundary layer. Radial variations in the plasma free stream can largely be disregarded because uniform plasma conditions above the small probe are likely. Although the surrounding plasma, in which the probe and its boundary layer are immersed, contributes to the line-of-sight radiation, its intensity remains essentially constant for measurements closer to the substrate surface. Consequently, variations in radiation in the boundary layer can be isolated even though the surrounding plasma may distort the absolute emission values.

5.2.1 Electron Density

The evolution of the electron density (n_e) in the boundary layer is evaluated from the Stark broadening effect on the H_β line at 4861 Å, as described earlier. Line-of-sight measurements are taken along the vertical axis above the substrate in 0.2 mm spatial increments. To reduce the total acquisition time, the spectra are recorded with the CCD diode-array camera with an exposure time of 10 milliseconds rather than using the high-resolution photomultiplier system. At standard plasma operation, boundary layer measurements are performed with an electrically floating substrate and under strong positive (+500 V) and strong negative (-400 V) substrate bias conditions in the same experimental run. Figure 5.2.1 shows the measured electron density as a function of position above the substrate surface in the two extreme bias cases. Since no bias induced difference in the line width can be discerned within the experimental fluctuations,

averaging and smoothing all three measurements including the floating substrate case yields the continuous curve.

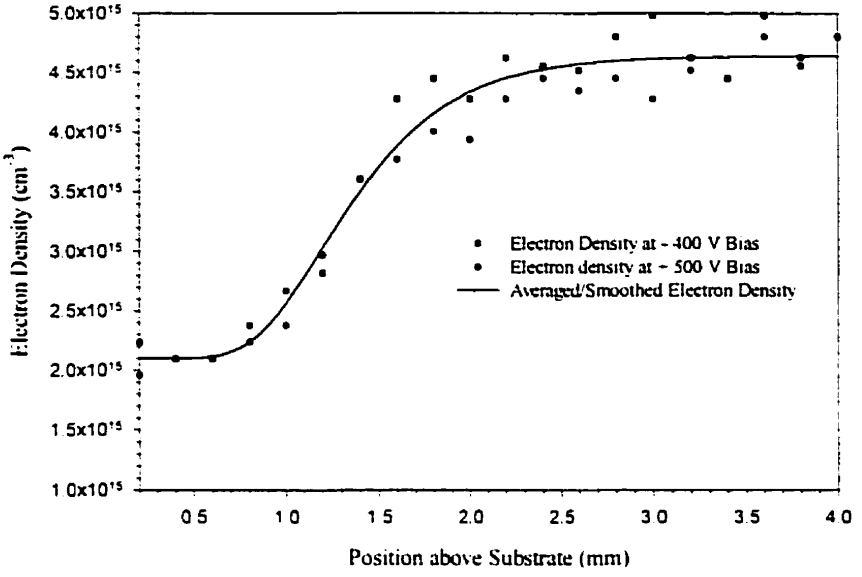

Figure 5.2.1 : Electron Density in Boundary Layer from Line-of-Sight H_β Broadening at (– 400 V) and (+500 V) Substrate Bias Voltage.

The electron density starts decreasing from its free stream value at approximately 2 mm above the substrate. At positions less than 0.7 mm, the emission intensity from the boundary layer is possibly quite low. The surrounding plasma gas dominates the radiation collected in close proximity to the substrate, and the observed asymptotic trend is an artifact. The free stream density of $4.5 \cdot 10^{15}$ cm^{-3} is slightly higher than previously measured. This may be due to the limited resolution of CCD system, which exaggerates the width of the emission line. It is also possible that the plasma has drifted from the conditions at which the original electron density measurements are obtained. A slow drift in plasma conditions is experienced throughout the experimental work and is further discussed in section 8.1.

The electron density gradient is expected to follow the temperature gradient. The electrical boundary layer thickness of ~ 2 mm is in some agreement with the simulated thermal boundary layer thickness of ~ 1.6 mm. The application of a substrate bias voltage, positive or negative, does not affect the electron density above the substrate surface in the resolved spatial range.

5.2.2 Electron Temperature

Along with the measurement of the H_β line intensity at 4861 Å, the H_γ line at 4340 Å was recorded as a function of axial position above the surface for the three bias conditions. The acquisition parameters are described above and are kept identical. Two consecutive frames are taken with the CCD camera per measurement. Due to the broadening of the lines, the intensities are found by integrating the area under the emission peak with the background emission subtracted. The excitation temperature evolution of atomic hydrogen in the boundary layer is evaluated from the relative intensity of the two Balmer series lines, using the Botzmann plot method. Figure 5.2.2 depicts the H_γ intensities as a function of position for the electrically floating substrate and at –400 V and + 500 V bias voltage.

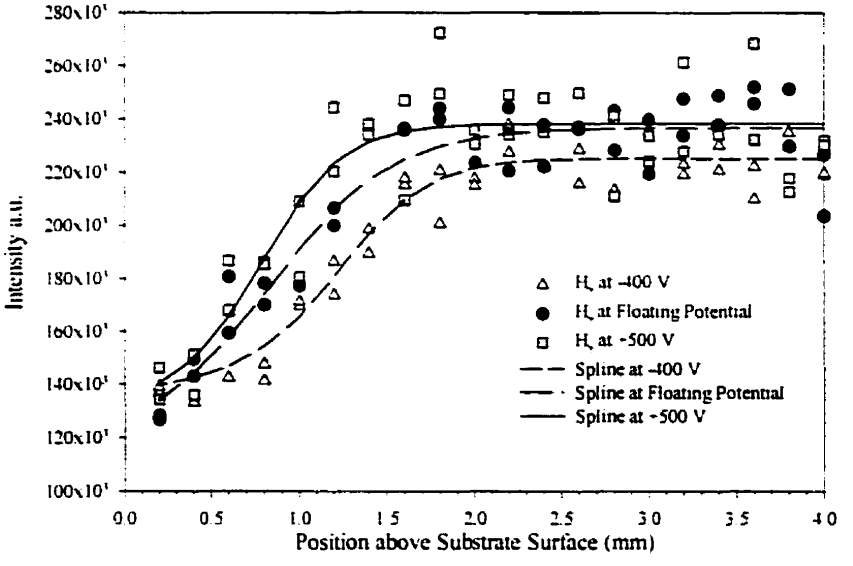

Figure 5.2.2 : H_γ Intensity in Boundary Layer for different Substrate Bias Conditions.

Since the intensity data of both H_γ and H_β exhibit an appreciable scatter, spline function values are used for the temperature determination. The intensity ratio of the two atomic transitions yields the excitation temperature profiles for the three bias cases shown in Figure 5.2.3.

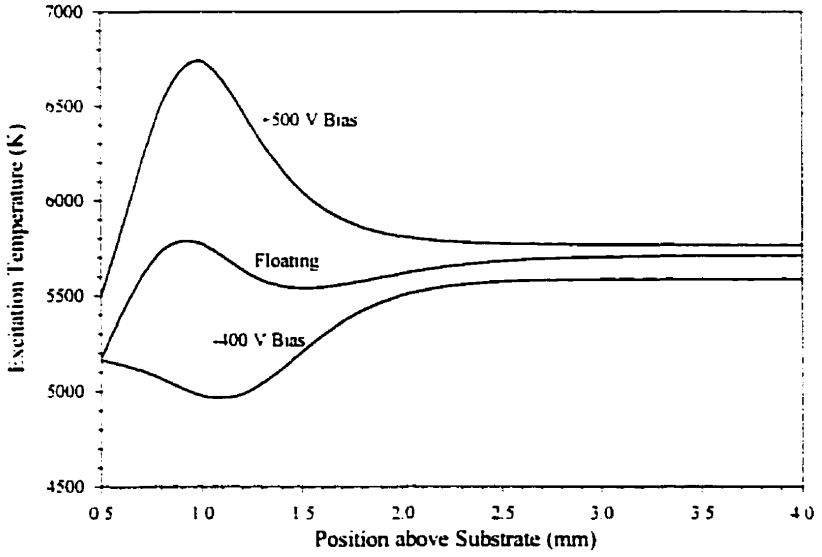

Figure 5.2.3 : Atomic hydrogen excitation temperature in boundary layer at different bias conditions.

The excitation temperature increases in the boundary layer region with increasing positive bias from –400 V to +500 V, as reflected by an increase in excited state population (n = 5) of atomic hydrogen. Again, the surrounding plasma gas probably corrupts the line-of-sight emission data in close proximity to the surface. This causes the measured peaks at the 1 mm position. The free stream temperatures are not in exact agreement with previous plasma characterization, which is again due to the plasma drift and will be further discussed in section 8.1. The slight variations in plasma free stream temperature in the three curves are due to the experimental scatter. The excitation temperature may or may not represent the electron temperature because of uncertainties about the equilibrium state in the boundary layer. Figure 5.2.3 illustrates that an increase in atomic hydrogen excitation and possibly electron temperature in the boundary layer is induced by the application of a positive substrate bias.

6. Effect of Bias Voltage on Diamond Deposition

6.1 Preliminary Observations

The effect of substrate bias voltage on the diamond deposit is investigated. The plasma is operated at argon, hydrogen and methane gas flow rates of 57.56 slpm, 5.31 slpm and 0.133 slpm, respectively. The substrate is located 1.5 cm below the torch exit nozzle. The initial substrate temperature is maintained at 900°C ± 50°C, as measured by the pyrometer probe at a location of 5 mm below the surface. The corresponding surface temperature can be extrapolated using the heat flux of about 45.5 W and a thermal conductivity of molybdenum of 105 W/m·K and is approximately 1060°C ± 50°C. The substrate temperatures given in the following sections refer to the measured values only and not to the actual deposition surface temperatures. In these preliminary runs a plate power of 28 kW is applied, which is slightly lower than the power used in subsequent experiments.

All operating parameters except the bias voltage are kept nominally constant. A bias voltage in the range of −100V to +500 V is applied at the moment the methane gas is injected, and the deposition commences. A constant bias voltage is supplied throughout the duration of the run, including the initial nucleation stage. The morphologies of the diamond deposits obtained in 40 minutes are depicted in the SEM micrographs in Figure 6.1.1 at 1500 time magnification.

The deposits consist of particles with diameters ranging from 15 μm to 25 μm. At positive bias voltages (+200 V to +500 V) the particles are spaced far apart, and the particle number density appears low. At moderate bias (-100 V, 0 V, +100 V) a higher number density is observed such that the particles are starting to coalesce to form a continuous coverage.

The particles are composed of mostly triangular crystal faces. A crystal size variation with bias voltage is clearly illustrated in the micrographs. At positive bias the crystals are approximately 4 to 6 μm in diameter, while at the negative bias a much smaller crystal size (~0.5 – 1.0 μm) is obtained. A small crystal size generally reflects

degradation in diamond quality and comes about when nucleating a new crystal is preferred over building up an existing one. In the limiting case of small crystals cauliflower-type diamond deposits are composed of microcrystals only.

The results suggest that at negative bias voltage the nucleation rate is promoted but the diamond quality is degraded. On the other hand, positive bias voltages suppress nucleation but assist in the formation of larger diamond crystal faces. Subsequently, the effect of bias voltage on the nucleation and the growth are investigated separately.

6.2 Initial Nucleation Density

The growth of a diamond film is initiated by the formation of diamond nuclei on the substrate surface. The creation of these nuclei occurs only within a finite time period in the beginning of the deposition process. Subsequent deposition does not generate new sites but rather increases the size of the existing particles leading to eventual coalescence. (See section 7.3)

The effect of applied substrate bias voltage on the initial diamond nucleation is investigated. A deposition time of five minutes at constant bias voltage conditions is used.

The nucleation density is evaluated from particle counts of SEM micrographs taken in the center of the substrate, 90 times or 370 times magnified. All particles with a diameter larger than one micrometer are considered. A typical micrograph in Figure 6.2.1 shows a uniform distribution of the nuclei across the substrate. Such uniformity is, however, not always attained.

Nucleation densities at voltages from –300 V to +500 V are shown in Figure 6.2.2. The measured substrate temperature is between 800°C and 910°C. From –100 V to +500 V the nucleation density is invariant at approximately 3000 particles/mm^2, within the experimental reproducibility. At negative bias below –200 V the density increases up to 15,000 mm^{-2}. The variability is pronounced in the negative bias range.

Figure 6.2.1 : Typical Initial Diamond Nucleation (90 Mag.).

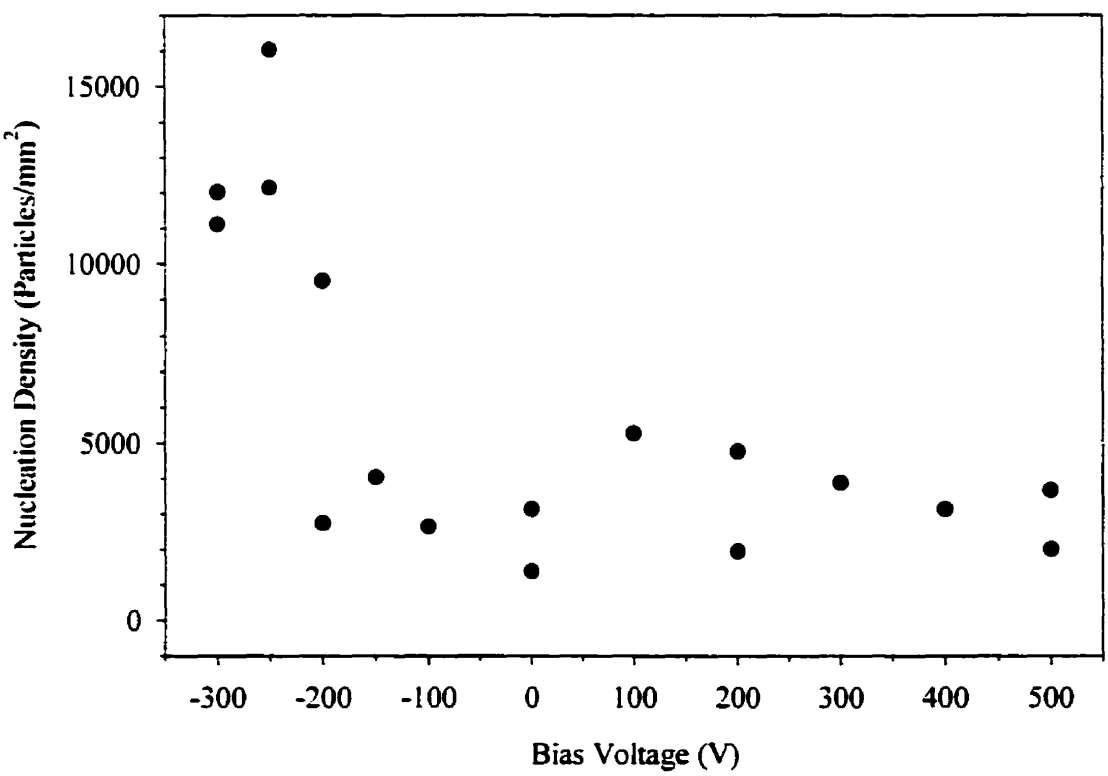

Figure 6.2.2 : Initial Nucleation Density versus Substrate Bias Voltage.

During the course of these experiments, a rather poor reproducibility in initial nucleation density is encountered. In addition, highly non-uniform coverage of the surface, prohibiting density measurements, is occasionally obtained. This is possibly due to the high sensitivity of the nucleation process on the substrate surface pretreatment as well as on the plasma operating conditions. The mechanism of nuclei formation is strongly coupled to the presence of preexisting nuclei or nucleation sites (Kulish, Ackermann, Sobisch 1996). Often, the patterns of coverage suggest that nucleation is strongly influenced by the presence of earlier formed diamond nuclei. Figure 6.2.3 shows a close-up (500 times magnification) of such a site in the case of a non-uniform deposit.

Figure 6.2.3 : Region of Non-Uniform Diamond Nucleation (500 Mag.).

In spite of these problems, an increase in nucleation density at strong negative bias voltage is here observed.

6.3 Quality of Initial Diamond Nuclei

The diamond morphology of the initial nuclei formed after five minutes deposition varies significantly as a function of bias voltage, even though all the nuclei are of comparable size. The morphology ranges from cauliflower-like particles consisting of microcrystals only to well defined cubo-octrahedral diamond particles. The SEM micrographs in Figure 6.3.1 obtained at a magnification of 5000 exemplify representative morphologies generated at strong negative (-200 V) and strong positive (+300 V) bias.

In an attempt to quantify the morphology, a ratio is defined which relates the size of the largest crystal face on a particle to the diameter of that particle. A low ratio represents cauliflower morphologies, and a high ratio characterizes well-defined diamond crystals. This ratio as a function of bias voltage is shown in Figure 6.3.2. Positive bias conditions ensure the formation of distinct crystal faces. Moderate negative voltages cause a decrease in crystal size until cauliflower-type diamond is formed at a strong negative bias below –200 V. From Figure 6.3.2 it can be concluded that the augmentation in nucleation density in the negative range, as seen in the previous section, compromises the nuclei quality.

Figure 6.3.1 : Typical Nuclei Morphologies (5000 Mag.)
at (a) –200 V: Cauliflower. (b) +300 V: cubo-octrahedral (100) and (111) crystal faces.

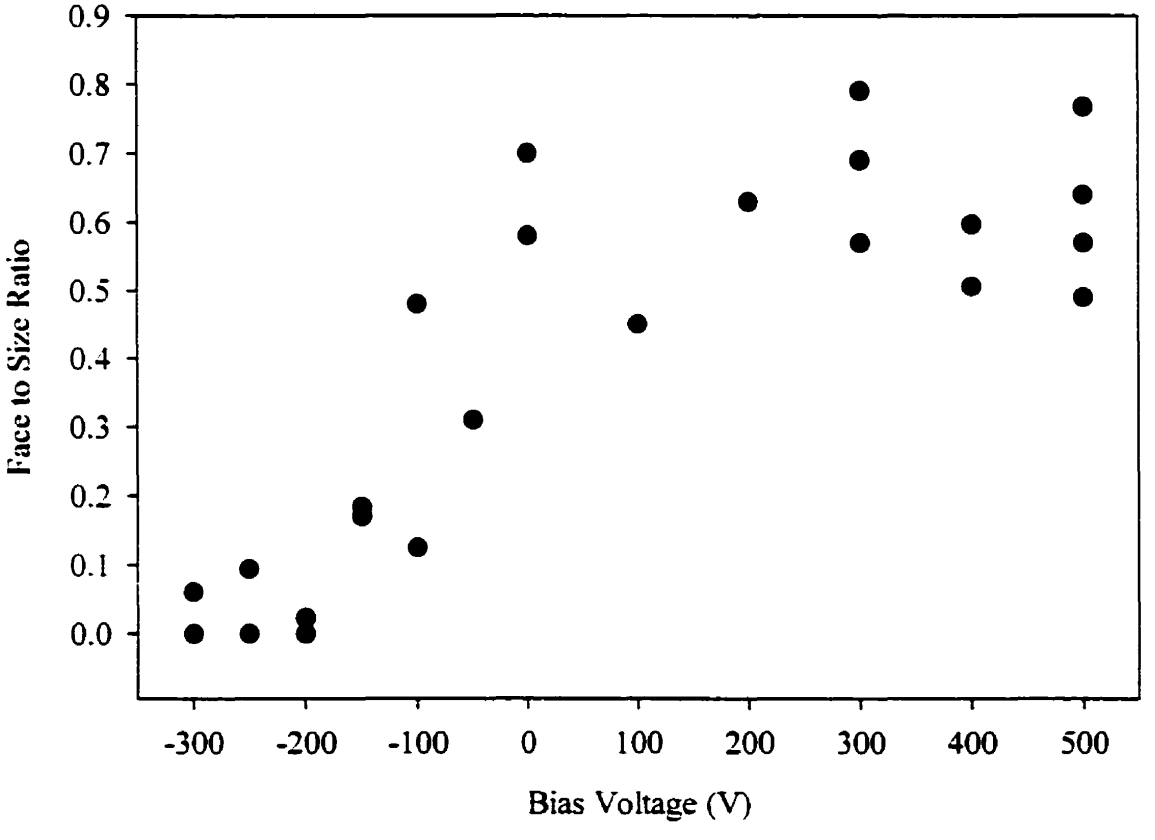

Figure 6.3.2 : Nuclei Crystal-Particle Size Ratio Versus Bias Voltage.

6.4 Diamond Film Quality

The diamond quality is assessed on deposits of homogeneous surface coverage, obtained by treating the nucleation and growth stages separately. The plate power is adjusted to 32.7 kW. The deposition is initiated at a bias voltage of –250 V for the first five minutes to promote a high nucleation density. The bias voltage during growth is then applied in the range of –300 V to +500 V for 40 minutes before the experiment is terminated. The SEM micrograph at 200 times magnification in Figure 6.4.1 exemplifies the homogeneous surface coverage in the case of +400 V bias voltage.

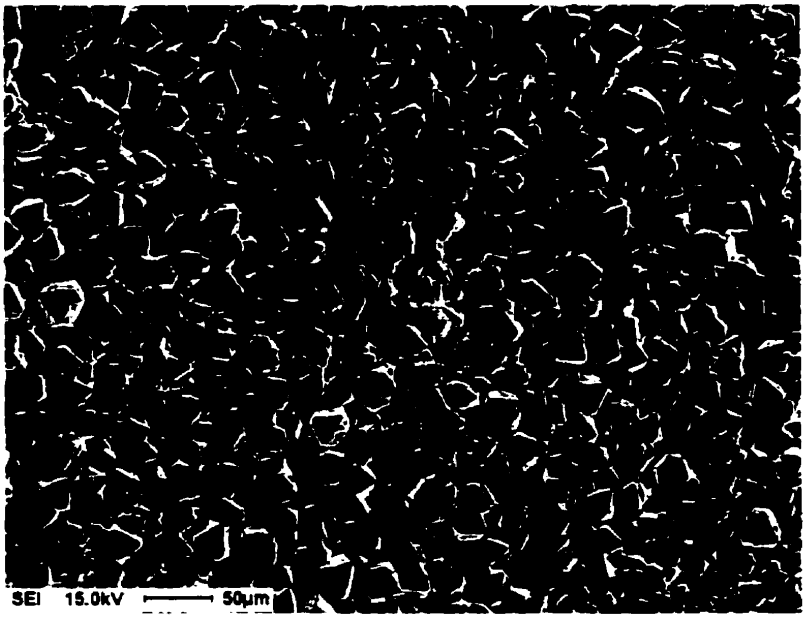

Figure 6.4.1 : SEM Micrograph (200 X) of Film Deposit.
Nucleation at –250 V (5 min.), Growth at +400 V (40 min).

The SEM micrographs (650 X mag.) in Figure 6.4.2 demonstrate a distinct increase in crystal size with an increase in positive bias voltage. At a negative bias, only microcrystal morphologies are obtained. Very high positive bias voltages, +400 V and +500 V, produce triangular and rectangular crystal faces with a diameter of up to 20 µm.

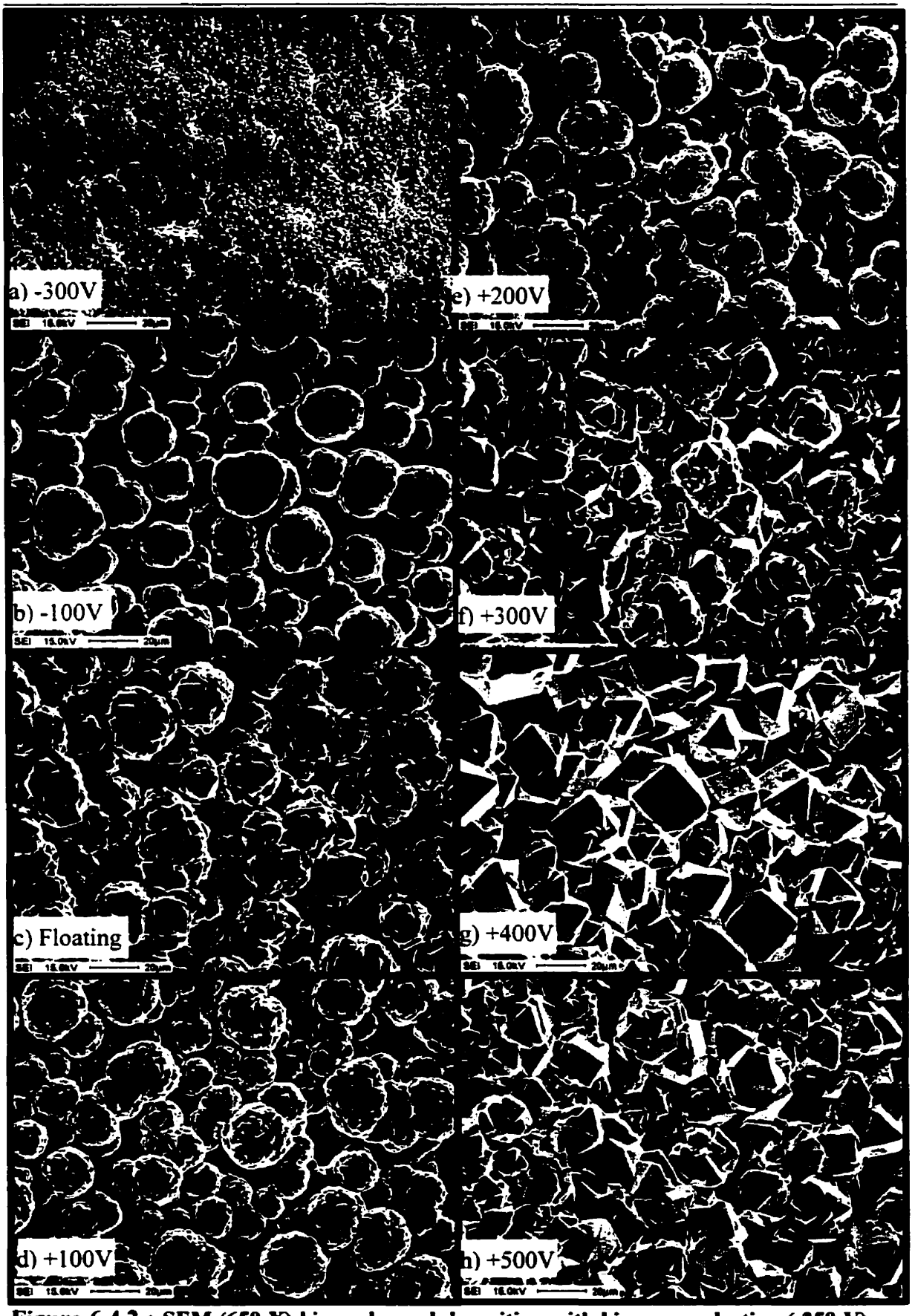

Figure 6.4.2 : SEM (650 X) bias enhanced deposition with bias prenucleation (-250 V).

Micro Raman spectroscopy is performed to confirm the trend in diamond quality. The diamond phase of sp^3 bonded carbon appears in the Raman spectra at 1332 cm^{-1}. This Raman line positively identifies diamond, and the strength of this signal is a measure of the diamond quality (Bahr et al. 1996). Broad bands located around 1350 and 1580 cm^{-1} correspond to amorphous features with sp^2-bonded carbon content (Huong 1991). Bridged carbon or sp^3-hybridized carbon atoms exhibit a signal around 1470 to 1500 cm^{-1} (Bárdos et al. 1994). The sensitivity of the Raman signal to sp^2 features is about 50 times higher than its sensitivity to sp^3 structures (Stoner, Ma, Wolter, Glass 1992). Consequently, the presence of the 1332 cm^{-1} peak reflects a high diamond content.

Figure 6.4.3 shows the Raman spectra evolution as a function of bias voltage during the growth stage. The spatial resolution of the Raman apparatus is approximately 2 μm. The spectrum varies with measurement position. Amongst a number of spectra, the highest diamond signal obtained, if any, is used. The spectra correspond to the samples in Figure 6.4.2. As the bias voltage is made more positive, the diamond signal at 1332 cm^{-1} increases with respect to the amorphous carbon features. The comparison suggests that, indeed, the diamond quality is improved by applying a positive bias voltage and the quality is diminished at negative substrate bias.

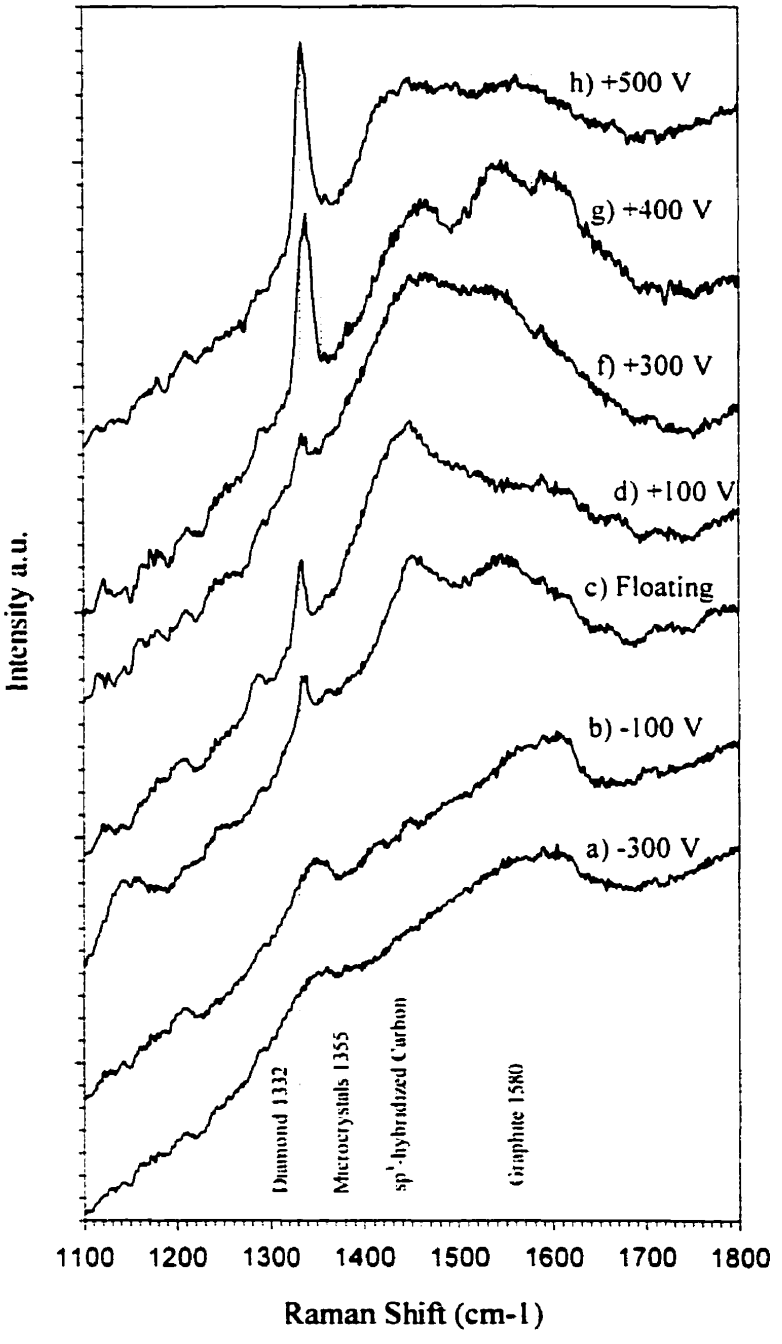

Figure 6.4.3 : Normalized Raman Spectra for Bias Induced Quality Evolution.
(signal assignment to carbon structure is indicated)

6.5 Diamond Film Growth Rate

Starting from the initial nuclei, the diamond particles grow laterally and in the direction of the free surface during subsequent deposition. A continuous film is created when the lateral growth forces the particles to coalesce. If the film is thin, lateral stresses can cause the deposit to delaminate from the substrate during cooling. These stresses arise from the mismatch in thermal expansion coefficient between diamond and molybdenum. The deposit generally adheres to the surface without breakage if either the film is not completely continuous or if its thickness provides sufficient structural integrity. A non-continuous and/or columnar structure allows for some lateral relaxation, and internal stresses in the film are possibly quite low. For deposition times longer than 40 minutes, thick and well adhering films are produced. The SEM micrograph in Figure 6.5.1 shows a side-view of a thin delaminated film. The lower part of the photo shows the bottom-side of the film, formerly attached to the substrate surface. The individual particles of which the film is composed can be identified.

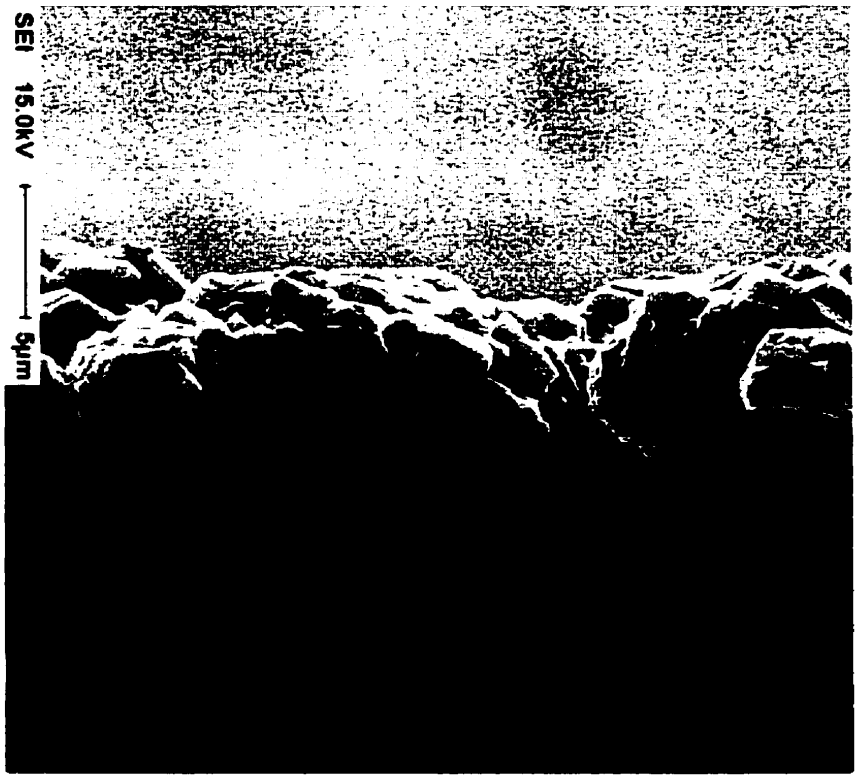

Figure 6.5.1 : SEM micrograph of delaminated diamond film (3000X).

The photograph in Figure 6.5.2 shows the molybdenum substrate after extended deposition. The continuity and uniformity of the non-delaminated film are clearly illustrated.

Figure 6.5.2 : Photograph of diamond film deposited molybdenum substrate.

The film thickness is estimated from cross-sectional SEM micrographs of the film at a view angle parallel to the substrate surface. Figure 6.5.3 shows such micrographs for deposits obtained at floating conditions and at +200 V, +300 and +500 V bias voltage conditions.

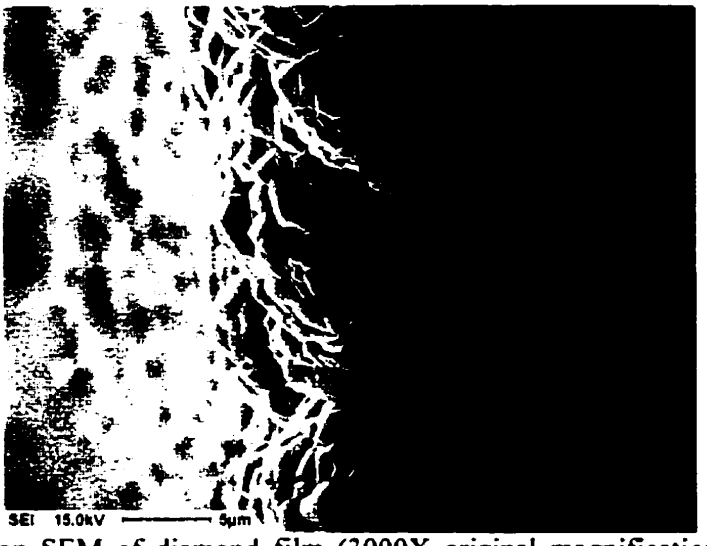

(a) Cross-section SEM of diamond film (3000X original magnification); Initial substrate temperature 960°C, Deposition Time: 40 min., No applied bias voltage (floating), estimated average film thickness: 12 μm.

(b) Cross-section SEM of diamond film (1500X original magnification); Initial substrate temperature 900°C, Deposition Time: 60 min., +200V Bias Voltage, estimated average film thickness: 22.6 μm.

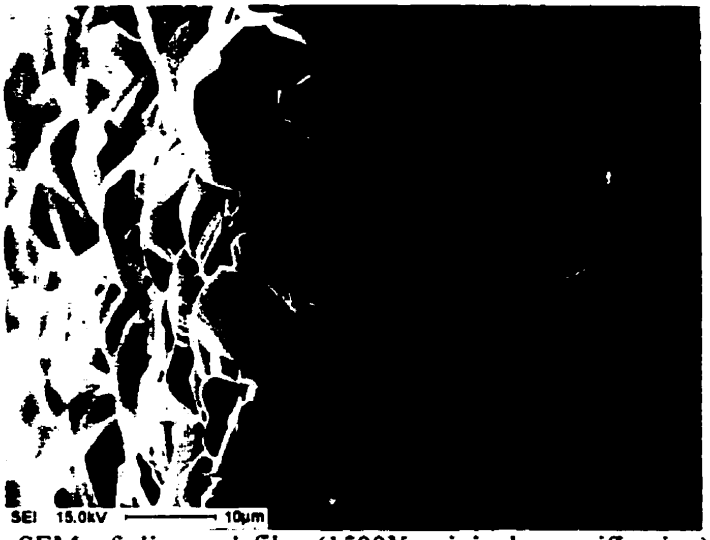

(c) Cross-section SEM of diamond film (1500X original magnification); Initial substrate temperature 890°C, Deposition Time: 60 min., +300V Bias Voltage, estimated average film thickness: 34.6 μm.

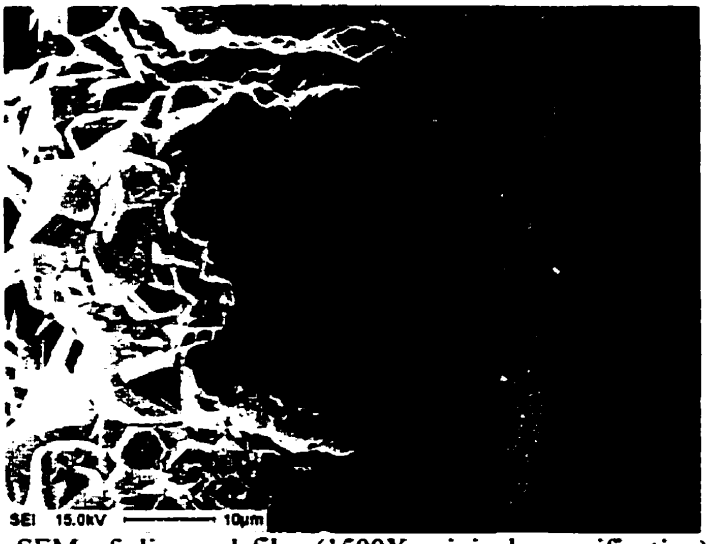

(d) Cross-section SEM of diamond film (1500X original magnification); Initial substrate temperature 935°C, Deposition Time: 41 min., +500V Bias Voltage, estimated average film thickness: 52.1 μm.

Figure 6.5.3 : Examples of Cross-Section SEM Micrographs of Diamond Films.

The diamond film growth rate of continuous films is evaluated by dividing the estimated film thickness by the total deposition time, including the initial nucleation time. Figure 6.5.4 summarizes the average growth rate of the diamond film as a function of bias voltage applied during the growth stage. A linear growth rate is assumed.

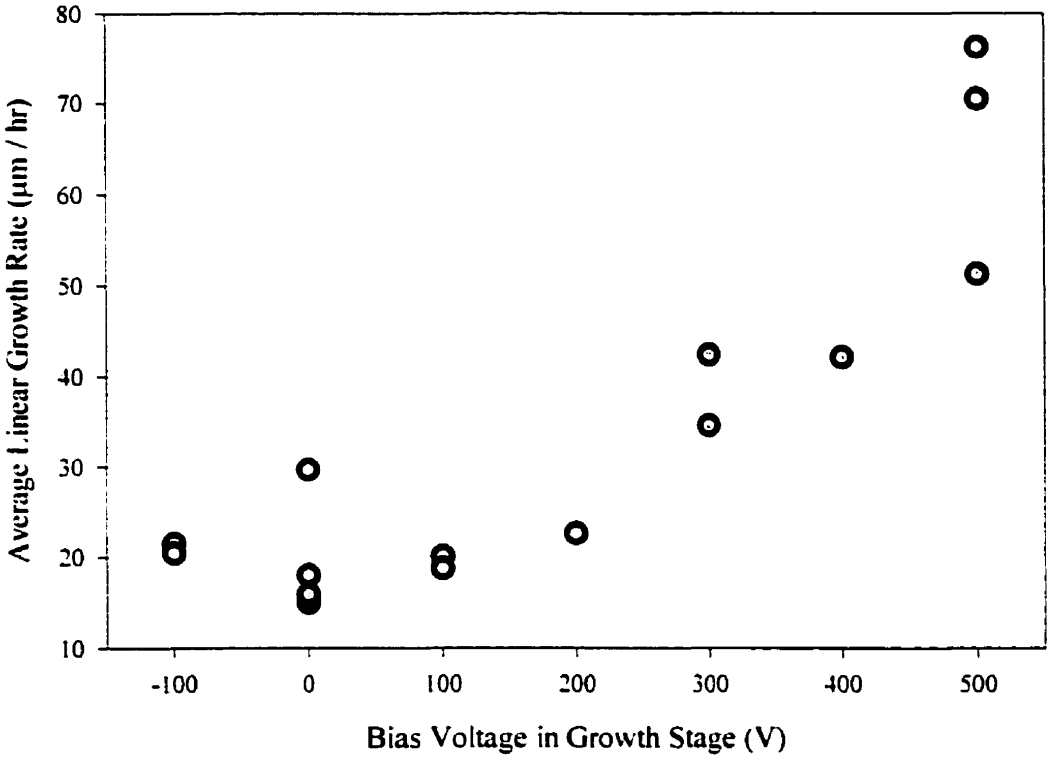

Figure 6.5.4 : **Average Linear Growth Rate versus Bias Voltage.**
Films composed of defined diamond crystal features; Substrate temperature: 890°C ±33°C (95% Confidence); Total Deposition Time: 40 to 62 min.

An increase in film growth rate from approximately 20 μm/hr at conditions around the floating potential to up to 78 μm/hr at high positive substrate bias is observed. Deposits from strong negative bias conditions are not considered because of their high non-diamond content. An augmentation in film growth rate is experienced at a bias above + 200 V.

7. Substrate Probe Measurements

The deposition surface of the substrate can be used as an electrical probe. The use of electrical probes is a common diagnostic technique in non-thermal discharges, but quite difficult and very rarely applied in thermal plasmas. The current drawn by a probe as a function of probe voltage can, in principle, yield information about the plasma state. Simple interpretation of current-voltage characteristics is, however, severely limited by a number of operational requirements. Classic probe theory is only applicable to very low-pressure, high-density plasmas using very small probe dimension (less than 0.3 mm). Other constraints include the absence of any rf voltage, gas cooling and thermal boundary layer, plasma flow and surface contamination effects. Using the deposition surface as the current collecting electrode in our thermal plasma is not intended to characterize the free flowing plasma, nor does it meet the criteria to apply Langmuir probe theory. This is mainly because the plasma in the vicinity of the substrate probe is substantially changed from the free stream conditions by the presence of the probe (see section 9.1). However, our probe is not as intrusive as to change the plasma free stream.

The electrical probe measurements can give information about the charged particle transport between the gas phase and the deposition surface, which is of utmost importance in the CVD process. The diamond growth depends critically on the plasma-substrate interface (boundary layer), and substrate bias effects on the growth are necessarily coupled to charged particle motion.

7.1 Current-Voltage Characteristics

The current collected from the plasma as function of probe voltage is shown in Figure 7.1.1 for a pristine molybdenum substrate in the beginning of a deposition experiment and for a diamond covered substrate after 30 minutes deposition.

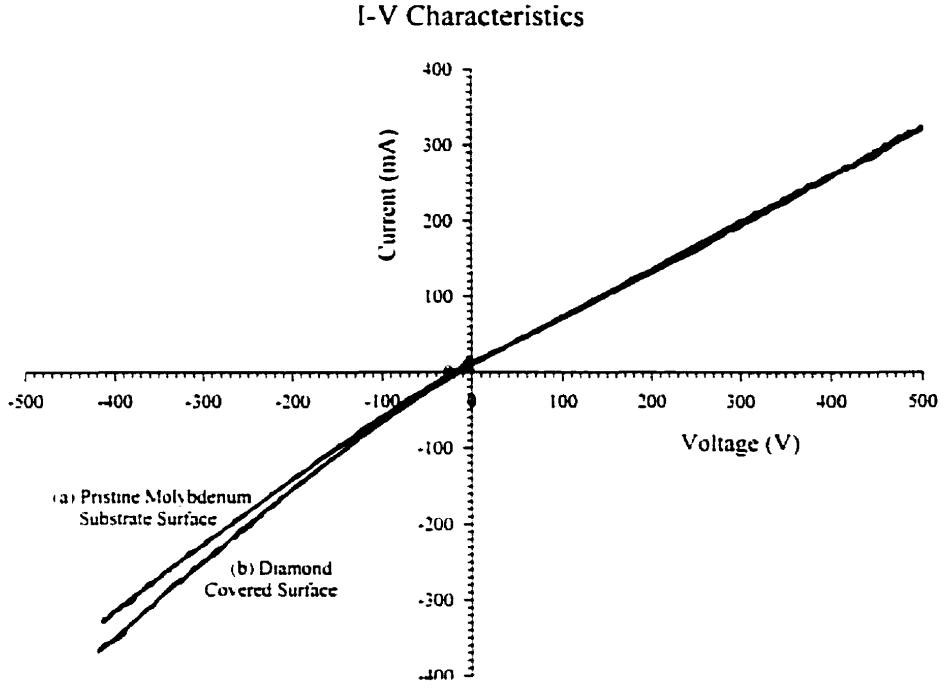

Figure 7.1.1 : I-V Characteristics for a blank molybdenum surface and for a surface covered with diamond.

The characteristics are attained within approximately 40 seconds by varying the voltage output and polarity of the dc bias power supply and recording the I-V measurements at a sampling rate of 10 Hz. To obtain measurements in the quadrants of opposing sign (i.e. positive current and negative voltage), the power supply is replaced by a variable resistor (see section 3.7).

Due to the plasma drift experienced throughout the experimental work the exact current values can vary slightly. The shape of the characteristics and their evolution is, however, highly reproducible. For the comparison depicted in Figure 7.1.1, the characteristics are obtained within the same experiment run, eliminating the effect of changes in the plasma conditions.

The current depends on the probe voltage through the entire bias range from –400 to +500 V and arises out of a difference between probe and plasma potential. For bias above the plasma potential, plasma electrons arriving on the probe generally dominate the current. Below the plasma potential, ion flux governs the negative current. Further explanation is given in section 9.1.

From Figure 7.1.1 it is evident that the current also depends on the nature of the substrate surface. In the region of negative probe potential the negative current is considerably larger when the surface is covered with diamond. A change in plasma composition and an associated increase in ion density are unlikely. The additional current is rather due to electron emission from the diamond. Similar observations have been made in low-pressure deposition systems (Beckmann et al. 1994, Lee et al. 1995, Milne et al. 1995).

Thermionic electron emission is possibly quite low at the pertinent surface temperature and cannot be responsible for the increase in electron emission current with diamond coverage. Using Fowler-Nordheim (FN) theory for field emission, Liu et al. (1995) measured an effective work function near 5.0 eV for a polycrystalline diamond surface, which is even higher than the work function for molybdenum of 4.3 eV (Schlesser et al. 1997, Fomenco 1966). According to the Richardson-Duchmann equation, a thermionic emission mechanism would imply a reduction in current with diamond coverage.

The increased current is likely caused by enhanced emission of secondary electrons due to ion bombardment if the surface is covered with diamond. The increased secondary electron emission capabilities of diamond with respect to bare molybdenum are readily experienced in scanning electron microscopy (SEM) in which the secondary electron image is greatly enhanced for diamond structures. Field emission may also play a role. Diamond is known to be an excellent material for field emission, as exploited in flat panel display application (Hong, Aslam 1995). Recent studies in field emitters have demonstrated a considerable enhancement of the field emission current of diamond covered molybdenum tips, as compared to uncoated molybdenum (Schlesser et al. 1997). The mechanism for the observed high-current low-field emission characteristics from

diamond (100), (110) and (111) surfaces is, however, not well understood (Huang, Cutler, Mikskovsky and Sullivan 1994).

The additional electron emission current from the diamond surface arises only at negative probe potential and increases with increasing negative voltage. At a positive bias voltage the two curves coincide. If the probe voltage is below the plasma potential, the emitted electrons escape to the plasma and add to the apparent ion current. Above the plasma potential, all emitted electrons are drawn back to the probe and cannot contribute to a net current. This effect is historically exploited in the use of emissive probes to determine the plasma (space) potential. In emissive probe measurements, heating a small tungsten wire probe to strong thermionic emission induces the electron emission. The bias voltage at which the hot and cold probe characteristics separate is taken as an indication of the plasma potential (Smith, Hershkowitz, Coakley 1987, and Chen 1965). In our case, the increase in electron emission from the diamond is analogous to the intensified emission of a hot tungsten wire. The diamond coated and uncoated curves begin to disagree at a probe voltage of approximately −10 V. This voltage likely represents an approximation of the plasma potential as experienced by the probe.

Since the emission current depends also on the diamond, the coverage of the substrate can be followed by monitoring the emission current at some constant negative bias voltage. Alternatively, the current can be fixed such that the probe voltage evolution is recorded. Such measurements can allow monitoring the diamond growth *in-situ*.

7.2 Current Evolution during Diamond Deposition

At a negative substrate bias, the electron emission current from the probe is expected to vary as a function of diamond formation. Figures 7.2.1 exemplify the current evolution during deposition at high negative constant bias voltage.

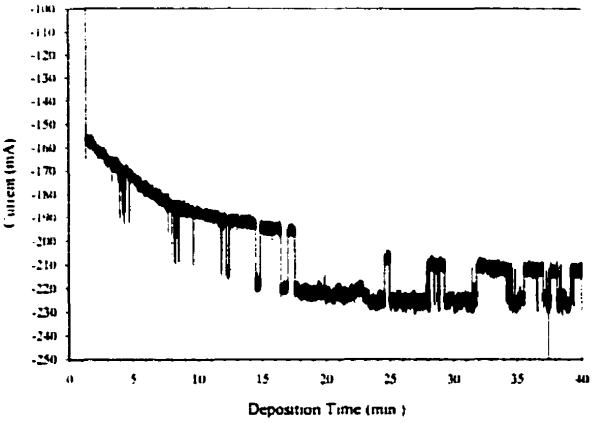

a) Current History at –200 V constant bias voltage; 5 Hz sampling rate.

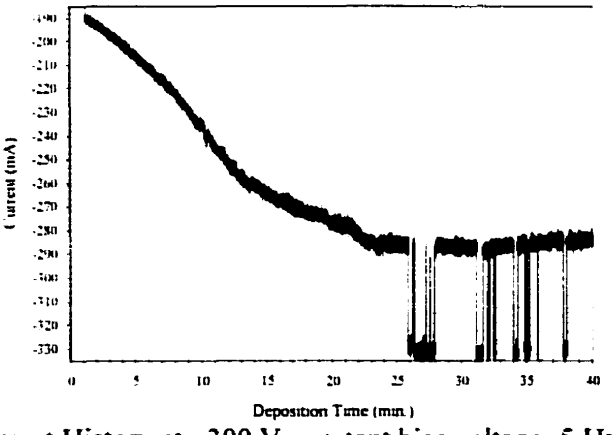

b) Current History at –300 V constant bias voltage; 5 Hz sampling rate.

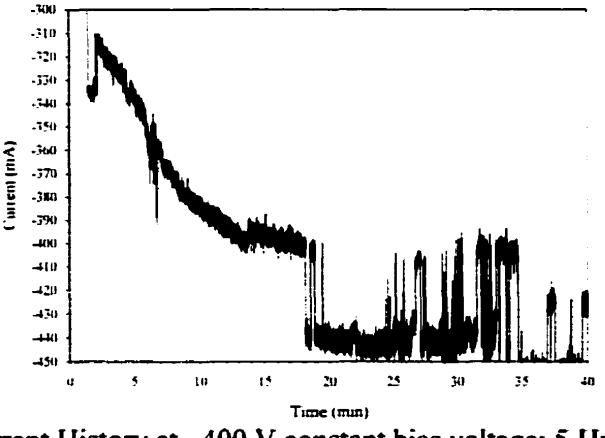

c) Current History at –400 V constant bias voltage; 5 Hz sampling rate.

Figure 7.2.1 : Current History of Deposition at Strong Negative Constant Bias Voltage.

The negative current increases asymptotically as the deposition progresses. A plateau is reached after approximately 15 minutes. With the premise that the additional current is due to electron emission from the diamond surface, the saturation occurs when the diamond coverage of the substrate area has reached its maximum value for the particular experiment. Further deposition does not increase the degree of electron emission. The noise in the data reflects fluctuations in the constant bias voltage and is due to limitations in power supply regulation. Strong current fluctuations are observed, in particular, after the current has reached its asymptotic value. These current spikes can be associated with sudden plasma ionization, caused by electron emission from hot graphite particles that co-deposit on the edge of the deposition surface. This secondary ionization is further explained later in section 7.6. Besides ionization, the maximum electron emission from the diamond surface is reached within the first 15 to 25 minutes of the deposition.

7.3 The Probe Floating Potential

When the substrate probe is disconnected from the external circuit, the net collected current is zero. Under those conditions the current contributions from collected electrons and ions as well as from emitted electrons balance exactly. With no electron emission, the number of electrons arriving at the substrate surface must then equal the number of ions. Since the electrons have a much higher mobility than the ions, electrons have to be repelled to balance the fluxes. The floating potential is than necessarily more negative than the plasma potential (V_s) (Chen 1965). Electron emission current can, in principle, cancel the effect of the higher electron collection such that the currents can be balanced even when the probe is at the plasma potential.

The floating potential of the substrate probe in the beginning of a deposition experiment assumues values in the range of –25 to –35 V. Figure 7.3.1 shows a typical evolution of the floating potential during deposition.

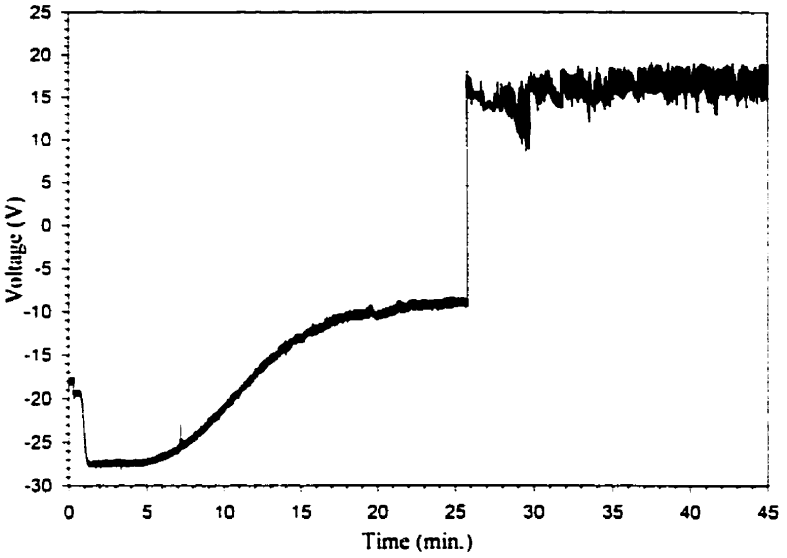

Figure 7.3.1 : Typical Evolution of Floating Potential during Diamond Deposition.

After a constant potential for the first five minutes. the floating potential increases asymptotically to a value of approximately −10 V in 20 minutes. Some time after this plateau is reached a distinct signal jump to +20 V occurs. and high voltage fluctuations are experienced. This is a highly reproducible trend. although the exact time at which this corruption occurs varies. Again. this abrupt jump is believed to be related to ionization of the plasma gas due to electron emission from graphite particles on the edge of the substrate. as will be discussed in section 7.6. A high precision is associated with the floating potential measurement since the condition of zero current is self-regulating.

The dependence of the floating potential on the diamond growth is further investigated by analyzing the nucleation density and the degree of surface coverage at different stages of the deposition. The diamond coverage is assessed from SEM micrographs, using a LECO 2005 Image Analysis System. Figure 7.3.2 overlays the floating potential with the corresponding nucleation density and area coverage as a function of deposition time.

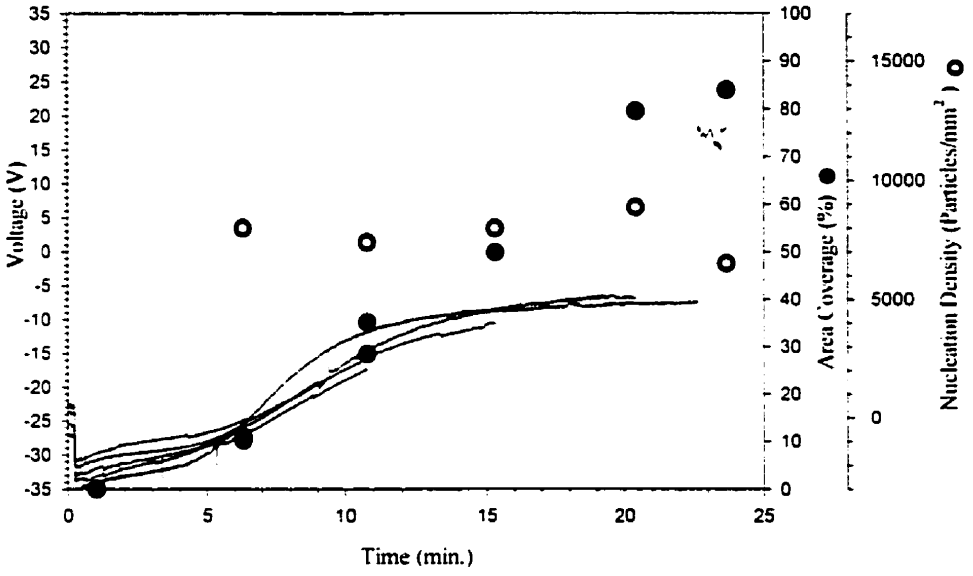

Figure 7.3.2 : Floating Potential and Diamond Film Evolution.

A constant nucleation density of approximately 8000 mm^{-2} is already attained within the first five minutes. This strongly suggests that the initial nucleation stage is terminated before five minutes. The floating potential remains more or less invariant during this period.

The surface area covered with diamond increases linearly from approximately 5 minutes to 23 minutes, until the maximum coverage is attained. As the particles grow laterally and cover the molybdenum surface the additional electron emission current forces the floating potential to rise. Consequently, the voltage correlates with the degree of coverage. However, the potential saturates to a constant value before the final coverage is attained. This is because electron emission can raise the floating potential only up to the plasma potential.

Since an emitting probe collects electrons when it is positive and emits them when it is negative with respect to the plasma potential, increasing the electron emission could let the probe float at the plasma potential, giving a direct indication of V_{space}. The plasma potential is, however, the upper limit of the floating potential of an emitting probe.

Using a classical emissive probe, consisting of a small heated tungsten wire, Kemp and Sellen (1965) found that the floating potential of emissive probes saturates as the probe emission (probe temperature) is increased, and the saturation voltage is interpreted as the plasma potential. Usually in low-pressure plasmas, the maximum emitted current cannot be sufficient to compensate for the collected current because the plasma electrons have much higher velocities. The slow emitted electrons build up in front of the substrate and create a potential barrier. Chen (1965) refers to a formation of a double-sheath. The created space-charge limits the degree to which the floating potential can be brought to the space (plasma) potential. Chang and Bienkowski (1969) carefully study the conditions for space-charge limitations and suggest that in high-pressure plasmas the charge build-up is cancelled if there are ions convected into the sheath by the plasma flow. This situation likely applies to our case, and the formation of a double sheath is not regarded pertinent. Consequently, the plasma potential can be measured directly by the saturated floating potential of approximately –10 V.

7.4 Thermal Probe Measurements

The deposition substrate can be used as a thermal probe (see section 3.5). Figure 7.4.1 illustrates the bias voltage dependence of the substrate temperature along with the corresponding I-V characteristics.

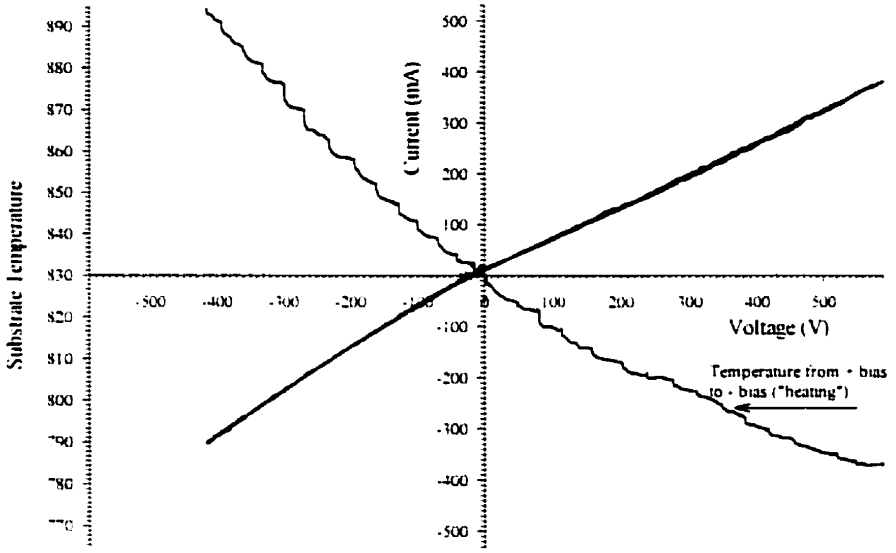

Figure 7.4.1 : Initial Substrate Temperature Dependence on Bias Voltage.

An increase in substrate temperature at negative bias is noticed. At a slightly lower rate, the temperature decreases at a positive bias. At lower substrate temperature (around 700 °C at no bias), the curve usually saturates to a constant value in the positive voltage range. The temperature variation can be attributed to ion recombination and ion bombardment energy that add to the heat flux at negative voltage. At positive voltage, the plasma ions are gradually repelled. This will be further discussed subsequently in section 9.2. A strong variation in temperature with bias voltage is only observable on a pristine substrate in the beginning of a deposition experiment. Once the substrate is covered with diamond, additional heating and cooling mechanisms mask the effect of ion flux. Since the temperature varies appreciably during the course of a deposition, in particular in the beginning of the experiment, distortions and hysteresis cannot be avoided. The recorded temperature-voltage characteristic must be considered an approximation.

7.5 Temperature Evolution during Diamond Deposition

The temperature of the molybdenum substrate cylinder is measured *in-situ*, 5 mm below the substrate surface. Although the measurement is indirect, it can reflect the evolution of the actual surface temperature. Appreciable changes during deposition are observed. Figure 7.5.1 depicts representative examples of temperature evolution during deposition under floating substrate conditions and constant bias voltage conditions. The corresponding electrical measurements are included to illustrate their functional relationship.

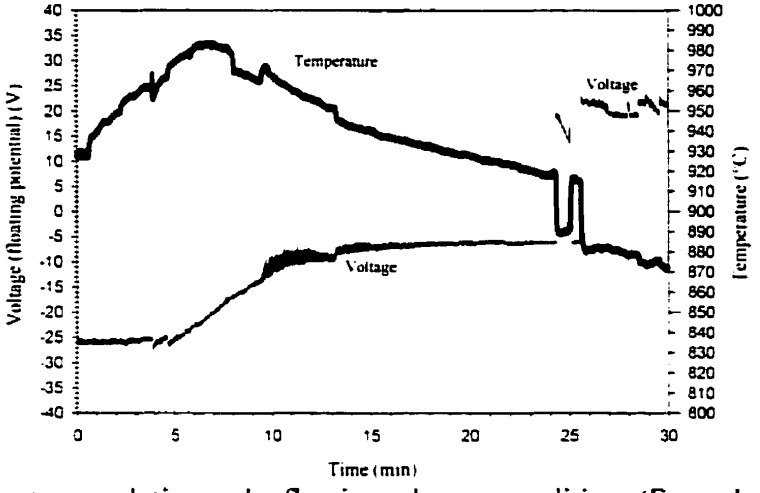

a) Temperature evolution under floating substrate conditions (Example 1)

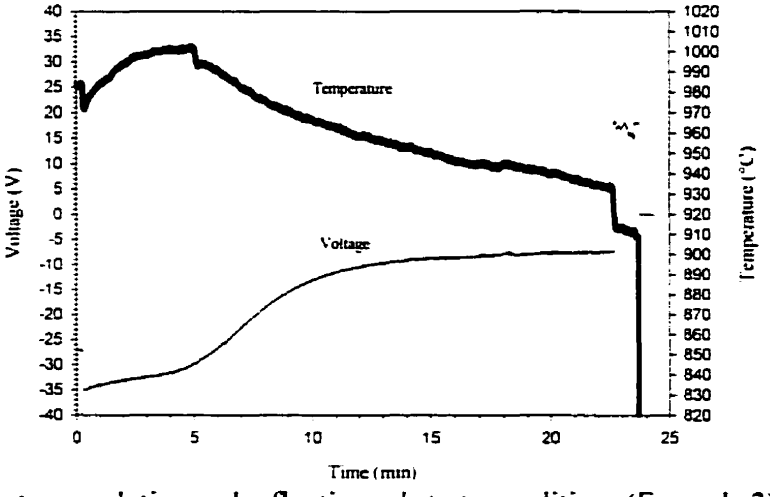

b) Temperature evolution under floating substrate conditions (Example 2)

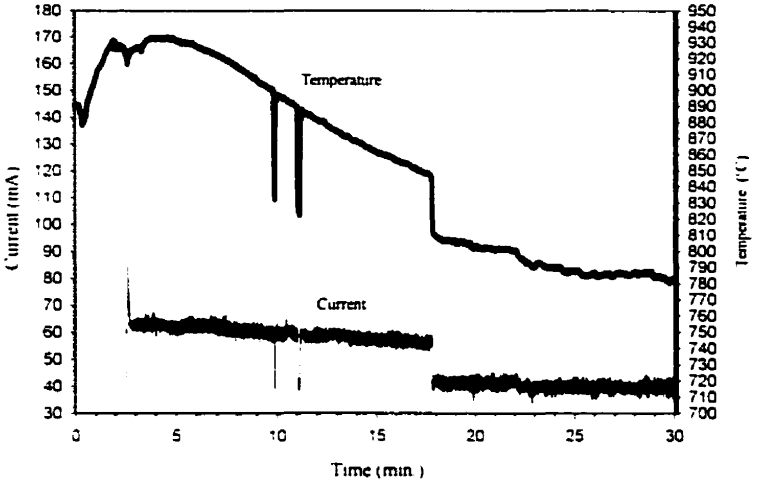

c) Temperature evolution at +100 V Bias Voltage (Current measured through 2.5 Amp Shunt)

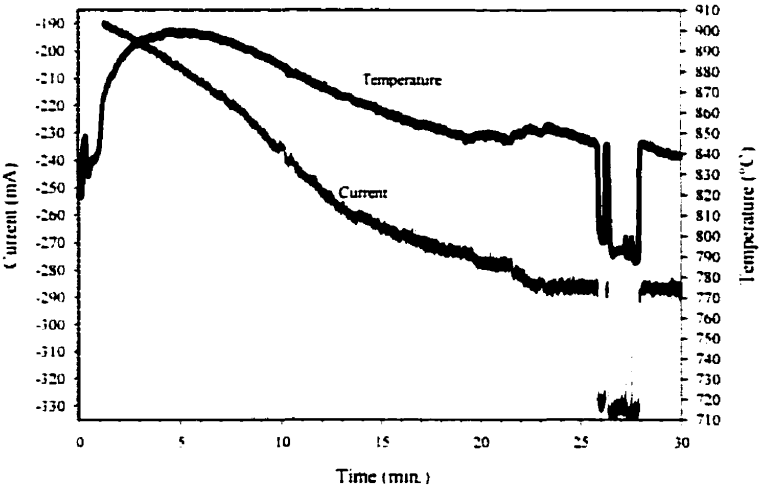

d) Temperature evolution at -300 V Bias Voltage (Current measured through 1.0 Amp Shunt)

Figure 7.5.1 : Temperature Evolution during Diamond Deposition.

The temperature increases to its maximum value in the first five minutes of the deposition. during the time when the initial diamond nucleation occurs. After five minutes the measured temperature starts to decrease. The rate of temperature change gradually decreases until. after approximately 15 minutes, the temperature declines linearly with time. The temperature never reaches a constant value even in experiments

exceeding 60 minutes. In the later part of the experiment, the temperature follows the current or voltage spikes. In these instances, the temperature drops abruptly by 20 to 40°C. This temperature evolution is very reproducible throughout the experimental work.

It is possible that the apparent temperature rise in the beginning is caused by the formation of molybdenum-carbide at the temperature measurement location on the substrate cylinder. Since the carbide has a slightly higher emissivity than pure molybdenum, the change in emissivity would appear as a temperature rise.

As the substrate gets covered with diamond, the emissivity of the top surface changes drastically such that radiation cooling of the substrate may become an important factor. The temperature consequently decreases until most of the surface is covered. As the diamond particles grow laterally and in the direction of the free surface, the deposit increases in thickness. Even though diamond has a high thermal conductivity, the formation of a more or less porous film necessarily insulates the underlying molybdenum substrate from the heat flux of the plasma. Since only the temperature of the molybdenum cylinder is measured, a build up of insulation is recorded as a temperature decrease. Conversely, the top surface of the diamond film becomes insulated from the water-cooled molybdenum such that the temperature of the actual deposition surface increases. Evidence for the thermal insulating properties of the polycrystalline diamond deposit obtained in our experiments is presented next.

The combined effect of radiation cooling and thermal insulation build up causes the high rate of decline in measured temperature in the first 15 minutes of deposition. The subsequent linear temperature decrease may reflect a linear growth rate of the diamond film normal to the surface.

7.5.1 Evidence for Thermal Insulation Build-Up

Since diamond is known to possess high thermal conducting properties, some evidence for the above interpretation of the measured temperature decrease as an insulation build-up is required.

For this purpose, two identical substrate cylinders are prepared in such a way that thermocouples can be installed on the backside. The cylinders are mounted next to each

other such that a hot air jet, generated by a heat gun, can heat the other end in stagnation flow simulating the situation in the plasma. The temperature rise in the two substrates is recorded simultaneously. The samples are heated from room temperature to approximately 250°C. One substrate serves as a reference, and the other as a blank. Ideally, there should be no temperature difference. The blank is now coated with a diamond film under standard operating conditions for 50 minutes. Again using the air jet, the temperature rise of the coated sample is compared. Figure 7.5.2 evaluates the temperature difference of the diamond coated and uncoated sample with respect to the reference as a function of heating time in the air jet.

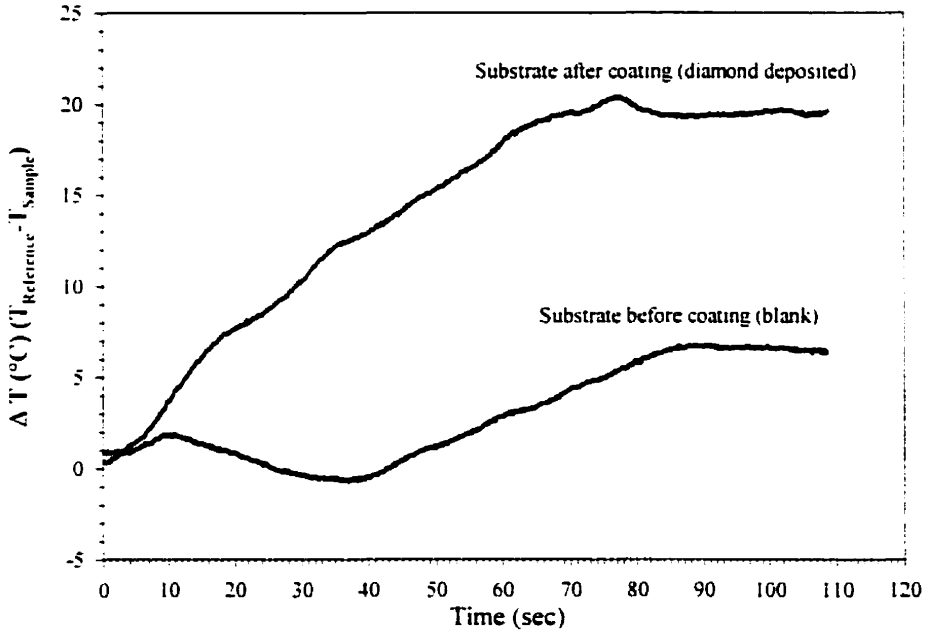

Figure 7.5.2 : Average temperature difference between uncoated sample and reference and between coated sample and reference during heating in air jet (three measurements each).

Since the difference is expressed as reference minus the sample temperature, the result shows a colder coated substrate. The resistance to heat transfer must then be attributed to thermally insulating properties of the polycrystalline diamond film.

This test supports the idea that the linear decrease in measured temperature is a consequence of thermal insulation buildup, and in turn reflects an increase in actual surface temperature during diamond deposition.

7.6 Ionization Stage

Random signal spikes, usually in the later period of the deposition experiment, corrupt the current, voltage and temperature measurement. These abrupt changes can be interpreted as a local ionization of the plasma gas in close vicinity of the probe. The increase in ion density manifests itself as an apparent increase in the plasma potential.

Yan et al. (1996) studied the use of emissive probes in plasmas at a pressure of 1 Torr, which is traditionally considered a high pressure for probe measurements. Their findings show that in a weakly ionized gas there is a strong tendency for a current discharge to be established near the probe. Electron emission from a strongly heated emissive probe can perturb the local plasma potential since the emitted electrons can acquire enough energy to ionize the gas. At the elevated pressures, the ionization can substantially increase the local plasma density around the sheath region because the ion mean free path becomes smaller than the sheath dimension. This effect gets worse with increasing electron emission or when the probe is biased far above or far below the plasma potential.

To investigate this possibility, our electrical characteristics are further explored. Figure 7.6.1 shows current-voltage characteristics taken at three different stages of the deposition process: on pristine molybdenum substrate in the beginning (a), on a diamond covered substrate after 30 minutes deposition (b), and finally during the ionization stage (c), after the distinct jump in current, voltage and temperature has occurred.

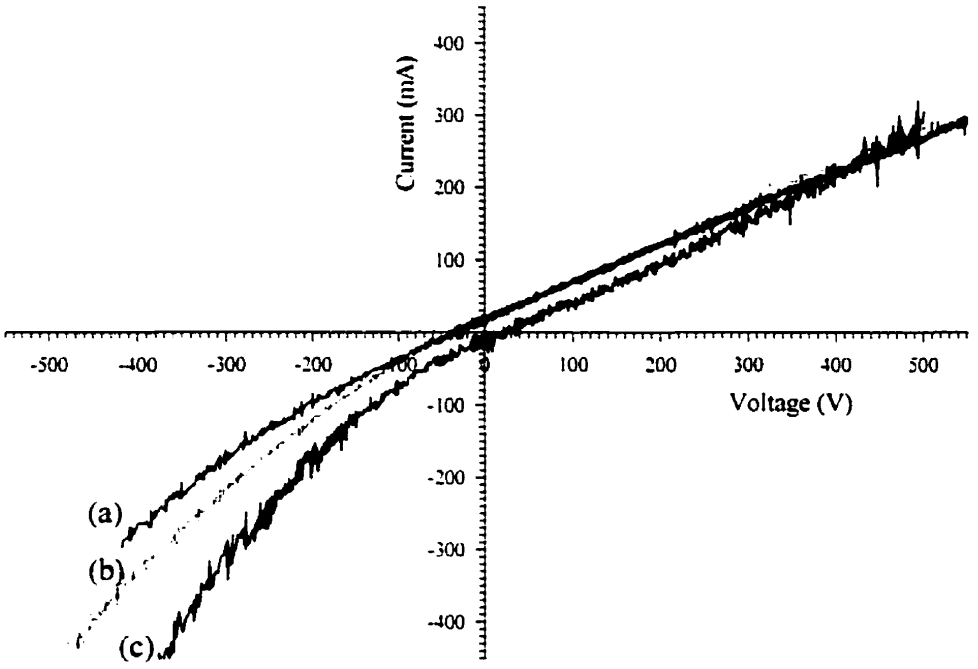

Figure 7.6.1 : Current-Voltage Characteristics at the Different Deposition Stages.
Pristine Molybdenum Substrate (a); Diamond Covered Substrate (b); During Electron Emission induced Ionization (c).

At ionization, not only does the floating potential jump to approximately +20 V but also the entire characteristic is shifted to higher voltage values in a nearly parallel fashion. This observation is highly reproducible and compatible with the interpretation of an increase in apparent plasma potential since the current depends on the potential difference between the probe and the plasma. At strong positive and negative bias, slightly higher collection currents are observed as expected from the increase in charge carriers available.

The onset of the discontinuity in the electrical measurement coincides precisely with the generation of a single very bright spot on the graphite, similar to a cathode spot seen in dc arc attachments to an electrode. The associated temperature drop possibly

reflects the additional radiation cooling of the substrate from that graphite spot. The photograph in Figure 7.6.2 shows a side view of the substrate immersed in the plasma jet at such a moment. Besides glowing graphite particles at the edge of the substrate surface, a distinct arc spot superimposed on the graphite glow can be discerned.

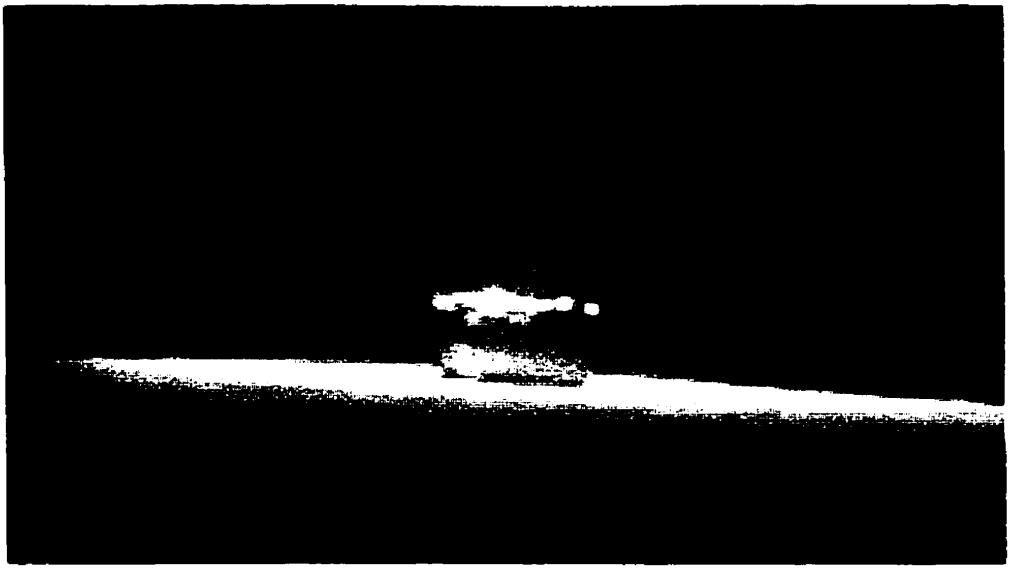

Figure 7.6.2 : Photograph of Substrate during Deposition, with Local Ionization Spot.

Our experiments generally yield a uniform diamond deposit over most of the flat deposition area. However, on the outer edge of the surface a graphite rim is often formed. Since the plasma heats the substrate edge from more than one side, the higher edge temperature possibly endorses the graphite growth. The highly porous graphite filaments have little thermal contact to the substrate and are heated by the plasma to strong thermionic electron emission. These emitted electrons cause the local ionization. Accordingly, the onset of graphite formation and ionization is promoted at a high substrate temperature at the outset, or on the top surface of the diamond film that has

gradually reached the critical temperature. Graphite particles attached to a continuous diamond film are shown in the photograph in Figure 7.6.3. The graphite particles have formed on top of a closed continuous diamond film, supporting the idea of an increasing surface temperature during deposition.

Figure 7.6.3 : Diamond Film with Graphite Particles.

In this experimental work it has not been found possible to eliminate the graphite formation without jeopardizing the diamond growth. However, a relationship between this secondary ionization and the bulk diamond formation is not apparent. Understanding the origin of this disturbance assists significantly in the interpretation of the probe measurements.

8. Effect of Substrate Temperature on Diamond Deposition

Substrate temperature is known to be an important parameter in chemical vapor deposition of diamond. For diamond films with high levels of crystal perfection, the temperature is usually in the range of 900°C to 1100°C (Baldwin et al. 1994)(Oberste Berghaus 1996). Reduction in surface temperature results in the growth of microcrystals only, creating ball-shaped cauliflower structures. At high surface temperatures graphite growth is promoted. The variations in substrate temperature, as experienced in this work, make it necessary to isolate the effect of temperature on the growth in our deposition system. Changing the length and position of the copper sleeve, which provides the thermal contact between the substrate probe and the water-cooled base, can in principle control the surface temperature. However, the temperature is highly sensitive to small variations in the thermal contact resistance for different sleeves and positions. For a comparative study at otherwise identical conditions it is preferential to change the substrate length. The molybdenum cylinder length is varied from the standard of 26.0 mm in 0.5 mm increments. Assuming a heat flux of 45.5 W, 0.5 mm in length would translate into a temperature difference on the surface of approximately 20°C. SEM micrographs of the films after extended deposition are shown in Figure 8.1.1 for 25 mm through 26.5 mm long substrates. The original magnification is 1500. No substrate bias is applied and the probe is left floating throughout the experiment.

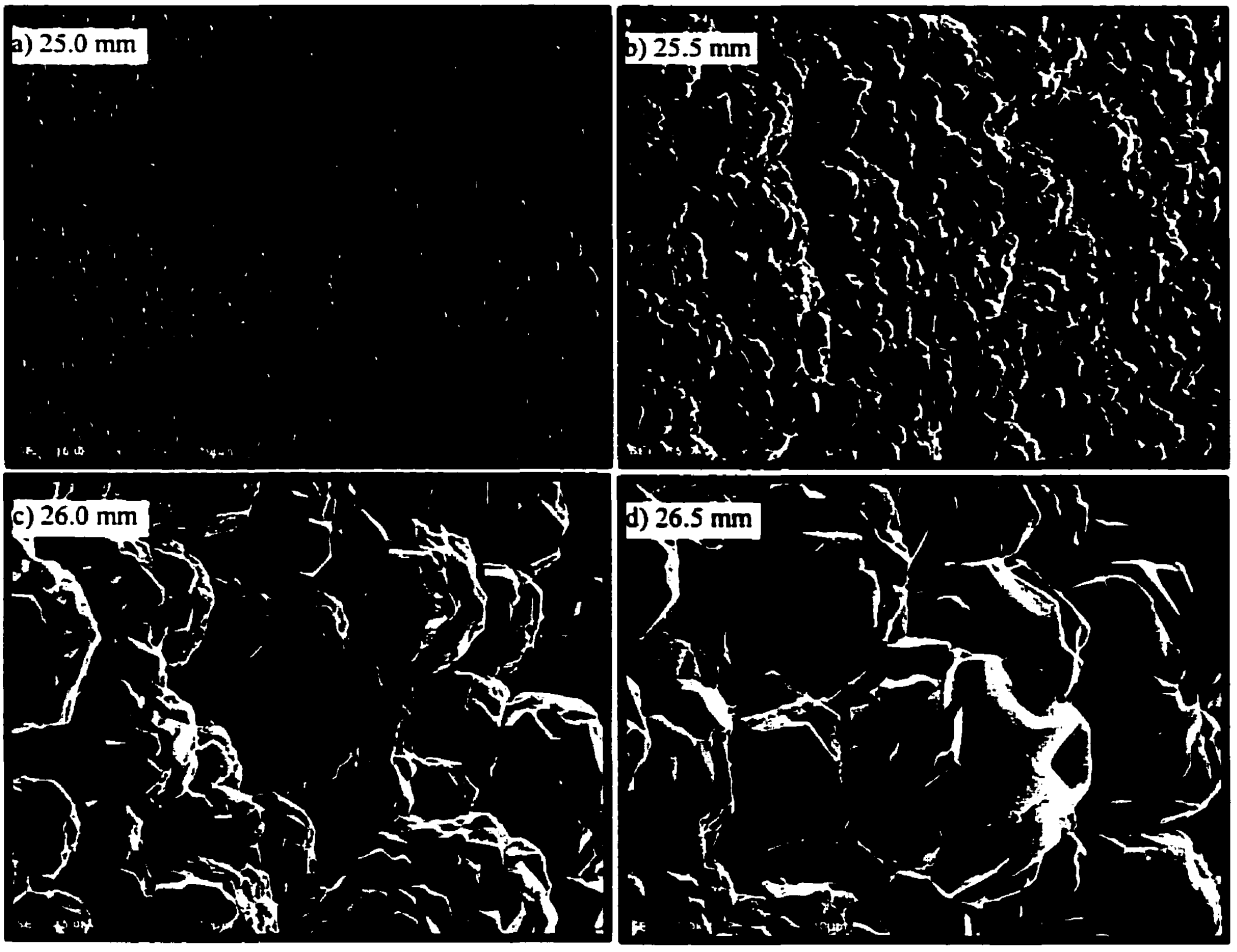

Figure 8.1.1 : SEM Micrographs for Surface Temperature Variations.
Surface Temperature increases by 20°C in 0.5 mm steps from a) to d).

At the lowest surface temperature (a), only amorphous carbon is formed, and no diamond crystal features can be identified. With increasing temperature, sample (b), triangular crystal faces of approximately 1 μm diameter appear. The crystal size then increases in (c) and (d) to 5 μm and 10 μm, respectively.

Raman Spectroscopy confirms this improvement in diamond quality with surface temperature in the range investigated. The Raman spectra, corresponding to the samples in Figure 8.1.1, show the enhancement of the diamond signal at 1332 cm^{-1} with respect to the graphite signal from (a) to (d).

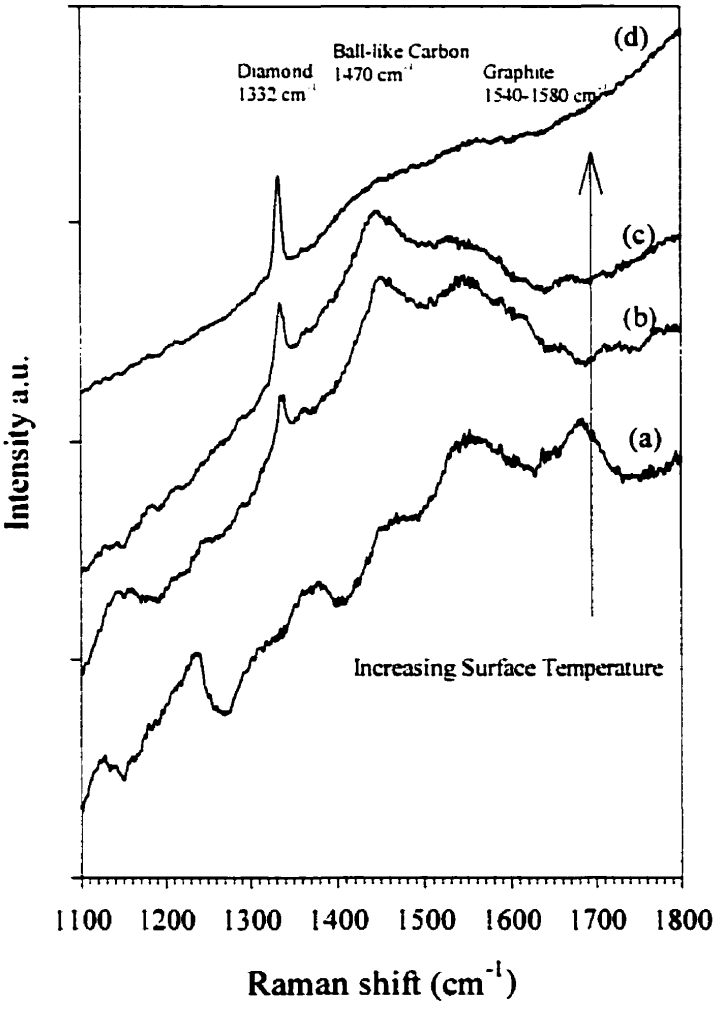

Figure 8.1.2 : Micro-Raman Spectra of Deposition with Different Substrate Length
(a) 25.0 mm, (b) 25.5 mm, (c) 26 mm, (d) 26.5 mm. An increase in surface temperature in 20°C increments is associated. Spectra from Renishaw 3000 Ramascope with 541 nm excitation.

The voltage and temperature histories for these experiments are recorded in Figure 8.1.3.

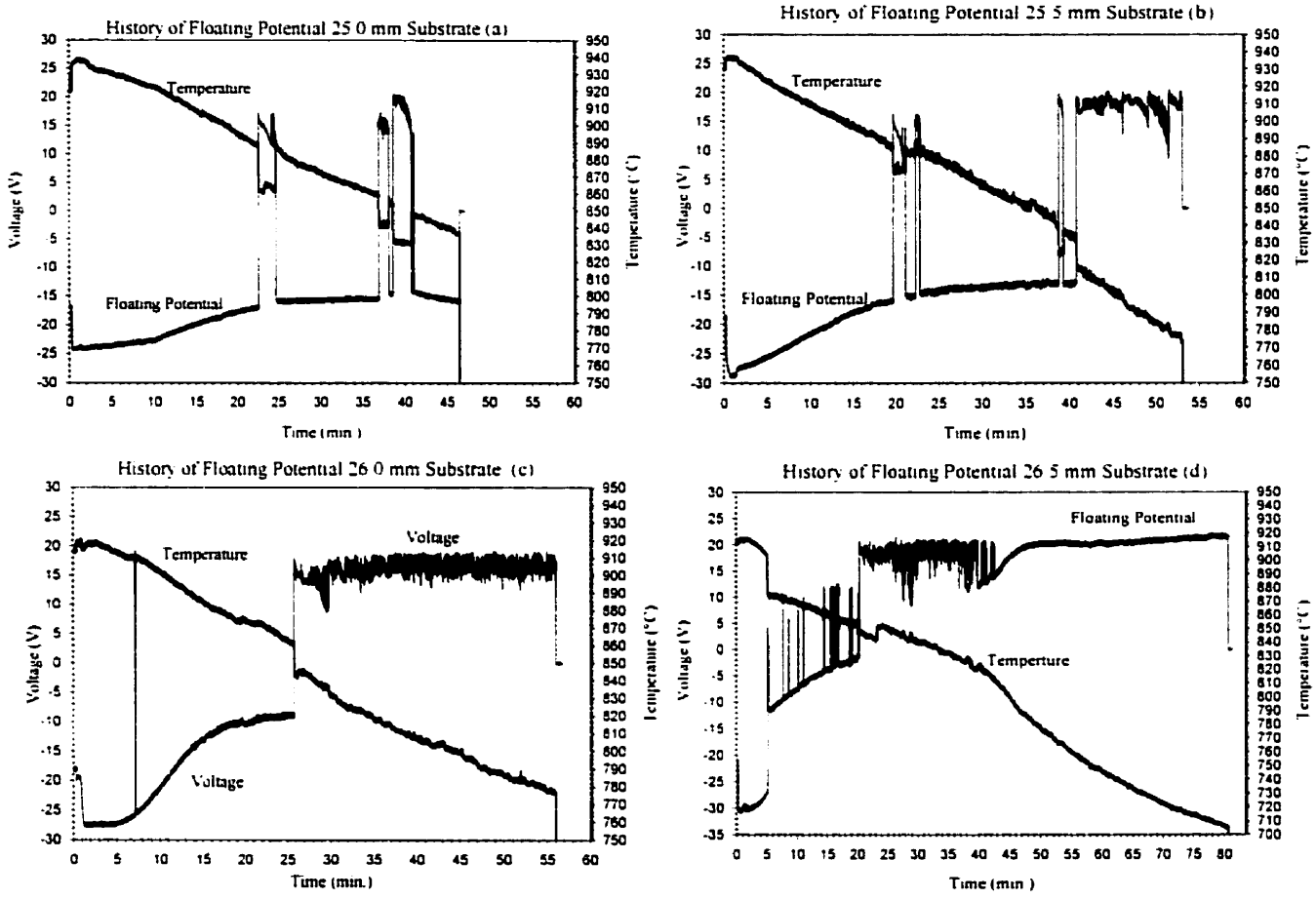

Figure 8.1.3 : Floating Potential and Temperature Evolution for Deposition at different substrate length.

The measured initial temperature in all four experiments is approximately 930°C. Since the measurement position with respect to the cooled base is the same, the invariant initial temperature indicates identical heat flux from the plasma. The high initial temperature in this particular set of experiments also suggests that the heat flux is possibly larger than 45.5 W. This implies that the surface temperature difference induced by the 0.5 mm change in substrate length is substantially higher than the 20°C originally estimated. From the histories (a), (b) and (c) it is seen that the asymptotic value of the floating potential, which is related to the plasma potential, increases for increasing

surface temperature. This is possibly related to thermal boundary layer effects, when a thicker boundary layer, as in the case of a cold substrate, decreases the ion density above the probe surface. By providing a lower surface temperature, the onset of sustained secondary ionization by graphite particles is delayed since the formation of the graphite is suppressed. Besides some short occurrences, an ionization phase is not encountered in the coldest case (a). Ionization starts after 41 minutes in case (b) and after 26 minutes in case (c). In the hot substrate case (d), ionization is immediate, and after 45 minutes a continuous graphite ring emits electrons to such a degree that additional ionization does not require arc spot formation.

8.1 Plasma Drift and Experimental Variability

An appreciable drift in the plasma characteristics is experienced during the course of the experimental work. This can be mainly attributed to aging and erosion in the plasma-generating torch. Because the probe is located in the tail flame appreciably far from the torch. the effect of plasma variations is amplified on the substrate. In an attempt to compensate for these deviations. the plasma power is slightly adjusted to yield an invariant heat flux to the substrate holder as monitored on the cooling water rise. An invariant heat flux at the same plasma composition implies identical boundary layer and diamond growth conditions. The heat flux to the substrate assembly is successfully maintained at 1810 W ± 30 W (95% confidence), with only minor adjustments in plate power. Particular attention is given to compare diamond growth behavior only within an experimental set. which is performed over a short time period during which the plasma conditions are invariant and reproducible.

Our results illustrate that both the substrate bias voltage and the substrate surface temperature substantially affect the diamond deposit. Considering the high sensitivity of the temperature measurement. which detects temperature changes even during the course of an experiment. a variability of ±70°C in initial temperature reading is not surprising. The effect of bias voltage can nonetheless be isolated from temperature effects, since the temperature variations are random and are not correlated to the bias from one experiment to the next. In terms of the diamond growth within one experiment the two parameters are inversely related. such that a positive bias improves the deposit even though it cools the substrate. Consequently. the effect of these two parameters on the deposit can be considered unrelated in our investigation.

DISCUSSION

9. Discussion

Using the substrate surface as an electrical and thermal probe gives a unique insight into the bias assisted diamond CVD process, provided that the measurements can be accurately interpreted. The primary focus in Chapter 7 is to exploit the electron emission capabilities of diamond. Besides monitoring this emission current to follow the diamond development, comparing emitting and non-emitting characteristics yields direct information about the plasma potential. A plasma potential of approximately −10 V is measured. Emissive probe theory can readily be applied because the electron emission current could be isolated without having to consider the magnitude of the other contributions to the net current.

As stated in Chapter 7, electrical probes are common plasma diagnostic tools. The established probe theories have to be used with caution in our case because a large number of operational constraints are not fulfilled. However, the current-voltage behavior reflects charged particle transport between the plasma and the substrate under bias conditions, which is critical to our CVD process.

In the following, classical Langmuir probe theory is shortly reviewed. An attempt is made to identify the theoretical principles, which can and cannot be applied to the present situation. By relating the applicable concepts to our probe and plasma measurements, a basic description for our process is developed. Comparing our findings with ongoing research efforts in non-thermal and thermal CVD systems, as reported in the literature, allows to infer the governing mechanisms in bias assisted diamond CVD in the rf thermal plasma system.

9.1 Electrical Probe Theory

9.1.1 Classical Electrical Probe Theory

An electrical or Langmuir probe consists of a single electrode whose current/voltage characteristics are measured when it is surrounded by the plasma (Langmuir 1926). The plasma away from the probe is assumed to contain equal parts of positive and negative charge. When the probe is biased positive with respect to the plasma then only electrons reach the probe and a current will flow from an external circuit to the probe (electron saturation current). Equally, when the probe is biased negatively, the current will eventually be negative due to positive ion flow (ion saturation current). If the probe is held at the same potential as the plasma (space potential), both ions and electrons can reach the probe, and the current will be determined by the relative velocity of the two species. In the usual situation of higher mobility of the electrons, the current at space potential is essentially electron current. If the probe is insulated from an external circuit, then its potential will float to a value (the floating potential) at which the ion and electron currents are equal. When one or the other of the charged species is repelled (fully or partially) a region close to the probe will be deficient in that species. This region is known as the sheath.

Figure 9.1.1 shows the current/voltage characteristics of an idealized probe.

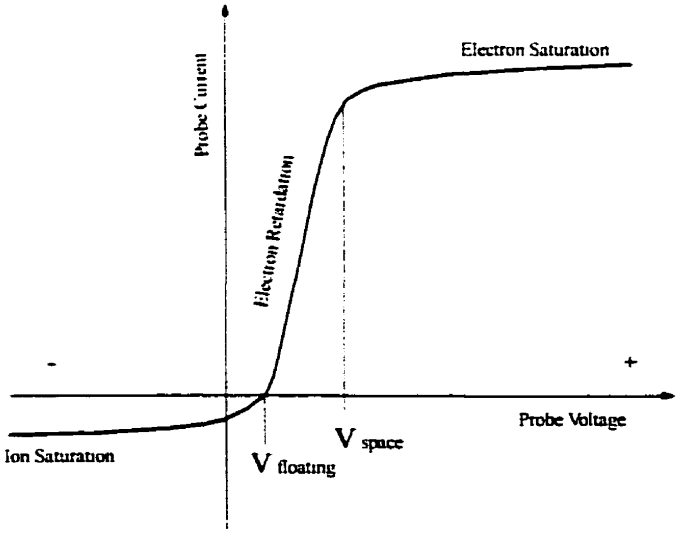

Figure 9.1.1 : Characteristics of an idealized probe.

The electron current at and above the space potential is governed by the random current density (j_r) of the electrons, which is proportional to the density of the electrons and their thermal velocity. The electrons are considered to have a Maxwell-Boltzman velocity distribution with an electron temperature T_e. It is commonly assumed that all particles arriving at the sheath edge also arrive at the surface.

$$I_{e0} = j_r \, A_S = \frac{1}{4} n_e \, e \left(\frac{8kT_e}{\pi \, m_e} \right)^{\frac{1}{2}} A_S \, . \tag{9.1.1}$$

where A_S is the sheath area, n_e the electron density, e is the electron charge, and k is the Boltzman constant, and m_e is the electron mass.

With a gradual decrease in probe voltage below the space potential (electron retardation region), ions are accelerated and electrons are repelled according to their thermal velocity distribution: at first the slower electrons and then also the faster ones. The collected electron current can be expressed by,

$$I = I_{i0} + I_{e0} \exp\left(\frac{e \, V_P}{k \, T_e} \right) . \tag{9.1.2}$$

where I is the total current to the probe, V_P is the difference between probe voltage and the space potential, and I_{i0} is the ion saturation current. The ion saturation current is obtained at a negative bias voltage when all the electrons are repelled and only the attracted ions can contribute to a net current. In analogy to the electron saturation current, I_{i0} is proportional to the ion density (equal to the electron density in a globally neutral plasma) and to the thermal velocity of the ions. However, the thermal velocity of the ions at the sheath edge is not governed by the ion temperature but rather by the electron temperature. This phenomenon is know as the Bohm criterion and assumes a presheath region in which the ions are accelerated to a velocity larger than $\sqrt{k \, T_e / m_i}$.

The plasma parameters that can, in principle, be derived form the probe measurements are the electron temperature T_e (from electron retarding region) and the electron density n_e (from electron saturation current).

This original theory was developed for stationary plasmas at very low gas pressures. Ions and electrons can move to and inside the sheath unhindered by collisions.

In addition, the probe is small such that the measured plasma is not altered form the conditions far from the probe. This implies the assumptions that both the probe radius (r_P) and the Debye shielding length (λ_D), which is a measure of the sheath thickness, are much smaller than the mean free path of ions and electrons (l_i and l_e). For the plasma conditions of interest the situation is very different, and the classical theory cannot be applied directly.

9.1.2 Probe Theory at High Pressure

In thermal plasmas at nearly atmospheric pressure, the condition that the mean free path (l) is significantly larger than the probe radius (r_P) can usually not be satisfied. The velocity distribution at the edge of the sheath will differ from the undisturbed distribution since the probe is large enough to block a non-negligible portion of the particles arriving on the edge. This causes a decrease in plasma ion density near the probe, with two important consequences. Firstly, the sheath thickness increases. Secondly, since now collisions occur within the sheath, the particle velocity is reduced from the thermal velocity to the much lower drift velocity, such that plasma flow effects may become important (see section 9.2). These factors imply that at atmospheric pressure collisions must be considered (i.e. the sheath will be many free path in thickness) and the stationary plasma theory is only valid at very low gas velocities, lower than the collision reduced drift velocity.

In high-pressure plasmas, the currents to a probe can be predicted accurately only by a complete continuum analysis of the probe plasma interactions. Detailed solution of those generalized formulations, which couple bulk fluid motion, species diffusion and convection, electron and bulk energy equations, and net-finite ionization with the equations for the electric field are presented by Meeks and Cappelli (1993) and Cappelli (1993) based on earlier theoretical works by Talbot (1960), Lam (1964), Su (1964), and Self and Eskin (1983). General review on probe behavior includes works by Chen (1965), Chung (1964) and Schott (1968). Smy (1976) reviews Langmuir probe theory and its applicability to probes in contact with high pressure and moderate temperature plasmas.

While a complete analysis of such probes is generally a complex matter, which involves a number of numerical solutions, some theories also give simple asymptotic relations, which are applicable to many situations. Approximate solutions for probe currents in flowing high-pressure plasmas are developed for various plasma and probe configurations and compared with experimental measurements. In particular, we cite the work of Clements, MacLatchy and Smy (1972), Clements and Smy (1969 – 1973), and MacLatchy (1979/1991) with the focus on identifying the governing mechanisms leading to ion and electron currents. The fundamental concept in these theories is that inside the sheath the ion motion is space-charge controlled, i.e. every ion that enters the sheath is driven to the probe surface by the electric field. The transport of charged species to the sheath edge is either controlled by diffusion or by convection. Depending on the operating parameters, such as electron temperature, mobility, flow velocity, electron density, probe radius and applied voltage, the current to the probe can be describes by a convection-diffusion or sheath-convection model.

9.1.3 Characteristic Length Scales

Debye Length:

The Debye length is a measure of the spatial extent of the deviation from charge neutrality in the plasma, and is expressed by:

$$\lambda_D = \sqrt{\frac{\varepsilon_0 k T_e}{e^2 n_e}} \tag{9.1.3}$$

with an electron temperature T_e = 4000 K and an electron density $n_e = 1.6 \cdot 10^{21}$ m^{-3}, the Debye length in our plasma is approximately $\lambda_D = 1.1 \cdot 10^{-7}$ m.

Ion Mean Free Path:

The mean free path (m.f.p.) l is the average path length traversed by a particle between successive collisions:

$$l = \frac{1}{n\sigma_0} \tag{9.1.4}$$

, where n is the number density of neutral particles and σ_0 is the total cross section for collisions. Bradley and Ibrahim (1974) measured the gaseous positive-ion collision cross-section in a methane-air combustion flame at atmospheric pressure as $\sigma_i = 1 \cdot 10^{-18}$ m^3. Since the predominant positive charge carrier in our plasma is the C^+ ion, we adopt this measured cross-section as a first approximation. At our heavy-species gas temperature of T_h = 3700 K, a total number density of $n = 7.046 \cdot 10^{23} m^{-3}$ is determined from FACT equilibrium calculation for our gas composition. The elevated ion density arising from non-equilibrium effects due to the high electron temperature (i.e. partial equilibrium) is neglected. The ion mean free path in our plasma is then estimated as $l_i = 1.42 \cdot 10^{-6}$ m.

The electron mean free path is approximated by $l_e = 1 \cdot 10^{-5}$ m. A collision cross section of $\sigma_e = 1.42 \cdot 10^{-19}$ m^2 is used, as calculated by Bradley and Ibrahim (1974) in a combustion flame at 1700 K, since the cross-section in only weakly dependent on temperature.

9.1.4 Saturation Currents

The electrical probe radius in our measurement is $r_P = 2.5 \cdot 10^{-3}$ m, much larger than the mean free paths ($l_i = 1.42 \cdot 10^{-6}$ m, $l_e = 1 \cdot 10^{-5}$ m), with the result that the ion density near the probe is depleted.

Due to the effects of a large probe, Chen (1965) shows in the limit of a small mean free path that the charged species density is depleted by a factor of $3l/4r_p$. In particular, the saturation currents at moderate bias potentials are given by:

$$I = \frac{1}{4} n_0 \bar{v} e A_P \cdot \frac{3}{4} \frac{l}{r_P} \tag{9.1.5}$$

, with the thermal velocity $\bar{v} = \left(\frac{8kT}{\pi m} \right)^{\frac{1}{2}}$. Using T_e = 4000 K, T_i = 3700 K, and the equilibrium ion/electron density at 4000 K of $n_e = 5.8 \cdot 10^{16}$ m^{-3}, the electron saturation current is $I_{e\ sat} = 5.4 \cdot 10^{-5}$ A. The ion saturation current is $I_{i\ sat} = -4.96 \cdot 10^{-8}$ A. For this order of magnitude estimation we use the Saha equilibrium electron density value as calculated from FACT at our gas composition.

The saturation currents delimit the steep electron retardation region in which the exponential relationship of current to voltage allows determination of T_e and n_e in low-pressure theory. The small values of saturation currents suggest that this all-important characteristic cannot be resolved within our experimental measurement precision. Figure 9.1.2 shows the I-V characteristics around the expected retardation region. The data are filtered to remove the random electronic noise. Although a steep slope in the I-V data is observed at around –3 V, which may indicate the region of electron retardation and the saturation currents, an exponential rise of I versus V, to be interpreted in terms of the Langmuir theory, is not obtained (see equation 9.1.2).

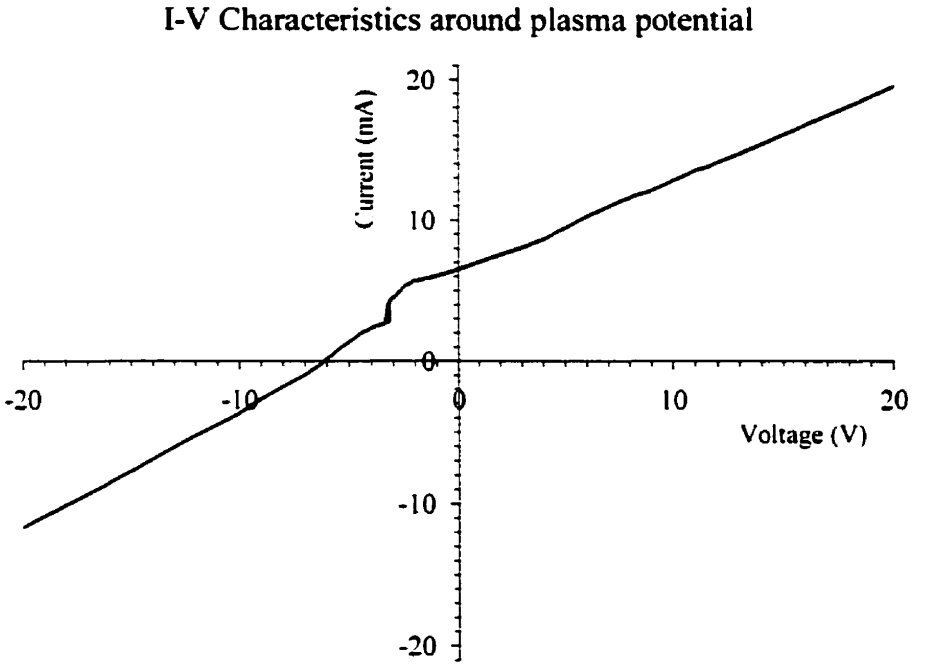

Figure 9.1.2 : I-V characteristics in the vicinity of the plasma potential.

A depleted electron density at the sheath edge implies that the local Debye length, which is related to the sheath thickness, is increased by a factor of $\sim(3l_i/4r_p)^{-1/2}$, such that $\lambda_D = 5.3 \cdot 10^{-6}$ m in the vicinity of the probe. Consequently, the collisionless condition $\lambda_D << l_i$ is no longer fulfilled and the sheath is rather described by theories that take collisions into account.

9.2 Collision Dominated Flowing Plasma Theory for Ion Collection

The general theory for flowing plasmas presented by Lam (1964) shows that plasma flow effects can be expected if the flow velocity exceeds the ion drift velocity. In the vicinity of the probe, the ion drift velocity is of the order of the product of the ambipolar electric field $E \sim \frac{kT_e}{er_p}$ and the ionic mobility μ_i:

$$v_d \sim \frac{kT_e}{er_p}\mu_i \tag{9.2.1}$$

The ion mobility is given by $\mu_i = \frac{el_i}{m_i \bar{v}_i}$, with the ion thermal velocity $\bar{v}_i = \left(\frac{8kT_i}{\pi m_i}\right)^{\frac{1}{2}}$.

For the C^- ion in our situation with T_i = 3700 K, $l_i = 1.42 \cdot 10^{-6}$ m, $m_i = 1.9927 \cdot 10^{-26}$ kg, the ion mobility is estimated as $\mu_i = 4.47 \cdot 10^{-3}$ $m^2V^{-1}sec^{-1}$. With an ambipolar electric field E ~ 138 V m^{-1} close to the probe, the ion drift velocity is in the order of v_d ~ 0.6 m/sec. Comparison with the estimated flow velocity of the plasma flame of 65.3 m/sec clearly illustrates that flow effects cannot be neglected.

Taking account of convective effects rising from the local flow velocity vector **v**, the electron and ion flow to the probe can be described by the following conservation equations:

Ion flow: $$\mathbf{v} \cdot \nabla n_i + \nabla \cdot \Gamma_i = 0 \tag{9.2.2}$$

Electron flow: $$\mathbf{v} \cdot \nabla n_e + \nabla \cdot \Gamma_e = 0 \tag{9.2.3}$$

Poisson's equation: $$\nabla^2 V = e/\varepsilon_0 (n_i - n_e) \tag{9.2.4}$$

Where diffusion and space charge effects govern the ion and electron fluxes, Γ_i and Γ_e:

$$\Gamma_i = D_i \nabla n_i + e\mu_i n_i E \tag{9.2.5}$$

and $$\Gamma_e = D_e \nabla n_e + e\mu_e n_e E \tag{9.2.6}$$

, where e is the electronic charge, n_i and n_e are the ion and electron densities, μ_i and μ_e are the ion and electron mobility, ε_0 is the permittivity of free space, V is the potential, and $E = \partial V / \partial y$ is the electric field.

Lam (1964) derives a general dimensionless governing equation for the probe current, composed of a diffusion current, a convection current and a current of ions driven by the sheath electric field. Furthermore, the following dimensionless parameters are defined.

$$\mathrm{Re}_e = (2r_p Ue)/\mu_i kT_e \quad \text{(Electrical Reynolds number)} \qquad (9.2.7)$$

$$\alpha = \lambda_D/(2r_P) \quad \text{(Debye length/probe radius)} \qquad (9.2.8)$$

$$\chi = eV/kT_e \quad \text{(Dimensionless potential)} \qquad (9.2.9)$$

Further detail is given in the review article by Smy (1976).

Depending on the operating regime of the probe, simplifying assumptions are possible, which effectively decouple the boundary layers from the sheath effects. Smy (1976) illustrates that if $R_e\alpha^2\chi^2 \ll 1$, the term representing the sheath effects can be neglected, and the current is governed by diffusion and convection effects. On the other hand, if $R_e\alpha^2\chi^2 \gg 1$, the diffusion term is neglected and the current is governed by convection and sheath effects. If, in addition, $R_e\alpha^2<1$, then all ions convected to the sheath are driven by the sheath electric field to the probe. The quantity $\alpha\chi$ determines whether the sheath is thin ($\alpha\chi \ll 1$) or thick ($\alpha\chi \gg 1$) with respect to the probe area. Evaluation of these criteria for our plasma conditions with r_P = 0.0025 m, U = 65.3 m/sec, T_e = 4000 K, $\mu_i = 4.47\cdot10^{-3}$ m^2/Vsec, $\lambda_D = 1.1\cdot10^{-7}$ m, and a negative bias voltage of V = -100 and V = -400 V leads to:

$$R_e = 212$$

$$\alpha = 2.2\cdot10^{-5}$$

$$\chi_{100} = 290;\ \chi_{400} = 1160$$

In comparison with the dimensions of the probe, the sheath is very thin ($\alpha\chi = 0.026 \ll 1$), even for strong bias voltage. At moderate probe potential (V=-100V) the convection-diffusion regime is likely, since $R_e\alpha^2\chi^2 = 8.6\cdot10^{-3} \ll 1$. However, at strong probe bias (-400V), the sheath-convection approach may be more appropriate, since $R_e\alpha^2\chi^2$ =0.14 ~ O(1), and $R_e\alpha^2=1.03\cdot10^{-7} < 1$.

The two simplifying cases are schematically illustrated in Figure 9.2.1. It must be noted that the probe theory is originally derived for spherical probes but qualitatively adopted here to our substrate geometry. Since the mechanisms leading to ion current are delimited by these two extreme cases, they will now be discussed in more detail.

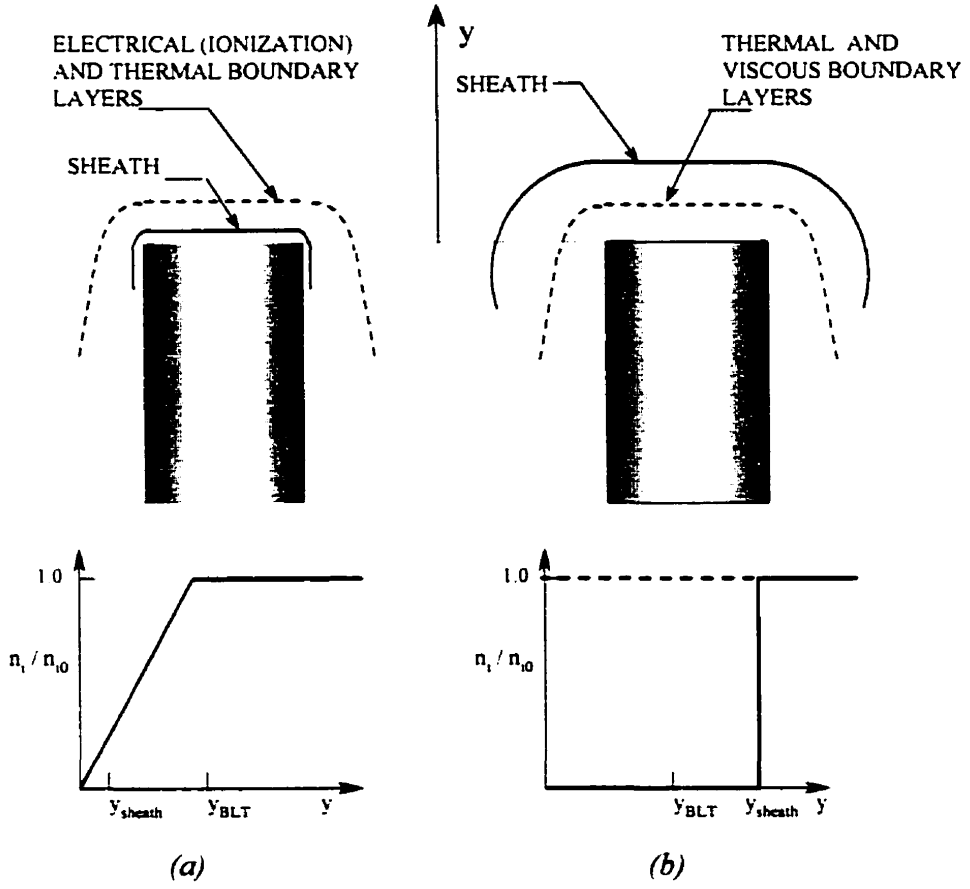

Figure 9.2.1: Schematic of Ion-Density Distribution near the Probe for Simplified Models. (a) Diffusion-convection ($R_e\alpha^2\chi^2$ «1); the sheath is thin with respect to the various boundary layers. (b) Sheath-convection ($R_e\alpha^2\chi^2$ »1, $R_e\alpha^2$<1); the sheath is thick compared with the boundary layers and all ions which enter the sheath eventually reach the probe.

9.2.1 Convection-Diffusion

In the convection-diffusion regime the sheath is thin with respect to the probe and with respect to the thermal and viscous boundary layers above the probe. In the limit of a very thin sheath, the sheath effects are neglected, and the ion flow to the probe is governed by ion convection and diffusion. In stagnation point flow, the local flow velocity on the probe surface is essentially zero (due to the non-slip boundary condition). Consequently, the ion current is given by the ambipolar diffusion across the electrical boundary layer:

$$I_i = j_i \cdot A_S = e \cdot \Gamma_i \cdot A_S = e \cdot D_a \cdot \nabla n_i \cdot A_S \qquad (9.2.10)$$

, where I_i is the ion current, j_i is the current density, A_S is the sheath area (assumed to equal the probe area) and D_a is the ambipolar diffusion coefficient. Using the Einstein relation $\mu = eD/kT$, and kinetic theory for ambipolar diffusion $D_a = 2\ D_i$ in one dimension (y denoting the coordinate perpendicular to the probe surface), the current density is given by:

$$j_i = e \cdot \Gamma_i = e \cdot 2\mu_i \frac{kT_i}{e}\left(\frac{\partial n_i}{\partial y}\right)_{surface} \qquad (9.2.11)$$

The ion density gradient on the surface is the parameter that has to be determined from equations governing the viscous, thermal and electrical (i.e. ion/electron density) boundary layers above the probe. Usually, these boundary layers are of comparable thickness such that the ion density gradient is calculated in analogy to the gas temperature gradient. Spectroscopic electron density measurements in the boundary layer above the substrate can give an approximation of this parameter. In the limit of a very thin sheath, the electron density gradient reflects the ion density gradient since charge separation in the boundary layer is not yet considered. In addition, ions and electrons are assumed to diffuse together in using the ambipolar diffusion coefficient. Figure 9.2.2 shows the measured electron density and an extrapolation to the substrate surface, assuming a linear relation and equal ion and electron density gradients.

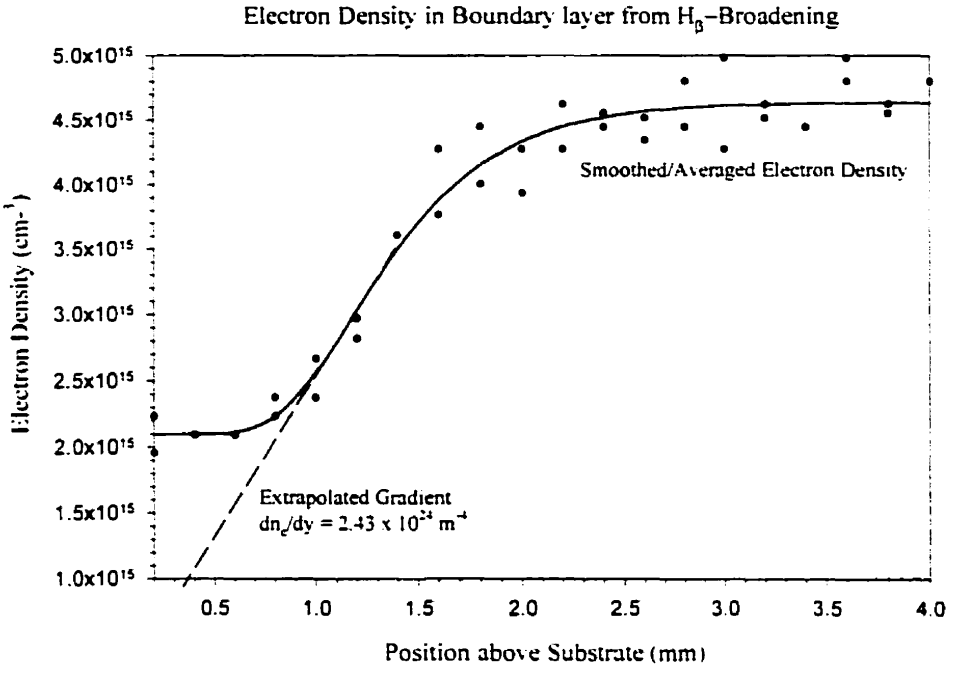

Figure 9.2.2 : Experimental determination of electron density gradient in boundary layer region with spectroscopic measurement of H_β Stark broadening.

With the simplification of the convection-diffusion model, and the approximation of the ion density gradient on the probe surface of $(\partial n_i / \partial y)_{surface} = 2.43 \cdot 10^{24} m^{-4}$, the saturation ion current is estimated as $I_i \approx 21.8$ mA. This current is measured experimentally at approximately –34 V, as seen in Figure 9.2.3. Diffusion inside the boundary layer may describe the ion saturation current at the small bias voltage value only, where the assumption of a very thin sheath may hold. However, the model neglects sheath effects such that beyond –34 V the current is expected to be independent of voltage and to saturate to the constant value. Conversely, the measured current does not saturate, but varies strongly with voltage throughout the negative bias range (see Figure 9.2.3). This suggests that sheath effects play an important role and cannot be neglected, at least not at stronger negative bias voltages.

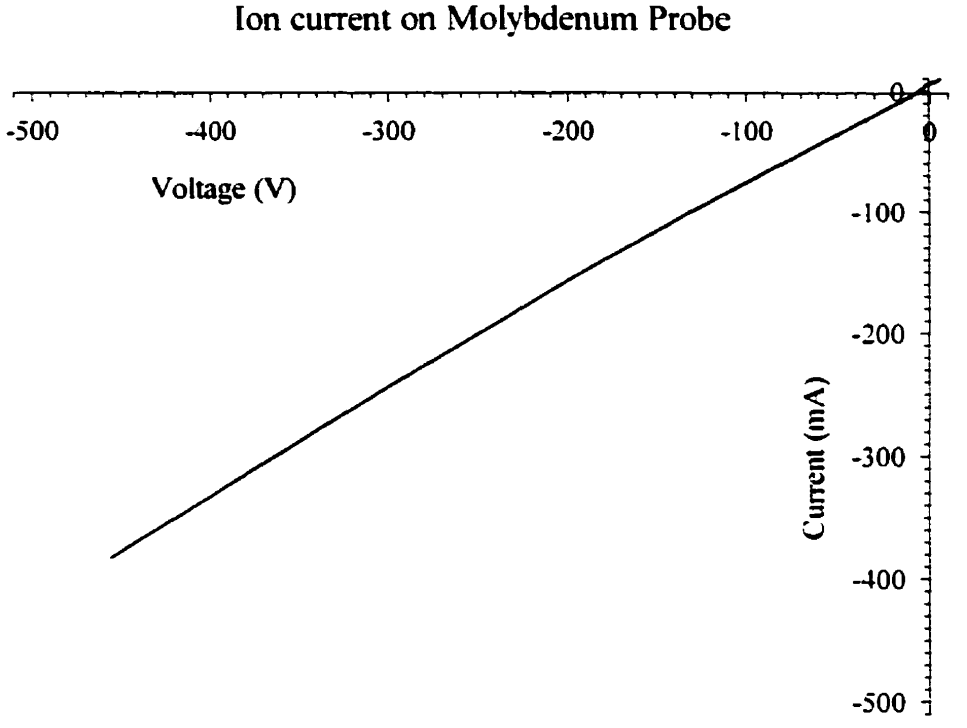

Figure 9.2.3 : Measured Ion Current vs. Voltage on uncoated molybdenum substrate at standard plasma operating conditions.

9.2.2 Sheath-Convection

If sheath effects are considered, it can be assumed that at high bias voltage all ions transported into the sheath are driven to the probe by the sheath electric field. The ion current density is described by space charge effects in the sheath, and the diffusion term is neglected:

$$j_i = e \cdot \Gamma_i = e \cdot \mu_i n_i E = e \mu_i n_i \frac{dV}{dy} \qquad (9.2.12)$$

At high negative bias voltage, the sheath is depleted of electrons ($n_e \rightarrow 0$). As a first approximation, which will allow an analytical solution for the sheath thickness, the electron density in the sheath is set to zero. The one-dimensional Poisson's equation can then be written as:

$$\frac{\partial^2 V}{\partial y^2} = \frac{e}{\varepsilon_0} n_i \qquad (9.2.13)$$

Combining 9.2.12 and 9.2.13 eliminates n_i from the equations While assuming constant mobility, and integrating the voltage through the sheath from $y = 0$ on the surface to $y = y^*$ (sheath edge) with the boundary conditions $E \rightarrow 0$ and $V \rightarrow 0$ at y^*, yields the planar, mobility-dominated space-charge equation for the sheath thickness:

$$y^* = \left(\frac{3V}{2}\right)^{\frac{2}{3}} \left(\frac{\varepsilon_0 \mu_i}{2 j_i}\right)^{\frac{1}{3}} \qquad (9.2.14)$$

This equation illustrates that the sheath thickness now varies with bias voltage. A more detailed description would require accounting for electrons emitted from the surface and plasma electrons transported into the sheath against the sheath electric field. This will be discussed shortly.

In the original sheath-convection model by Smy, the sheath is considered larger than any other boundary layer dimension. This implies that the major contribution to the probe current consists of transport of the plasma ions to the sheath edge by the hydrodynamic plasma flow. The convection current to the sheath edge is given by:

$$I_i = n_i e \mathbf{v}_{y^*} A_S \qquad (9.2.15)$$

In this extreme case of the model, the ion density and flow velocity are the free stream values. With $n_i = 1.6 \cdot 10^{21}$ m^{-3}, U = 65.3 m/sec, and $A_S = \pi \cdot r_P^2$, the ion current is $I_i = 330$ mA. This corresponds to the current measured at a bias voltage of – 400V in Figure 9.2.3 / 9.2.4. However, using equation 9.2.14 yields a sheath thickness of $y^* = 7.5 \cdot 10^{-5}$m at –400 V. The sheath thickness as a function of voltage is shown in Figure 9.2.4 for the measured current densities.

Since the thermal boundary layer (~1.5 mm) is much larger than the sheath thickness, the sheath-convection model strictly fails. The sheath edge lies within the boundary layers, and boundary layer and sheath effects cannot easily be decoupled. Consequently, exact prediction of the ion current requires a complete continuum approach, which is beyond the scope of this simplified analysis.

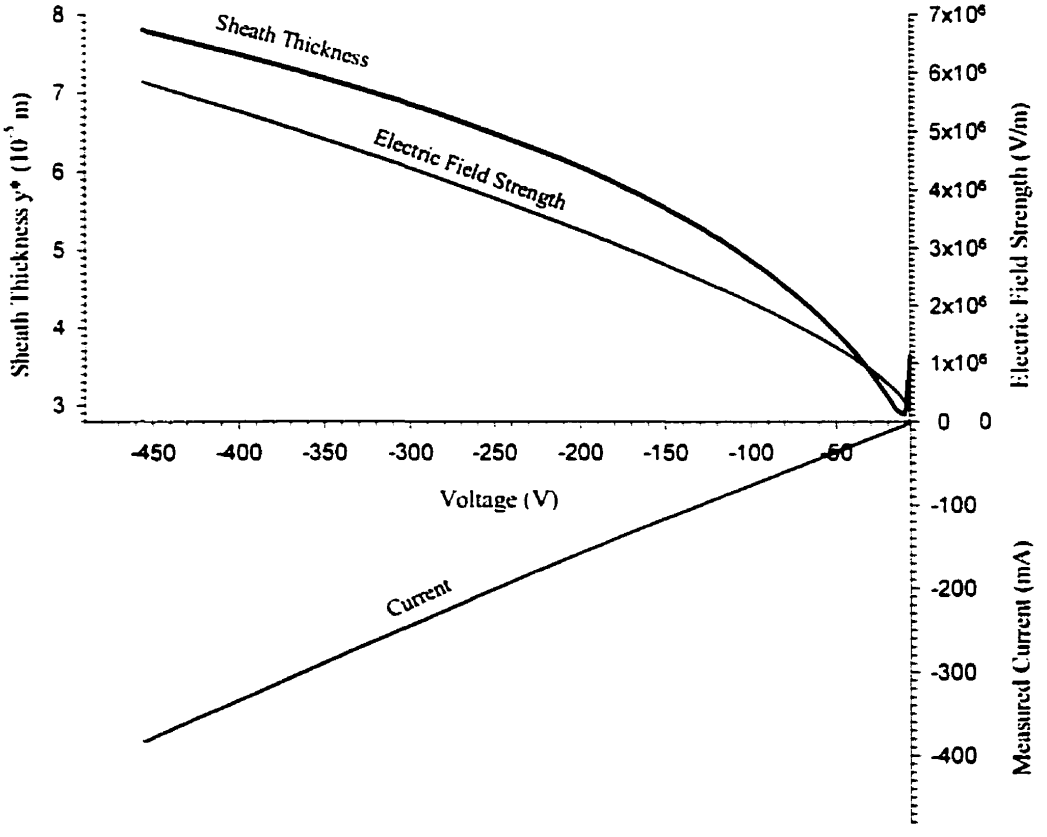

Figure 9.2.4: Sheath Thickness and Electric Field versus Voltage from mobility-limited space-charge equation.

The calculation of the sheath thickness is based on the proposition that the measured current density is due to ion flux only, and electron emission currents are neglected. To substantiate this assumption, the current density ($j_{T\text{-}F}$) due to electron emission from the substrate probe can be evaluated by the Richardson-Dushman equation for thermionic emission. Surface electric field effects are considered by using the Schottky correction:

$$j_{T\text{-}F}(E_S, T_S, \Phi) = \frac{4\pi e m_e (k_B T_S)^2}{h^3} \exp\left(-\frac{e(\Phi - \Delta\Phi)}{k_B T_S}\right) \qquad (9.2.16)$$

with the Schottky correction factor: $\Delta\Phi = \left(\frac{e E_S}{4\pi \varepsilon_0}\right)^{\frac{1}{2}}$ (9.2.17)

Besides the universal parameter notation, T_S = 1273 K denotes the surface temperature, Φ is the work function taken as Φ= 4.3 eV for molybdenum, and E_S is the surface electric field, approximated by $E_{Sheath} \cong \frac{V_{Bias}}{y^*}$. In the example of V_{bias} = -400V, the electric field strength is $E_S = 5.3 \cdot 10^6$ V/m. This relatively low value justifies the use of the Richardson-Dushman equation, as opposed to the Murphy and Good formalism for thermo-field emission (Coulombe et al. 1997). The electron emission current density yields $j_{T\text{-}F}$ = $4.35 \cdot 10^{-5}$ A/m^2, translating into a probe current of $I_{T\text{-}F}$ = $8.5 \cdot 10^{-7}$ mA. Evidently, this electron emission current is negligible with respect to the ion current, and the absence of emitted electrons in the ion rich sheath is a reasonable assumption.

The plasma electrons transported into the sheath against the sheath electric field, but not contributing to the current, are not considered in the Poisson's equation (9.2.13). Such a refinement is not warranted here, given the uncertainty about the electron energy distribution inside the boundary layer region. Without resolving the sheath structure, equation (9.2.14) may slightly underestimate the sheath thickness but, in the very least, give the lower limit.

This analysis suggests that at strong negative voltage the sheath is of appreciable thickness: however, it does not extend beyond the boundary layer. All ions entering the sheath are drawn to the probe by the sheath electric field. Since the sheath edge is imbedded inside the boundary layer region, the transport of ions to the sheath edge is governed by convection and diffusion. While considering sheath effects, an increase in probe voltage brings about an increase in sheath thickness. The observed increase in current with voltage, and the absence of saturation, is caused by this change in sheath thickness. Recalling equation 9.2.15: $I_i = n_i\, e\, \mathbf{v}_{y^*}\, A_S$, various mechanisms can be envisaged to explain an enhancement in ion current with an inflating sheath.

1) As the probe collection area is not entirely planar, the sheath area A_S is increased.

2) The sheath edge expands into the electrical boundary layer (i.e. ion/electron density gradient in the thermal boundary layer), such that the ion density at the sheath edge n_i increases. Simultaneously, the ion density gradient above the sheath edge increases, enhancing diffusion fluxes into the sheath.

3) The sheath expands into the viscous boundary layer, such that the local velocity $\mathbf{v}_{y^*}$ at the sheath edge becomes larger.

In the absence of electron emission, the measured probe current at negative bias voltages yields the ion flux to the surface. Using the substrate also as a thermal probe at negative bias conditions will elucidate some of the proposed mechanisms and yield information about the ion bombardment energy.

9.2.3 Ion Bombardment and Heating Effects

The measured substrate temperature is observed to undergo appreciable variations with probe potential. The temperature variations are particularly pronounced at negative potential, when an ion current is drawn. The major heat transfer by conduction, convection and radiation from the impinging plasma jet can be considered independent of bias voltage. In the following, only the heat flux contribution by charged species will be examined. In particular, the ions hitting the substrate transfer their kinetic energy, and recombination energy is released when a positive ion recombines with an electron on the surface.

Ions transfer a part of their potential energy when striking a surface. This heat transfer is the product of the ion flux into the sheath and the energy of recombination per ion:

$$Q_i^{rec} = j_i \, h_{rec} \tag{9.2.18}$$

The current density j_i is obtained from the measured ion current divided by the probe collection area $A_P = \pi \cdot r_P^2 = 1.96 \cdot 10^{-5} m^2$. Each incident ion releases its ionization potential h_{ion} minus the work function of the metal Φ, as an electron has to be released from the metal surface before recombination:

$$h_{rec} = h_{ion} - \Phi \tag{9.2.19}$$

Since C^- is the predominant ion in the plasma, h_{ion} = 11.26 eV (CRC Handbook of Chemistry and Physics 1990). The work function for an uncoated molybdenum substrate is taken as Φ_{Moly} = 4.3 eV (Fomenko 1966).

The heat transfer by ion bombardment is given by:

$$Q_i^{kin} = j_i \, h_{kin} \tag{9.2.20}$$

The kinetic energy per ion (h_{kin}) is a function of the degree of acceleration by the sheath electric field. For a collisionless sheath at low pressure the ion energy is determined by the free fall energy (Kersten et al. 2000):

$$h_{kin} = eV_{Bias} \tag{9.2.21}$$

In a collision-dominated sheath, the ion energy is rather approximated by:

$$h_{kin} = \frac{1}{2} m_i v_d^2 \qquad (9.2.22)$$

, where m_i=1.9927·10^{-26} kg is the mass of the C^+ ion. The parameter v_d is the ion drift velocity inside the sheath, and is given by the product of ion mobility and the electric field strength through the sheath:

$$v_d = \mu_i \cdot E_{sheath} . \qquad (9.2.23)$$

As in section 9.2.2, the sheath field strength can be estimated by $E_{Sheath} \cong \frac{V_{Bias}}{y^*}$, with the sheath thickness y* calculated from the planar, mobility-limited space charge equation.

Using the experimental current-voltage characteristics at negative bias, the increase in heat flux due to recombination and ion bombardment is evaluated. The corresponding substrate temperature rise is compared with the experimental observation. A constant ion mobility of μ_i = 4.47·10^{-3} m^2/V·sec, estimated at a gas temperature of 3700 K, is used. Without applied bias voltage, a heat flux of 45.5 W to the substrate has been determined experimentally. The contribution due to the bias is added to this value. With a thermal conductivity of molybdenum of k_{Moly} = 105 W/m·K, a correction is made for the temperature measurement position (5 mm below the substrate surface). The comparison is illustrated in Figure 9.2.5.

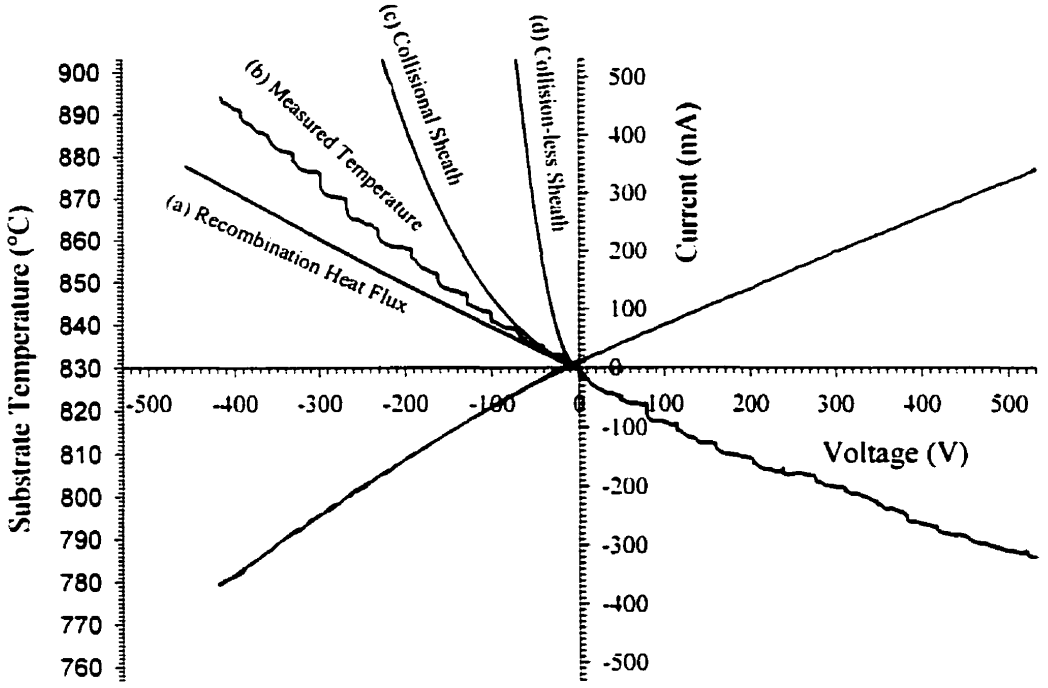

Figure 9.2.5 : Measured (b) and predicted substrate temperature rise on pristine molybdenum substrate by (a) ion-surface recombination, and recombination and ion-bombardment in (c) collisional and (d) collisionless sheath.

A very high heat flux in (d) is obtained from the free-fall equation and confirms that a collision-less sheath approach is not applicable. In the other extreme, ion-surface recombination alone (a) is not quite sufficient to explain the temperature rise. Consequently, ion acceleration in the sheath must be considered.

However, the collisional sheath model slightly over-predicts the heat flux. This can mainly be attributed to the use of the bulk ion mobility. In the thin sheath, the gas temperature is suppressed, but, with constant pressure throughout the plasma, the density will be greater than the bulk value. Since $\mu_i \propto \frac{1}{\rho\sqrt{T_i}}$, the ion mobility in the sheath will be lower that $4.47 \cdot 10^{-3}$ $m^2/V \cdot sec$. as estimated at 3700 K.

The theoretical study by Cappelli et al. (1993) assumes a constant ion mobility of $2 \cdot 10^{-3}$ $m^2V^{-1}sec^{-1}$ for an atmospheric argon plasma at 6000 K, and this value is used in many studies (MacLatchy et al. 1979, Clements et al. 1971).

Adopting the collisional sheath model, the energy of the bombarding ions can be estimated by the difference between the measured heat flux and heat flux due to recombination. C^--ion bombardment energy of approximately 4 eV at strong negative probe potential is obtained for the data in Figure 9.2.5.

The observation that the substrate temperature slightly decreases even at a positive substrate potential requires some explanation. At moderate positive bias, there is possibly convective and diffusion ion transport to the probe against the sheath electric field. Such an effect would be pronounced at a high plasma flow velocity, as reflected in a high substrate temperature. These ions are then gradually repelled with an increase in positive probe potential. Under conditions of a low substrate temperature, possibly due to misalignment of the substrate or reduction in effective plasma power, the expected temperature saturation at positive probe potential is generally observed. Figure 9.2.6 shows an example where the substrate temperature reaches a relatively constant value at positive bias.

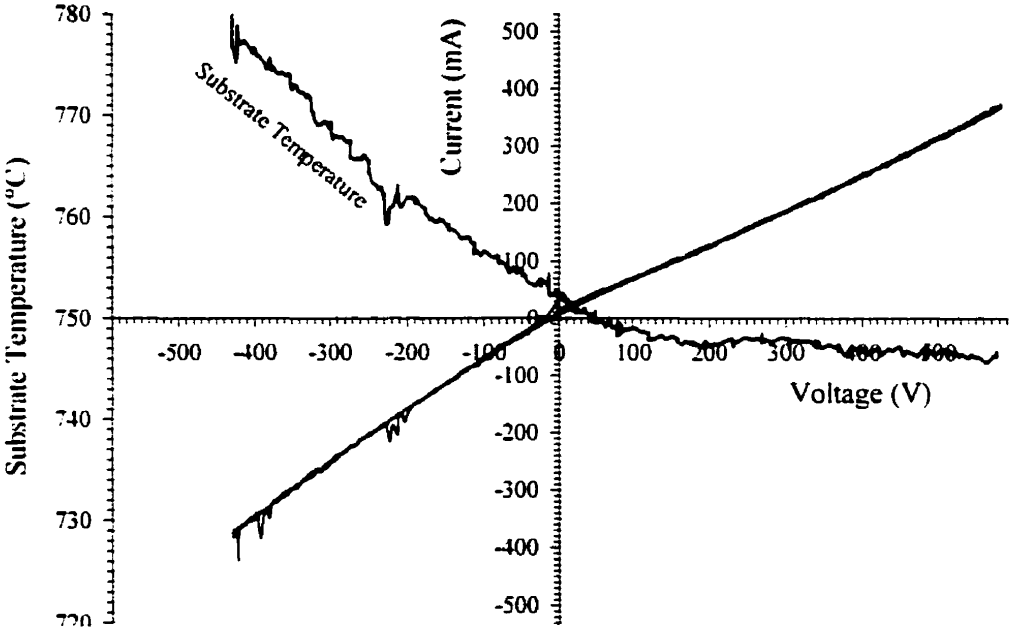

Figure 9.2.6 : Current-Voltage Temperature Characteristics at reduced effective plasma power.

9.3 Enhanced Nucleation at Negative Bias Voltage

A high initial nucleation density is generally desired to improve film adhesion, and can lead to an early coalescence of the diamond particles to produce a continuous and smooth coating in the early stages of the deposition (Yarbrough 1992, Chao et al. 1994). An increase in initial nucleation density is brought about by the application of a negative substrate bias in our thermal plasma system. This enhancement comes at the expense of a reduced diamond quality.

Yugo et al. (1991) were the first to show that diamond nucleation density in low-pressure CVD systems is markedly increased by negatively biasing the substrate, so-called bias enhanced nucleation (BEN). A number of mechanisms have been envisaged but the processes leading to nucleation are still not well understood. Likely mechanisms include ion bombardment that either affects the gas phase chemistry (Yugo et al. 1991), or leads to the creation of nucleation sites (Gerber et al. 1996), or even increases adatom diffusion on the surface (Jiang et al. 1994). It is also suggested that BEN may be related to an increase in electron emission from the substrate into the plasma. Even though our induction plasma differs from the non-thermal conditions, the nucleation process may be clarified in light of the previous low-pressure work.

9.3.1 Ion bombardment

Several studies in microwave plasma chemical vapor deposition (MPECVD) systems report the formation of an amorphous carbon intermediate layer on the surface into which the initial diamond nuclei are imbedded (Yugo et al. 1995/1996, Sattel et al. 1996, Reinke et al. 1995), inferring that ion bombardment leads to the formation of sp^3 bonded carbon clusters (so called subplantation) which serve as nuclei for subsequent diamond growth (Stöckel et al. 1996). Jiang et al. (1996) and Zhang et al. (1996) illustrate the role of ion bombardment by relating the diamond orientation of secondary nuclei to varying ion energy conditions, and McGinnis et al. (1995) show a direct correlation between ion bombardment energy and nucleation density. Consequently, the acceleration of ions from the plasma to the substrate surface at negative bias voltage is most often made

responsible for the increase in nucleation density in the BEN process in MPECVD (Yugo et al. 1995, Wolter et al. 1993). These nuclei possess low sp^3 content, which is understood in terms of ion impact, converting diamond to graphite or glassy carbon. Sattel et al. (1996) find optimal carbon ion energies of 70 to 90 eV for nucleation enhancement in a standard microwave CVD apparatus. McGinnis et al. (1995) and Kulish et al. (1996) report a threshold average ion energy in the order of ~ 15 eV and 15 to 20 eV, respectively, which has to be surpasses for a significant augmentation. Bárdos et al. (1994) quote a threshold energy of Ar^+ ions of about 50 eV, necessary to affect diamond crystals in a low pressure capacitive discharge.

Considering the magnitude of these threshold ion energies, it is unlikely that ion bombardment is the dominant cause for the nucleation enhancement observed in our study. At the near-atmospheric pressures in the rf thermal plasma, the ion energy is substantially reduced in the collisional sheath. The heat balance on our substrate clearly illustrates that the kinetic C^+ bombardment energy does not exceed ~ 4 eV. This value is notably smaller than any threshold reported in the literature.

9.3.2 Electron Emission

Stoner et al. (1993) observe a difference in diamond nucleation behaviour in a MPECVD system depending on the existence of a diamond coating on the surrounding substrate holder. The ion bombardment mechanism is thereby put in question. Electron emission from the diamond coating on the holder is made responsible for the diamond nucleation on the substrate, which begins on the edge and proceeds towards the centre. This evolution is accompanied by a local increase in dissociated hydrogen concentration in the gas phase near the surface. A similar phenomenon is reported by many authors, where a secondary plasma is initially localized on the diamond covered substrate holder but then advances radially towards the centre of the substrate, and diamond nucleation takes place at the front of the advancing glow (Kulish et al. 1996, Stöckel et al. 1998, Schreck et al. 1996 and Kim et al. 1996).

An increase in nucleation density with negative bias is also observed in hot filament CVD systems (HFCVD). Using such a system, Chen, Yang and Lin (1995) rule out the role of ions and conclude that enhanced nucleation results from an increased concentration of dissociated hydrogen and/or hydrocarbon radicals near the substrate surface, which is caused by electron emission from the diamond coating. Chen and Lin (1996) apply a negative bias while eliminating ion bombardment and show that negative bias alone cannot enhance nucleation without electron emission. The authors suggest an electron-emission–enhanced mechanism (EEE-method).

In our deposition system, the electron emission current from the diamond coating is substantial and may be as strong as to influence the growth behaviour. Similar to the MPECVD findings, a strong local interdependence of nucleation density with pre-existing diamond nuclei exists; i.e. diamond nuclei promote further nucleation in their neighbourhood, which often leads to anisotropy in the coverage. A typical example of such diamond nuclei coverage was shown in Figure 6.2.3 in section 6.2. Figure 9.3.1 shows two additional examples of non-uniform surface coverage where a number of those enhanced nucleation sites can be identified.

Figure 9.3.1: Top-view on samples of non-uniform substrate surface nuclei coverage.

Since the role of ion-bombardment can essentially be excluded in our system, we speculate that electron emission from the diamond is the predominant mechanism that leads to the observed nucleation enhancement at negative substrate bias. The associated degradation in the nuclei quality may be explained by the suppression of growth of emitting crystals as well as by the promotion of secondary nucleation.

Lee, Liu and Lin (1995) show that the growth of the diamond grains that emit electrons is suppressed and may even be converted in amorphous carbon and etched away by the plasma in extreme situations. Feng, Komvopolous and Brown (1995) produce amorphous carbon films at various bias voltages in a MPECVD system and study their resistance to etching in hydrogen plasma. They find that the etch resistance drastically decreases for an increase in sp^2 and decrease in sp^3 bonding present in the films.

In the MPECVD systems, an increase of atomic hydrogen concentration above the diamond-covered substrate at negative bias is often observed by optical emission spectroscopy (Schreck et al. 1996, Kulish et al. 1996, Cui et al. 1996). In the thermal plasma, the spatial extent of increased gas dissociation by electron emission is expected to be in the order of the electrical sheath. Such intensity variations above the substrate could not be identified in our study, possibly because our sheath dimensions are far smaller than the resolution of our spectroscopic (OES) detection capabilities.

9.4 Diamond Quality and Growth Rate at Positive Bias

An improvement both in diamond quality and in film growth rate at increasing positive substrate bias is experienced. This result is in agreement with findings in dc arc thermal plasma jet CVD, reported in the literature. In particular, we quote the earlier works by Matsumoto et al. (1990 and 1992), Baldwin et al. (1995) and Kruger et al. (1997), as well as Ito et al. (1995), which in part motivated the present study. Kruger reports an astonishing seven-fold increase in diamond growth rate at +170 V, as compared to the unbiased case. Ito observes a notable increase in the diamond purity at +70 V. Since OES measurements reveal that the positive voltage is coupled with a substantial increase in excited atomic hydrogen concentration (3.4 times) and electron temperature in the thermal boundary layer, the authors conclude that accelerated plasma electrons drive the boundary layer chemistry to a higher degree of non-equilibrium. The induced super-saturation raises the active radical flux to the growing surface, thereby favouring diamond formation.

A remarkable difference of the dc arc systems to our work is the high current density to the substrate. For example, Baldwin measures 3.5 A/cm^2 at +115 V, while we draw 0.4 A/cm^2 at that voltage and do not exceed 1.9 A/cm^2 at +600 V. Accordingly, dc arcjet biasing is referred to as the current flowing (Ito et al. 1995) or secondary discharge induced method (Baldwin et al. 1995). Furthermore, Matsumoto's photographs of the plasma with and without bias (1990) clearly suggest the creation of a transferred arc, whereby the diffuse arc attachment on the substrate anode can be identified. Since our electrode-less induction torch cannot serve as a cathode, the creation of a secondary discharge at positive bias in the above sense is not a possible explanation for the improved diamond growth. Plasma emission intensities above the substrate, within the dimensions of the thermal boundary layer, do strictly not show an increase in electron density or in atomic hydrogen concentration at positive bias in the case of H_β measurements, and only a slight increase in the case of H_γ. The predominant process in bias assisted diamond growth in rf induction plasma CVD is consequently not the secondary discharged induced mechanism found in dc arc-jet reactors. However, a slight

increase in electron temperature in the thermal boundary layer at positive bias is also observed in our case. Some plasma electron acceleration and consequent excitation of active species in the boundary layer cannot be excluded and is likely to play some role.

We speculate, however, that electron emission from the diamond surface, as a function of bias voltage, is the predominant factor in our case. At positive bias a suppressed electron emission from the crystals reduces secondary nucleation and allows these crystal faces to grow in an sp^3 configuration, which is less subject to etching than amorphous carbon structures. The lower etch rate of the diamond features promotes the higher net film growth rates at positive substrate bias voltage.

9.5 Deposition Stages

The diamond nucleation enhancement at negative bias voltage, as applied in the low-pressure CVD as well as in our study, is customarily considered a pretreatment step to improve the subsequent film growth (Kulish et al. 1996, Jiang et al. 1994). It is often used in conjunction with elevated methane concentration to further enhance the effect (Sattel et al. 1996). As opposed to conventional pretreatment methods such as scratching or seeding the substrate with diamond powder or damaging the surface to create high energy sites, bias enhanced nucleation is an *in-situ* technique that acknowledges the inherent difference in optimal conditions for diamond nucleation and diamond film growth. In the rf thermal plasma CVD process, operating parameters are generally highly coupled, making it difficult to change one process parameter without affecting all the others. Bias enhanced nucleation carries here particular importance because the bias voltage is an independent parameter, which can be adjusted during deposition at established plasma operating conditions.

Kulish et al. (1996) and Lee et al. (1995) observed an evolution in emission currents during diamond formation in MPECVD and interpret these changes in terms of a nucleation and growth sequence. In this work, the changing electron emission currents identify the duration of the nucleation stage and the onset of the growth stage. In particular, the evolution of the floating potential designates various phases. Figure 9.5.1 again illustrates the initial diamond nucleation, diamond growth and ionization stages.

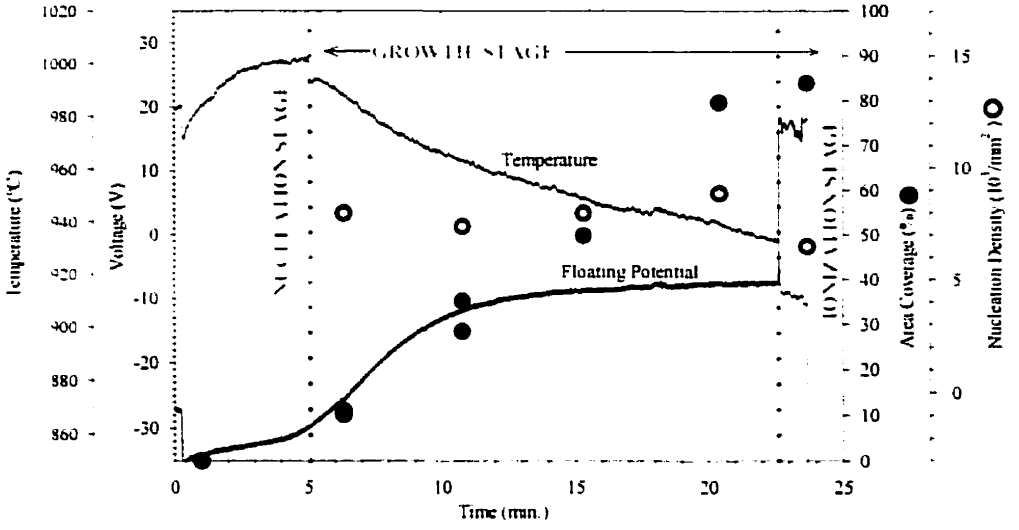

Figure 9.5.1 : Diamond Deposition Stages.

In order to grow continuous films, the substrate is covered with a high number of nuclei at a negative bias during the nucleation stage, and the nuclei are then allowed to grow and coalesce into a high quality film at a positive bias during the growth stage. The point of transition is determined by monitoring the evolution of the current or voltage characteristics during deposition. Applying such a two-step process yields homogeneous, continuous, and highly crystalline diamond film deposits on our substrate. Such deposits are then used in the assessment of diamond film quality and film growth rate as a function of bias voltage in section 6.4 and section 6.5. Representative examples are reproduced here in Figure 9.5.2.

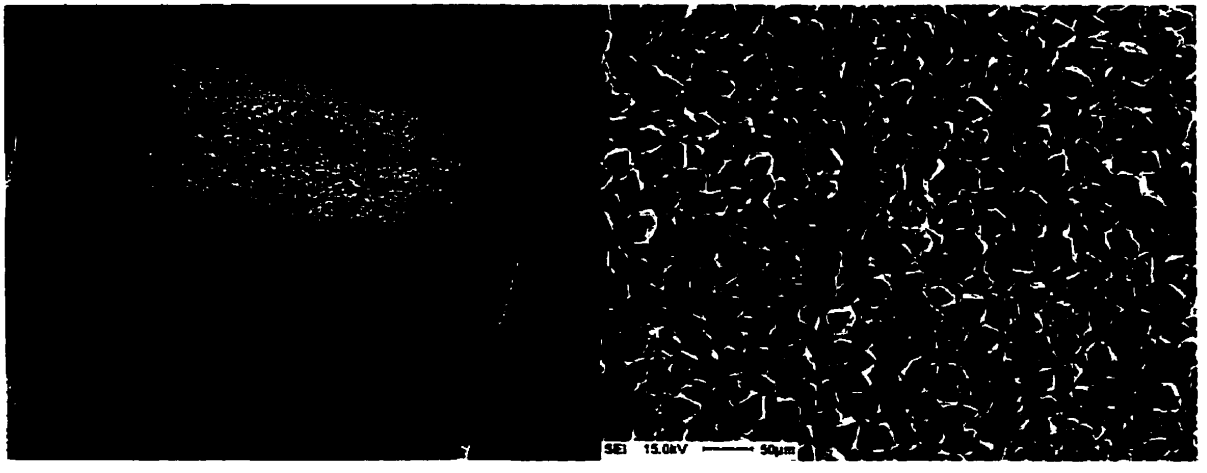

Figure 9.5.2: Representative Diamond Films produced in Two-Step CVD Process.

CONCLUSION

10. Conclusion

The implementation of d.c. substrate biasing in an r.f. induction thermal plasma diamond CVD system is demonstrated. The reactor environment is maintained at ground potential, and a high-impedance, high-power passive filter network, resonance tuned to the r.f. driving frequency, attenuates the r.f. voltage across the plasma-probe junction by –60 dB. Radio frequency interference (RFI) is alleviated to such a degree that the d.c. currents and voltages on the substrate probe can be accurately measured and electronically recorded during plasma operation. A traditional limitation of the induction thermal plasma CVD technology is thereby overcome.

The application of a bias voltage during deposition has a major effect on the nature of the resulting diamond deposit. Negative bias at and beyond –100 V enhances the initial diamond nucleation density. A three-fold increase is observed at –300 V over the non-biased case. However, the increased nucleation comes at the expense of a decline in diamond quality. Secondary nucleations leading to small crystal faces and amorphous carbon formation are promoted. Furthermore, non-uniform surface coverage is frequent.

On the other hand, positive bias substantially improves the diamond quality, and well-defined diamond morphologies are produced. In addition, positive voltages above +200V greatly increase the diamond growth rate. Linear film growth rates of up to 70 μm/hr are obtained at +500 V, as compared to ~20 μm/hr without bias.

At invariant plasma and bias operating conditions, neither the surface temperature nor the current to the substrate remain constant during deposition but change considerably as the diamond film evolves. The surface temperature varies due to a combined effect of radiation cooling and thermal insulation build up. The electrical variations reflect increasing electron emission from the developing diamond structures. Taking advantage of the changing emission current by using the growing film as an electrical probe, the diamond evolution is monitored *in-situ* from the initial nucleation to the final film growth. Typically, the nucleation stage terminates within the first five minutes of

deposition, and maximum surface coverage is attained after 20 to 25 minutes. Co-deposition of graphite particles, causing local discharges in the vicinity of the substrate, constitutes the main impediment to the measurement.

Acknowledging the inherent difference in diamond nucleation and film growth, the bias voltage is used as an additional and independent operating parameter and easily adjusted *in-situ* to the changing growth requirements at constant plasma operation. The substrate is covered with a high number of nuclei at a negative bias in the nucleation stage, and the nuclei are then allowed to grow and coalesce into a high quality film at a positive bias. The point of transition is determined from the changing probe characteristics. Applying such a two-step process yields homogeneous, continuous, and crystalline diamond films.

In contrast to previous research in dc arcjet diamond CVD, a positive substrate voltage in our r.f. system does not create a secondary discharge or transferred arc. In d.c thermal plasma systems such discharge is believed to promote the diamond growth by driving the boundary layer chemistry to a higher degree of non-equilibrium. Although the boundary layer chemistry plays also here an essential role in the diamond formation, evidence is presented that there are no substantial changes in the degree of dissociation or supersaturation in such dimension, even under strong bias conditions. The mechanism of bias assisted diamond deposition in r.f. thermal plasmas is therefore intrinsically different from the dc thermal plasma technology.

Although bias enhanced nucleation (BEN) in low-pressure diamond CVD systems is most often rationalized in terms of energetic ion bombardment of the substrate surface, the ion energy in our thermal plasma is substantially reduced to less than ~ 4 eV in the collisional sheath, and cannot be made responsible for the observed increase in nucleation density at negative bias. Appropriate theory applied to the electrical and thermal measurements shows that the interface between the plasma and the substrate at negative bias is described by an expanding collision-dominated sheath imbedded inside the ~1.5 mm thin chemically reacting thermal boundary layer.

It is suggested here that the predominant mechanism in bias assisted diamond CVD in the rf-induction thermal plasma system is the promotion and suppression of electron emission from the growing film. Enhanced electron emission at negative bias possibly causes local gas phase dissociation in the vicinity of the emission source, leading to increased nucleation and secondary nucleation, which prevent the formation of large crystal faces. The emitting site will eventually be etched away by the plasma. Electron emission is suppressed at positive bias, allowing the formation of larger and higher quality diamond crystals. These structures are less likely etched and an increase in net film growth rate results.

The present study demonstrates the use of substrate biasing as a unique tool to manipulate the diamond formation during deposition. Combining the benefits of substrate biasing with the high growth rates and film uniformity attainable in r.f. thermal plasma systems overcomes some of the traditional limitations in thermal plasma diamond CVD and likely augments its technological significance.

10.1 Contributions to Knowledge

The following original contributions to knowledge arise out of this work:

1. Implementation of d.c. substrate biasing in a r.f.-induction thermal plasma chemical vapor deposition (CVD) system is demonstrated for the first time.

2. The effect of bias voltage on diamond nucleation and diamond film growth is investigated: results show nucleation density enhancement with negative bias and growth rate and diamond quality increase at positive bias.

3. The growing diamond film is used as an electrical probe by which the film evolution is monitored during deposition; bias conditions are adjusted in-situ, providing a new control parameter that is independent of the plasma source.

4. Similarly, the substrate surface serves also as a thermal probe for monitoring the film growth. Both electrical and thermal probe aspects provide real time diagnostics of the deposition process that were not available in the past.

5. Mechanisms leading to bias assisted diamond CVD in r.f. thermal plasmas are investigated. Variation in electron emission from the diamond surface is identified as the main cause for the change in diamond growth at varying bias conditions.

Alder J.F., J.M. Mermet, "A spectroscopic study of some radio frequency mixed gas plasmas", *Spectrochimica Acta*, vol. 28B, pp. 421, 1973.

Anthony T.R., "Synthesis of Metastable Diamond", *Mat. Res. Soc. Symp. Proc.*; Diamond, Silicon Carbide and Related Wide Bandgap Semiconductors: vol.162, Pittsburgh, PA, pp. 61-74, 1990.

Bahr D.F., D.V. Bucci, L.S. Schadler, J.A. Last, J. Heberlein, E. Pfender, W. W. Gerberich, "Characterization of d.c. jet CVD diamond films on molybdenum", *Diamond and Related Materials*, vol. 5, pp. 1462-1472, 1996.

Baldwin S.K., T.G. Owano, C.H. Kruger, "Secondary discharge induced nonequilibrium chemistry in a CVD diamond dc arcjet reactor," *Proc. of the 12th Int. Symp. on Plasma Chem.*, Minneapolis, USA, vol. 3, pp. 2011-2016, Aug. 1995.

Baldwin S.K., T.G. Owano and C.H. Kruger, "Growth rate studies of CVD diamond in an rf plasma torch." *Plasma Chemistry and Plasma Processing*, vol. 14, no. 4, pp. 383-406, March 1994.

Baldwin S.K., T.G. Owano, C.H. Kruger," Increased deposition rate of chemically vapor deposited diamond in a direct-current arcjet with a secondary discharge," *Appl. Phys. Lett.*, vol. 67, no. 2, pp. 194-196, July 1995.

Bárdos L., T. Nyberg, H. Baránková, S. Berg, "Effect of the space charge sheath on properties of carbon and diamond films in the r.f. plasma jet", *Diamond and Related Materials*, vol. 3, pp. 528-530, 1994.

Beckmann R., B. Sobisch, W. Kulisch, C. Rau, "Investigation of the bias nucleation process in microwave plasma-enhanced chemical vapour deposition of diamond", *Diamond and Related Materials*, vol. 3, pp. 555-559, 1994.

Bieberich M.T., S.L. Girshick, "Control of substrate temperature during diamond deposition", *Plasma Chemistry and Plasma Processing*, vol. 16, no. 1(Supplement), pp. 157S-168S, 1996.

Blades M.W., "Excitation mechanisms and discharge characteristics – recent developments", Chapter 11 in *Inductively Coupled Plasma Emission Spectroscopy: Applications and Fundamentals*, by J. M. Boumans, Part 2. John Wiley & Sons, New York, 1978.

Bleekrode R.; W.C. Nieuwpoort, "Absorption and emission of C_2 and CH", *The Journal of Chemical Physics*, vol. 43, no. 10, pp. 3680, Nov. 1965.

Bonnot A.M., "Raman microspectroscopy of diamond crystals and thin films prepared by hot-filament-assisted chemical vapor deposition", *Physical Review B*, vol. 41, no. 9, pp. 6040-6049, March 1990.

Boulos M.I., P. Fauchais, E. Pfender, : *Thermal Plasmas: Fundamentals and Applications*, Volume 1, Plenum Press, New York, 1994.

Bousrih S., E. Ershov-Pavlov, S. Megy, J.-M. Baronnet, " Hydrogen/argon plasma jet with methane addition", *Plasma Chemistry and Plasma Processing*, vol. 15, no. 2, pp. 333-351, 1995.

Bradley D., S.M.A. Ibrahim, "Determination of positive-ion mobilities and collision cross sections in flame gases using electrostatic probes", *J. Phys. D: Appl. Phys.*, vol.7, pp. 1377-1390, 1974.

Bradley D., S.M.A. Ibrahim, "The effects of electrical fields upon electron energy exchanges in flame gases", *Combustion and Flame*, vol. 22, pp. 43-52, 1974.

Braithwaite N.S.J., N.M.P. Benjamin, J.E. Allen, "An electrostatic probe technique for rf plasma", *J. Phys. E: Sci. Instrum.*, vol. 20, pp. 1046-1049, 1987.

Cappelli M.A., "The nonequilibrium region of an electrode in contact with a flowing thermal plasma", *IEEE Transactions on Plasma Science*, vol. 21, no.1, pp. 194-201, Feb. 1993.

Cappelli M.A., T.G. Owano and C.H. Kruger, "High growth rate diamond synthesis in a large area atmospheric pressure inductively coupled plasma," *Journal of Material Research*, vol. 5, no. 11, pp. 2326-2333, Nov. 1990.

Chang K.W., G.K. Bienkowski, "Effects of electron emission on electrostatic probes at arbitrary pressure", *The Physics of Fluids*, vol. 13, no. 4, pp. 902-920, April 1976.

Chao, C.H., G. Popovici, E. H. Charlson, E. M. Charlson, J. M. Meese, M. A. Prelas, " Smooth diamond films grown by hot filament chemical vapor deposition on positively biased silicon substrates," *Journal of Crystal Growth*, vol. 140, pp. 454-458, 1994.

Chen F.F., "Electric probes", Chapter 4 in *Plasma Diagnostic Techniques*, Huddlestone R. H., ed.: New York, Academic Press, 1965.

Chen Q., J. Yang, Z. Lin, "Synthesis of oriented textured diamond films on silicon via hot filament chemical vapor deposition", *Appl. Phys. Lett.*, vol. 67, no. 13, pp. 1853-1855, September 1995.

Chen Q., Z. Lin, "Electron-emission-enhanced diamond nucleation on Si by hot filament chemical vapor deposition," *Appl. Phys. Lett.*, vol. 68, no. 17, pp. 2450-2452, April 1996.

Chung P.M., "Electrical characteristics of Couette and stagnation boundary-layer flows of weakly ionized gases", *The Physics of Fluids*, vol. 7, no. 1, pp. 110-120, Jan. 1964.

Clements M.R., C.S MacLatchy, P.R. Smy, "Verification of static spherical probe theory in a moving high-pressure plasma", *J. Appl. Phys.*, vol. 43, no. 1, pp. 31-36, Jan. 1972.

Clements M.R., P.R. Smy, "Electrostatic-probe studies in a flame plasma", *Journal of Applied Physics*, vol. 40, no. 11, pp. 4552-4559, Oct. 1969.

Clements M.R., P.R. Smy, "Ion current from a collision-dominated flowing plasma to a cylindrical electrode surrounded by a thin sheath", *Journal of Applied Physics*, vol. 41, no. 9, pp. 3745-3750, Aug. 1970.

Clements M.R., P.R. Smy, "Stagnation probe measurements in flowing plasmas", *J. Phys. D: Appl. Phys.*, vol. 4, pp. 1687-1694, 1971.

Clements M.R., P.R. Smy, "Langmuir probe measurements of electron temperature in high-pressure plasmas", *Journal of Applied Physics*, vol. 44, no. 8, pp. 3550-3556, Aug. 1973.

Coulombe S., J.-L. Meunier, "Importance of high local cathode spot pressure on the attachment of thermal arcs on cold cathodes", *IEEE Transactions on Plasma Science*, vol. 25, no. 5, pp. 913-918 , Oct. 1997.

Coulombe S., J.-L. Meunier, "Thermo-field emission : a comparative study ", *J. Phys. D: Appl. Phys.*, vol. 30, pp. 776-780, 1997.

CRC Handbook of Chemistry and Physics. Cleveland, Ohio : CRC Press, 70th Ed., 1989-1990.

Cui J.B., R.C. Fang, "The influence of bias on gaseous composition and diamond growth in a hot-filament chemical vapour deposition process", *J. Phys. D: Appl. Phys.*, vol. 29, pp. 2759-2762, 1996.

Davies P.B., P.M. Martineau, "Diagnostics and modeling of silane and methane plasma CVD processes", *Advanced Materials*, vol. 4, no. 11, pp. 729, 1992.

Deueler F., M. Pies, H. van den Berg, R. Tabersky, V. Buck, "Production, characterisation, and wear behaviour of plasma jet CVD diamond films on hard metal cutting tools," *Phys. Stat. Sol. A*, vol. 154, pp. 403-422, 1996.

Dilecce G., M. Capitelli, S. De Benedictis, "Electron energy distribution function measurements in capacitive coupled rf discharges", *J. Appl. Phys.*, vol. 69, no. 1, pp. 121-128, Jan. 1991.

Feng Z., K. Komvopoulos, I.G. Brown, "Effect of amorphous carbon film structure on diamond nucleation", *J. Appl. Phys.*, vol. 78, no. 4, pp. 2720-2724, Aug. 1995.

Fish P. J., *Electronic noise and low noise design*: New York : McGraw Hill, 1994.

Fomenco V.S., *Handbook of Thermionic Properties*, Plenum Press, New York, 1966.

Gagné R.R.J., A. Cantin, "Investigation of an rf plasma with symmetrical and asymmetrical electrostatic probes", *J. Appl. Phys.*, vol. 43, no. 6, pp. 2639-2647, 1972.

Gaydon A.G., M.G. Wolfhard, "Spectroscopic studies of low pressure flames", *Proc. Roy. Soc. (London)*, vol. A201, pp. 561, 1950.

Gerber J., S. Sattel, H. Ehrhardt, J. Robertson, P. Wurzinger, P. Pongratz, " Investigation of bias enhanced nucleation of diamond on silicon," *J. Appl. Phys.*, vol. 79, no. 8, pp. 4388-4396, Apr. 1996.

Girshick S.L., C. Li, B.W. Yu and H. Han. "Fluid boundary layer effects in atmospheric-pressure plasma diamond film deposition", *Plasma Chemistry and Plasma Processing*, vol. 13, no. 2, pp. 169-87, 1993.

Godbole V.P., K. Jagannadham, J. Narayan, " Nucleation and growth of diamond films on aluminium nitride coated nickel," *Appl. Phys. Lett.*, vol. 67, no. 9, pp. 1322-1324, Aug. 1995.

Goodwin D.G., "A model for diamond film deposition in a thermal plasma", *Materials Research Society*, Extended Abstract (EA-19), pp. 153, 1989

Goodwin D.G., G.G. Gavillet, "Numerical modeling of the filament-assisted diamond growth environment", *J. Appl. Phys.*, vol. 68, no. 12, pp. 6393, Dec. 1990.

Goodwin D.J., "Simulation of high-rate diamond synthesis: Methyl as growth species", *Appl. Phys. Lett.*, vol. 59, no. 3, pp. 277, July 1991.

Harris S.J., "Gas-phase kinetics during diamond growth: CH_4 as growth species.", *J. Appl. Phys.*, vol. 65, no.8, pp. 3044, April 1989.

Hernberg R., T. Mäntylä, T. Sternberg, J. Vattulainen, "Diamond synthesis on molybdenum in rf induction plasma," *Proc. of the 10th Int. Symp. on Plasma Chem.*, vol. 3.1-1, pp. 1-6 , 1991.

Hong D., M. Aslam, "Field emission form p-type polycrystalline diamond films", *J. Vac. Sci. Technol. B*, vol. 13, no. 2, pp. 427-430, 1995.

Huang, Z.-H., P.H. Cutler, N. M. Miskovsky, T.E. Sullivan, "Theoretical study of field emission from diamond", *Appl. Phys. Lett.*, vol. 65, no. 20, pp. 2562-2564, Nov. 1994.

Huong, P.V., "Structural studies of diamond films and ultrahard materials by Raman and micro-Raman spectroscopies", *Diamond and Related Materials*, vol. 1, pp. 33-41, 1991.

Ito N., M. Yamamoto, S. Nakamura, T. Hattori," Purification of diamond films by applying current into the plasma stream in the arc discharge plasma jet chemical vapor deposition technique," *J. Appl. Phys.*, vol. 77, no. 12, pp. 6636-6640, June 1995.

Jian, X., L. Quingyuan, L. Wenchong, Q. Haowen, T. Jingyuan, Z. Zhangxia , "Matrix effects of easily ionized elements on the spatial distribution of electron number densities in an inductively coupled plasma using an optical fiber probe and a photodiode array spectrometer", *Journal of Analytical Atomic Spectrometry*, vol. 7, pp. 131, March 1992.

Jiang X., K. Schiffmann, C.-P. Klages, "Nucleation and initial growth phase of diamond thin films on (100) silicon", *Physical Review B*, vol. 50, no. 12, pp. 8402-8410, Sep. 1994.

Jiang X., W.H. Zhang, M. Paul, C.-P. Klages, " Diamond film orientation by ion bombardment during deposition," *Appl. Phys. Lett.*, vol. 68, no. 14, pp. 1927-1929, April 1996.

Kalnicky D.J., V.A. Fassel, R.M. Kniseley, "Excitation temperatures and electron number densities experienced by analyte species in inductively coupled plasmas with and without the presence of an easily ionised element", *Applied Spectroscopy*, vol. 31, no. 2, pp. 137, 1977.

Karner J., M. Perazzini, I. Reineck, M.E. Sjöstrand, E. Bergmann, "CVD diamond coated cemented carbide cutting tools," *Material Science and Engineering*, vol. A209, pp. 405-413, 1996.

Kemp R.F., J.M. Sellen, "Plasma potential measurements by electron emissive probes", *Rev. Sci. Instrum.*, vol. 37, no. 4, pp. 455-461, April 1966.

Kersten H., E. Stoffels, W.W. Stoffels, M. Otte, C. Csambal, H. Deutsch, R. Hippler, "Energy influx from an rf plasma to a substrate during plasma processing", *Journal of Applied Physics*, vol. 87, no. 8, pp. 3637-3645, April 2000.

Kim S.H., Y.S. Park, I.T. Han, J.-W. Lee, W.S. Yun, "Effect of cyclic process on the {100}-oriented texture growth of diamond film", *Appl. Phys. Lett.*, vol. 69, no. 15, pp. 2184-2186, October 1996.

Kodali V. P.: *Engineering Electromagnetic Compatibility* :New York : IEEE Press, 1996.

Kohzaki M., K. Uchida, K. Higuchi, S. Noda," Large-area high-speed diamond deposition by rf induction thermal plasma chemical vapor deposition method", *Jpn. J. Appl. Phy.*, vol. 32 part 2, no. 3B, pp. L438-L440, 1993.

Kolman D., J. Heberlein, E. Pfender, R. Young, "Two-dimensional model for thermal plasma chemical vapor deposition", *Plasma Chemistry and Plasma Processing*, vol. 16, no. 1 (Supplement), pp. 57S-68S, 1996.

Kruger C.H., T.G. Owano, C.O. Laux, "Experimental investigation of atmospheric pressure nonequilibrium plasma chemistry", *IEEE Transactions on Plasma Science*, vol. 25, no. 5, pp. 1042-1051, Oct. 1997.

Kulish W., L. Ackermann, B. Sobisch, "On the mechanisms of bias enhanced nucleation of diamond," *Physic Status Solidi A*, vol. 154, no. 155, pp. 155-174, 1996.

Lam S.H., "A general theory for the flow of weakly ionised gases", *AIAA Journal*, vol. 2, no. 2, pp. 256-262, 1964.

Lee J.S., K.S. Liu, I-Nan Lin, "Direct-current bias effect on the synthesis of (001) textured diamond films on silicon," *Appl. Phys. Lett.*, vol. 67, no. 11, pp. 1555-1557, Sept. 1995.

Lee Y.H., G. H. Ma, K.J. Bachmann, J.T. Glass, "Bias controlled hot filament chemical vapor deposition of diamond thin film on various substrates," *Mat. Res. Soc. Symp.*, vol. 162, pp. 119-125, 1990.

Liu J., V.V. Zhirmov, A.F. Myers, G.J. Wojak, W.B. Choi, J. J. Hren, S. D. Wolter, M.T. McClure, B.R. Stoner, J.T. Glass, "Field emission characteristics of diamond coated silicon field emitters", *J. Vac. Sci. Technol. B*, vol. 13, no. 2, pp. 422-426, Mar./Apr. 1995.

Lu Z.P., J. Heberlein, E. Pfender, "Process study of thermal plasma chemical vapour deposition of diamond Part I: substrate material, temperature, and methane concentration," *Plasma Chemistry and Plasma Processing*, vol. 12, no. 1, pp.35-53, 1992.

Lu Z.P., L. Stachowicz, P. Kong , J. Heberlein , E. Pfender , "Diamond synthesis by dc thermal plasma CVD at 1 atm," *Plasma Chemistry and Plasma Processing*, vol. 11, no. 3, pp 387-394. 1991.

Ma Y., T. Tsurumi, N. Shinoda, O. Fukunaga, "Effect of bias enhanced nucleation on the nucleation density of diamond in microwave plasma CVD", *Diamond and Related Materials*, vol. 4, pp. 1325-1330, 1995.

MacLatchy C.S., "Langmuir probe measurements of ion density in an atmospheric-pressure air-propane flame", *Combustion and Flame*, vol. 36, pp. 171-178, 1979.

MacLatchy C.S., C.L. Smith, "The electron current to a Langmuir probe in a flowing high-pressure plasma", *IEEE Transactions on Plasma Science*, vol. 19, no. 6, pp.1254-1258, Dec. 1991.

Matsui Y., H. Yave, Y. Hirose, "The growth mechanism of diamond crystals in acetylene flames", *Japanese Journal of Applied Physics*, vol. 29, no.8, pp. 1552-1560, Aug. 1990.

Matsumoto S., I. Hosoya, T. Chuonan, "Substrate bias effect in diamond deposition by dc plasma jet," *Japanese Journal of Appl. Phys.*, vol. 29, no. 10, pp. 2082-2086, Oct. 1990.

Matsumoto S., I. Iosoyp, Y. Manabe, Y. Ilibino, " Diamond synthesis in thermal plasma CVD," *Pure and Appl. Chem.*, vol. 64, no. 5, pp. 751-758, 1992.

Matsumoto S., M. Hino, T. Kobayashi, "Synthesis of diamond film in a rf induction thermal plasma, " *Appl. Phys. Lett.*, vol. 51, no. 10, pp.737-739, Sept. 1987.

McGinnis S.P., M.A. Kelly, S.B. Hagström, "Evidence of an energetic ion bombardment mechanism from bias-enhanced nucleation of diamond", *Appl. Phys. Lett.*, vol. 66, no. 23, pp. 3117-3119, March 1995.

Meeks E., M.A. Cappelli, "A multi-fluid stagnation-flow plasma model with self-consistent treatment of the collisional sheath", *IEEE Transactions on Plasma Science*, vol. 21, no. 6, pp. 768-777, Dec. 1993.

Meeks E., M.A. Cappelli, "Two-temperature fluid model for high-pressure plasma in contact with cooled electrodes", *J. Appl. Phys.*, vol. 73, no. 7, pp. 3172-3182, April 1993.

Mermet J.M., "Spectroscopic diagnostics: Basic concepts", Chapter 10 in *Inductively Coupled Plasma Emission Spectroscopy: Applications and Fundamentals*, by J. M. Boumans, Part 2. John Wiley & Sons, New York, 1978.

Metals Handbook: Metallography, Structures and Phase Diagrams,8th Ed., Volume 8, Materials Park, Oh.: ASM International, 1998.

Milne D.K., P.G. Roberts, P. John, M.G. Jubber, M. Liehr, J.I.B. Wilson, " Epitaxy of diamond on silicon", *Diamond and Related Materials*, vol. 4, pp. 394-400, 1995.

Mizumura M., S. Uotsu, S. Matsumura, S. Teii, "Probe system with bias compensation using a laser heated emissive probe for rf discharge plasma diagnostics," *J. Appl. Phys.*, vol. 25, pp. 1744-1748, 1992.

Monteiro O.R., Z. Wang, I.G. Brown, "Novel technique to produce strongly adherent diamond films on Fe- and Ni-base alloys," *Mat. Res. Soc. Symp. Proc.*, vol. 416, pp. 139-144, 1996.

NRC Report: *Status and Application of Diamond-Like Materials - An Emerging Technology*: National Academy Press, Washington D.C., 1990

Oberste Berghaus J.,"Induction Plasma Deposition of Diamond Thin Films," M.Eng. Thesis, McGill Univ., Montreal, Quebec, Canada, July 1996.

Oberste Berghaus J., J.-L. Meunier, F. Gitzhofer,"Local growth studies of CVD diamond using a probe-like substrate", *IEEE Transactions on Plasma Science*, vol. 25, no. 5, pp. 1058-1065, Oct. 1997.

Oberste Berghaus J., J.-L. Meunier, F. Gitzhofer,"Diamond coatings for tool shafts by induction plasma deposition", *Int. Journal of Refractory Metals and Hard Materials*, vol. 16, no. 3, pp. 201-205, 1998.

Ott H.W., *Noise Reduction Techniques in Electronic Systems*, 2nd Ed.,New York : John Wiley & Sons, 1988.

Owano T.G., D.G. Goodwin, C.H. Kruger, M.A.Cappelli, "Diamond Synthesis in a 50 kW inductively coupled atmospheric pressure plasma torch", *Proc. of the 10th Int. Symp. on Plasma Chem.*, Bochum, Germany, vol. 3, no. 1, pp. 1-8, Aug. 1991.

Owano T.G., E.H. Wahl, C.H. Kruger,"Diagnostics of boundary layer chemistry in thermal plasma CVD", *Proc. of the 12th Int. Symp. on Plasma Chem.*, Minneapolis, USA, vol. 3, pp. 2017-2022, Aug. 1995.

Paranjpe A.P., J.P. McVittie, S.A. Self, "A tuned Langmuir probe for measurements in rf glow discharges", *J. Appl. Phys.*, vol. 67, no. 11, pp. 6718-6727, June 1990.

Park D.W., H. Park, "Diamond synthesis by rf thermal plasma CVD," *Proc. of the 12th Int. Symp. on Plasma Chem.*, p. 2267, Aug. 1995.

Perry R.H., Green, D., *Perry's Chemical Engineers' Handbook, 6th ed.*, McGraw-Hill, 1984.

Ravi K.V., Chapter 14 in *Synthetic Diamond: Emerging CVD Science and Technology* by Karl E. Spear and John P. Dismukes, John Wiley & Sons, Inc. 1994.

Reinke P., P. Kania, P. Oelhafen, "Investigation of the nucleation mechanism in bias-enhanced diamond deposition on silicon and molybdenum," *Thin Solid Films*, vol. 270, pp 124-129, 1995.

Reinke P., P. Kania, P. Oelhafen, "Investigation of the nucleation mechanism in bias-enhanced diamond deposition", *Appl. Phys. Lett.*, vol. 68, no. 1, pp. 22-24, January 1996.

Sattel S., J. Gerber, H. Ehrhard, "Ion induced nucleation of diamond," *Physica Status Solidi A*, vol. 154, no. 141, pp. 141-153, 1996.

Sattel S., J. Robertson, M. Scheib, H. Ehrhardt, "Ion assisted growth of diamond," *Appl. Phys. Lett.*, vol. 69, no. 4, pp. 497-499, July 1996.

Schlesser R., M.T. McClure, W.B. Choi, J.J. Hren, Z. Sitar, "Energy distribution of field emitted electrons from diamond coated molybdenum tips", *Appl. Phys. Lett.*, vol. 70, no. 12, pp.1596-1598, March 1997.

Schott L., "Electrical Probes", Chapter 11: *Plasma Diagnostics* by Lochte-Holtgreven, W., Amsterdam: North-Holland Pub. Co., 1968.

Schreck M., B. Stritzker, "Nucleation and growth of heteroepitaxial diamond films on silicon", *Physical Status Solidi A*, vol. 154, pp. 197-217, 1996.

Self S.A., L.D. Eskin, "The boundary layer between electrodes and a thermal plasma", *IEEE Transactions on Plasma Science*, Vol. PS-11, No.4, pp. 279-285, Dec. 1983.

Smith, J. T., N. Hershkowitz, P. Coakley, "Inflection-point method of interpreting emissive probe characteristics", *Rev. Sci. Instrum.*, vol. 50, no. 2, pp. 210-218, Feb. 1997.

Smy P.R., "The use of Langmuir probes in the study of high pressure plasmas", *Advances in Physics*, vol. 25, No. 5, pp. 517-553, 1976.

Špatenka P., H. Suhr, "Langmuir probe measurements during plasma-activated chemical vapor deposition in the system argon/oxygen/aluminium isopropoxide", *Plasma Chemistry and Plasma Processing*, vol. 13, no. 3, pp. 555-566, 1993.

Špatenka P., R. Studený, H. Suhr, "Apparatus for Langmuir probe monitoring of plasma during deposition processes", *Meas. Sci. Technol.*, vol. 3, pp. 704-708, 1992.

Spear D.E., "Diamond - Ceramic Coating of the Future"; *Journal of the American Ceramic Society*; vol. 72, no. 2, pp.171-191, 1989.

Stöckel R., K. Janischowsky, S. Rohmfeld, J. Ristein, M. Hundhausen, L. Ley, "Diamond growth during bias pre-treatment in the microwave CVD of diamond," *Diamond and Related Materials*, vol. 5, pp. 321-325, 1996.

Stöckel R., K. Janischowsky, S. Rohmfeld, J. Ristein, M. Hundhausen, L. Ley, "Growth of diamond on silicon during the bias pretreatment in chemical vapor deposition of polycrystalline diamond films," *J. Appl. Phys.*, vol. 79, no. 2, pp. 768-775, Jan. 1996.

Stöckel R., M. Stammler, K. Janischowsky, L. Ley, M. Albrecht , H.P. Strunk, "Diamond nucleation under bias conditions," *J. Appl. Phys.*, vol. 83, no. 1, pp. 531-539, Jan. 1998.

Stoner, B.R., G.H. Ma, S.D. Wolter, W. Zhy, Y.-C. Wang, R.F. Davis, J.T. Glass, "Epitaxial nucleation of diamond on β-SiC via bias-enhanced microwave plasma chemical vapor deposition," *Diamond and Related Materials*, vol. 2, pp. 142-146, 1993.

Stoner B.R., G.H. Ma, S.D. Wolter, J.T. Glass, "Characterization of bias-enhanced nucleation of diamond on silicon by in vacuo surface analysis and transmission electron microscopy", *Physical Review B*, vol. 45, no. 19, pp. 11067-11084, May 1992-I.

Su C.H., "Compressible plasma flow over a biased body", *AIAA Journal*, vol. 3, no. 5, pp. 842-848, 1964.

Talbot L., "Theory of the stagnation-point Langmuir probe", *The Physics of Fluids*, vol. 3, no. 2, pp. 289-298, March 1960.

Taylor R.E., *Radio Frequency Interference Handbook*, National Aeronautics and Space Administration, Washington D.C. 1971.

Teii K., "Diagnostics of the diamond depositing inductively coupled plasma by electrostatic probes and optical emission spectroscopy", *J. Vac. Sci. Technol. A*, vol. 17, no. 1, pp. 138-143, Jan/Feb. 1999.

Thorpe M.L., L.W. Scammon, "Induction plasma heating: High power, low frequency operation and pure hydrogen heating", *NASA Contractor Report*, National Aeronautics and Space Administration, Washington, D.C., May 1969.

Touloukian Y. S., *Thermal Radiative Properties: Metallic Elements and Alloys*, New York, Plenum Press, 1970.

Visser K., F.M. Hamm, P.B. Zeeman, "Temperature determination in an inductively coupled rf plasma", *Applied Spectroscopy*, vol. 30, no. 1, pp. 34, 1976.

Weiser, P.S., S. Prawer, " Chemical vapour deposition of diamond onto iron based substrates - the use of barrier layers," *Diamond and Related Materials*, vol. 4, pp. 710-713, 1995.

Wiese W.L., "Line broadening", Chapter 6 in *Inductively Coupled Plasma Emission Spectroscopy: Applications and Fundamentals*, by J. M. Boumans, Part 2. John Wiley & Sons. New York. 1978.

Wolter S.D., B.R. Stoner, J.T. Glass, "Textured growth of diamond on silicon via in situ carburisation and bias-enhanced nucleation", *Appl. Phys. Lett.*, vol. 62, no. 11, pp. 1215-1217, March 1993.

Yan S, J. Kamal, J. Amundson, N. Hershkowitz, "Use of emissive probes in high pressure plasma", *Rev. Sci. Instrum.*, vol. 67, no. 12, pp. 4130-4137, Dec. 1996.

Yarborough W.A., "Vapour-phase deposited diamond - problems & potential," *Journal of the American Ceramic Society*, vol. 75, 1992.

Yu B.W., S.L. Girshick, "Atomic carbon vapor as a diamond growth precursor in thermal plasma", *J. Appl. Phys.*, vol. 75, no. 8, pp. 3914-3923, April 1994.

Yu W., S.L. Girshick, "Diamond film deposition in a thermal plasma - effect of substrate location," *Proc. of the 9th Int. Symp. on Plasma Chem.*, vol. 2, pp. 1439-1443, 1989.

Yugo S., K. Semoto, K. Hoshina, T. Kimura, H. Nakai, " A modelling of diamond nucleation," *Diamond and Related Materials*, vol. 4, pp. 903-907, 1995.

Yugo S., K. Semoto, T. Kimura, "The cause of suppression of the diamond nucleation density," *Diamond and Related Materials*, vol. 5, pp. 25-28, 1996.

Yugo S., T. Kanai, T. Kimura, T. Muto, "Generation of diamond nuclei by electric fields in plasma chemical vapor deposition," *Appl. Phys. Lett.*, vol. 58, no. 10, pp. 1036-1038, March 1991.

Zhang W.J., X. Jiang, " The growth characteristics of (001) oriented diamond layers on (111) diamond face via bias-assisted chemical vapor deposition", *Appl. Phys. Lett.*, vol. 68, no. 16, pp. 2195-2197, April 1996.

Zhang Y.F., D. Dunn-Rankin, P. Taborek, "Potential role of atomic carbon in diamond deposition", *J. Appl. Phys.*, vol. 74, no. 11, pp. 6941-6947, Dec. 1993.

Zhu W., R.C. McCune, J.E. deVries, M.A. Tamor, K.Y. Simon Ng, " Investigation of adhesion of diamond films on Mo, W and carburized W substrates," *Diamond and Related Materials*, vol. 4, pp. 220-233, 1995.

Zhuang O.D., H. Guo, J.V.R. Heberlein,"Control of Substrate Temperature and its Uniformity for Thermal Plasma CVD", *Proc. of the 11th Int. Symp. on Plasma Chem.*, Loughborough, England, vol.1, pp.1680-1685, Aug. 1992.